Title
Development of a strain rate sensitive ice material model for hail ice impact simulation

Permalink
https://escholarship.org/uc/item/294018cv

Author
Tippmann, Jeffery Dwayne

Publication Date
2011

Peer reviewed|Thesis/dissertation

UNIVERSITY OF CALIFORNIA, SAN DIEGO

Development of a Strain Rate Sensitive Ice Material Model for Hail Ice Impact Simulation

A Thesis submitted in partial satisfaction of the requirements
for the degree of Master of Science

in

Structural Engineering

by

Jeffery Dwayne Tippmann

Committee in Charge:

Professor Hyonny Kim, Chair
Professor David Benson
Professor Francesco Lanza di Scalea

2011

The Master's Thesis of Jeffery Dwayne Tippmann is approved, and is acceptable in quality and form for publication on microfilm and electronically:

Chair

University of California, San Diego

2011

TABLE OF CONTENTS

Page

LIST OF TABLES

Table Page

LIST OF FIGURES

Figure Page

ACKNOWLEDGEMENTS

The author is thankful for the tremendous amount of support provided by numerous mentors and friends. I first would like to thank Professor Hyonny Kim, who I have worked with and known for over six years since working with him as an undergraduate research assistant in the summer of 2004 at Purdue University, for the excellent guidance and support through my academic and professional career. This work would not have been possible without his support. I would also like to thank my friends at ATA Engineering, Inc., who also supported my pursuit of graduate education.

A special thanks and strong acknowledgement to the Federal Aviation Administration for partially sponsoring and allowing for this work to be possible and also to D. Larry Illcewicz for his feedback and recommendations. I would also like to specially thank Hwun Park and Jennifer Rhymer for their significant contributions to the data set of experimental measured force history results of SHI impact, and also for teaching me the lab equipment and procedures.

ABSTRACT OF THE THESIS

Development of a Strain Rate Sensitive Ice Material Model for Hail Ice Impact Simulation

by

Jeffery Dwayne Tippmann

Master of Science in Structural Engineering

University of California, San Diego, 2011

Professor Hyonny Kim, Chair

A strain rate sensitive ice material model for hail ice impact simulation has been developed using previously measured ice compressive strength at impact strain rates. Simulations were conducted in Abaqus/Explicit and were compared to experimental tests of simulated hail ice impacts on a force measurement bar apparatus. The force history during the ice impact event studied shows agreement between the simulation results and the experimental data. The overall trend of peak force versus kinetic energy was also compared, showing a strong correlation. The scatter in the measured ice compressive strength data was incorporated in the modeling approach and was found to represent the scatter in the sphere impact experimental test data. Observations of the failure progression of simulated hail impact were made using high speed video images during impact tests. The simulation-predicted failure progression was found to qualitatively match with the failure behavior exhibited by actual ice spheres, thereby indicating that the model represents some of the basic physics and phenomena that govern ice impacts.

CHAPTER 1. INTRODUCTION

1.1. Motivation

Ice impacts and the ensuing dynamic loading are significant issues in many fields, such as ship building, arctic researchers, aviation, and interplanetary space missions. The focus of the research effort described herein is concentrated on the commercial aviation industry, where the ice projectiles are hail stones from meteorological weather systems. Hail impacts have always been of interest to commercial aviation, but within the last decade has become of greater importance due to the significant use of composite materials such as carbon fiber reinforced plastics in exposed primary structural components. The impact of hail projectiles requires a minimum skin thickness across all sizes of aircraft, requiring significantly more weight for smaller jets [1], since the major design driver becomes hail impact resistance.

Numerical simulations are often used for the studying various phenomena in greater detail to understand more than what is available (i.e., what quantities can be measured) during a physical test. Accurate modeling of the hail projectile and its impact behavior is a difficult aspect of studying hail impacts because of the complexity of the ice material. Because new aircraft are using complex composite laminates, numerical simulations provide information about damage initiation thresholds, formation, and growth, which can be difficult to capture and study in detail outside of a computer simulation. In order to produce accurate results on the target side, the projectile properties must be accurately modeled. Development of a hail projectile simulation model started over ten years ago in DYNA3D [2], with a couple researchers adding improvements [3, 4]. The research reported here builds on the previous works by providing an Abaqus material model with strain rate dependent failure that uses published rate-sensitive ice strength data [5]. Previous simulated hail ice (SHI) models [2 - 4] have required parameters to be manually adjusted for each simulation to account for rate effects.

1.2. Objective

The objective of this research is to provide a strain rate dependent ice material model for use in the commercial Finite Element Analysis (FEA) software Abaqus for simulating hail impacts. By using strain rate dependent ice strength data, the new material model will require no velocity or size dependent parameters to be manually adjusted by the analyst. The material is compared to existing and new experimentally-measured force history data measured during ice impact.

1.3. Approach

Ice compressive strength was previously measured for impact strain rates (10^3 s^{-1}) by Kim and Kuene [3, 5]. The results provided strength data previously unavailable when SHI models were first developed in DYNA3D by Kim and Kedward [2] and Kuene [3]. An Abaqus model similar to the model Kuene provided was developed by Park [4]. These models were correlated to experimental tests by varying the model's material input parameters, specifically the yield strength and hydrostatic tensile failure pressure. The new work presented here uses the dynamic compressive strength data [5] to add a strain rate dependent yield strength in the

Abaqus material model. The final model contains a simple elastic material with a strain rate dependent yield stress and a non-rate dependent tensile pressure failure criterion. The key and distinguishing aspect of this new material model is that it will not require the analyst to do individual tuning for each test.

The simulation results are compared to experimental data from Kim et al. [6] and unpublished experimental measurements of SHI dynamic forces using a force measurement bar apparatus. The simulation-predicted and experimentally measured force histories and peak forces are compared to show that a good correlation has been established. High speed video images of SHI impact are used to make qualitative observations of the failure progression during the impact event.

CHAPTER 2. BACKGROUND

2.1. Ice Material Behavior

Ice is a complex polycrystalline structure with individual crystals that can be of various sizes and orientations [7]. Ice mechanical property data can vary based on the temperature, grain size, and grain direction, exhibiting the Hall-Petch effect of grain boundary strengthening [8]. However, the ice crystalline structure has been observed to be of a stronger influence more in low strain rate impacts and less in high speed impacts [9]. The type of ice which is typically fabricated for experimental use is referred to as Polycrystalline ice (Ih) [8]. Natural atmospheric forming ice, particularly hailstones, are too difficult to collect and also irregular in their size and shape,, thus a lab-manufactured substitute is used for testing in hail impact research and is distinguished from natural hail by the designation of SHI.

2.1.1. Compressive Strength

The two failure models, tensile and compressive, each have unique behaviors in the failure of ice. The tensile failure strength is greatly affected by the grain size and is not dependent on strain rates, whereas compressive failure does depend on temperature and strain rates [7]. Compressive failure, the mode which occurs when under confinement, is the dominant mode of failure in hail ice during impact because the Hertzian-like contact between the spherical projectile and flat target results in the maximum stress always being compressive [10].

The compressive strength of ice has been measured using a Split Hopkinson Pressure Bar (SHPB) apparatus [5]. Several sources report experimentally measured compressive strengths of ice at different strain rates, temperatures, and grain orientations [5, 11 - 16]. A summary of the effect of strain rate on the compressive strength of ice is shown in Figure 2.1.

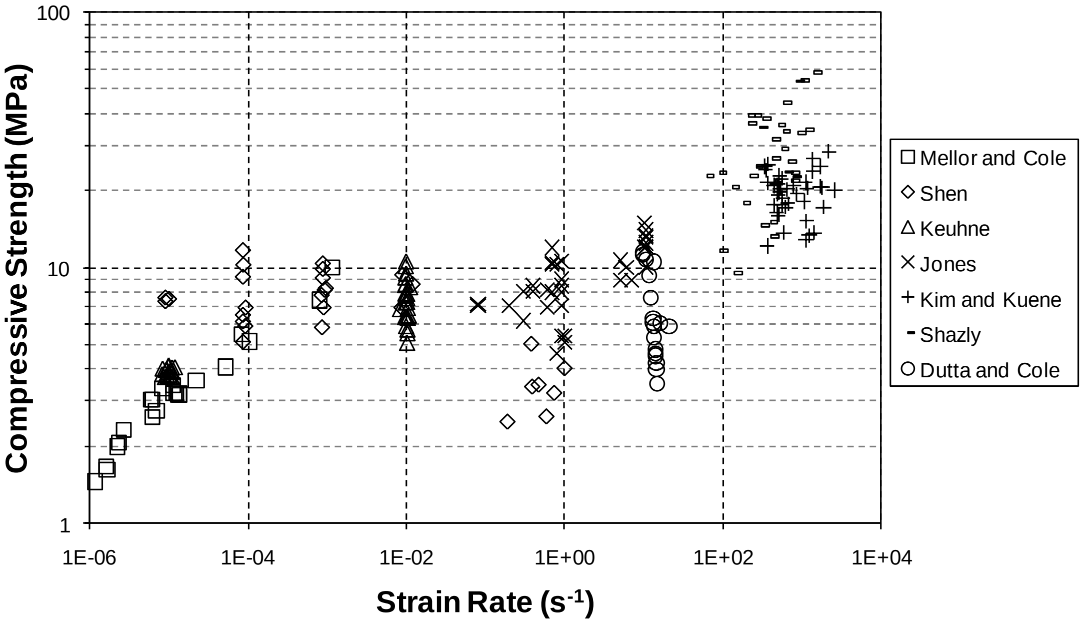

Figure 2.1: Collection of published ice compressive strength experimental data results

Low strain rates between 10^{-6} to 10^{-1} s^{-1} have been used to characterize the crack nucleation and propagation in ice, where at some point in this range the ice transitions from ductile to brittle behavior [7]. However, hail ice impacts are all high speed events occurring at velocities greater than 30 m/s with strain rates above 10 s^{-1} [5]. Kim and Kuene focused on measuring compressive strength data at impact strain rates, 10^3 s^{-1}, where data did not exist at the time [3, 5]. There were conflicting theories of what happened to the compressive strength of ice as strain rates increased above 10^1 s^{-1} [3]. The results in Figure 2.2 from Kim and Kuene [5] show a nearly constant value across the strain rates tested (10^2 to 10^3 s^{-1}) with a slight rising trend. However the wider survey summarized in Figure 2.1 shows an increase in compressive strength as the strain rate increases from above 10^{-2} to 10^3 s^{-1}.

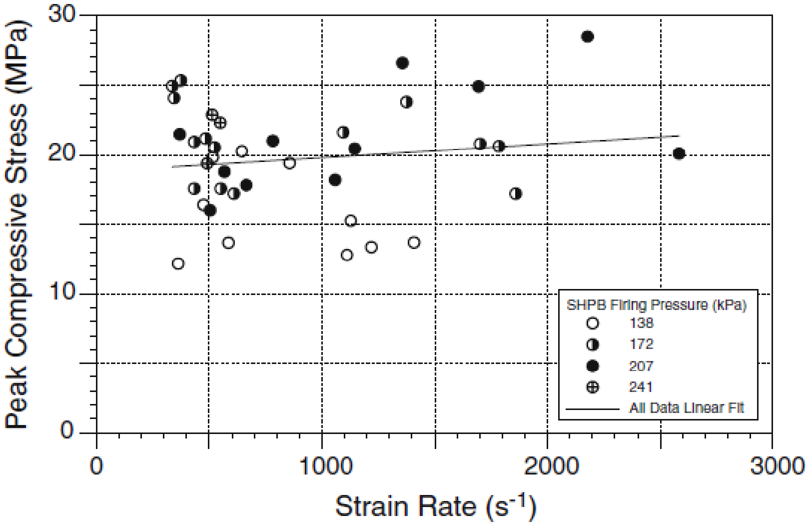

Figure 2.2: Kim and Kuene [5] high strain rate compressive strength data

In a response to ice impacts during Space Shuttle launches, Shazly et al. [15] more recently studied the compressive strength of ice at high strain rates. The testing included different types of ice: single crystal (“perfect”) ice with a singular granular direction strictly controlled during fabrication at Ice Culture, Inc. and multi-grain ice samples grown in lab from de-ionized water. The single crystal specimens showed a higher compressive strength than the multi-grain specimens. Photomicrographs of the single crystal and multi-grain structures are shown in Figures 2.3 and 2.4, respectively.

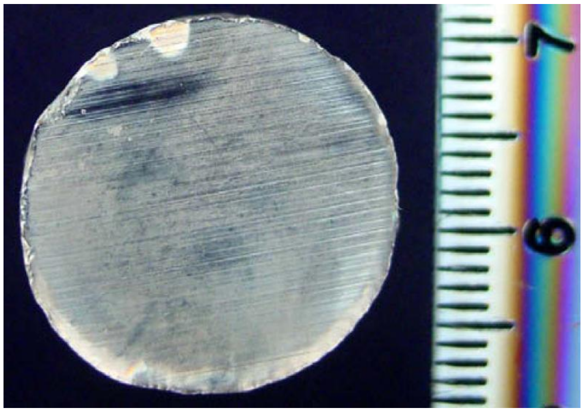

Figure 2.3: Single grain ice structure; 1mm between scale lines [15]

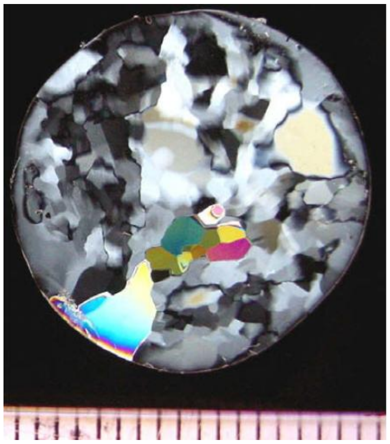

Figure 2.4: Multi-grain ice structure; 1mm line between scale lines [15]

2.1.2. Simulated Hail Ice

Hail ice naturally forms in layers, but this natural formation is very difficult to reproduce in a controlled laboratory environment. A monolithic form, which is a sphere cast from a mold during a single -filling/freezing session using de-ionized water, is a form that is easily and repeatedly produced. Layered ice is also used in experimental tests [6], but takes several casting sessions to form the ice in layers. Both forms constitute a multi-grain ice structure that is present in the SHI used in the experiments discussed in this research. Density for SHI can range from 880 to 930 kg/m^3, but generally has a density of 920 kg/m^3 [4], while natural hail ice has been measured to have densities of 870 to 920 kg/m^3. Halpin and Kim [17] reported the distributions of naturally-occurring hail sizes, as shown in Figure 2.5. The 90th, 95th, and 99th percentile hail sizes are 44.7, 51.8, and 66.8 mm, respectively. SHI diameters of 38.1, 50.8, and 61.0 mm were used in the impact experiments of this research.

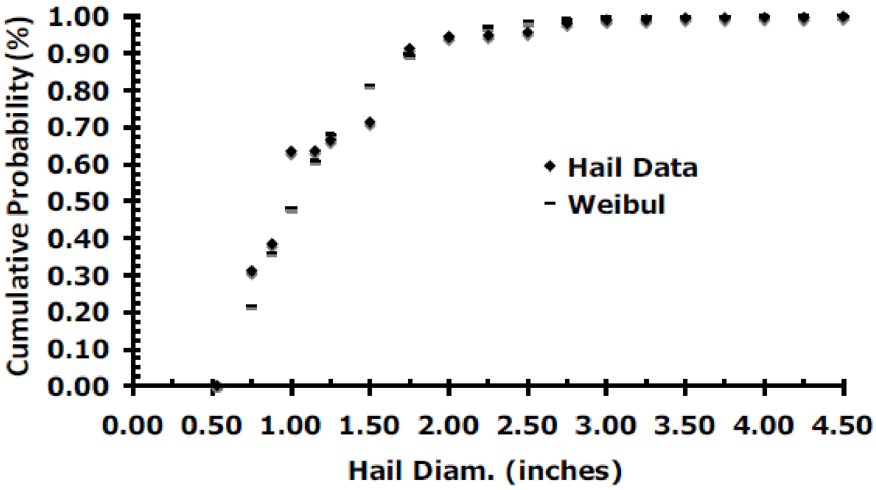

Figure 2.5: Hail ice size distribution data [17]

2.2. Kim et al. Experiments

Experimental SHI tests were conducted by Kim et al. [6]. The tests included a velocity range of 30 to 200 m/s, layered and monolithic ice, and three different SHI diameters: 25.4, 42.7, and 50.8 mm. The force history data were recorded using a dynamic force transducer system [2, 6] which is a nearly rigid target composed of a piezoelectric force cell mounted between a titanium front striking plate and heavy steel block. Figure 2.6 shows a representative example of the force history data and visual observations obtained by these experiments. A list of the tests used from this previous body of work [2, 6] for comparison of the simulation results in this current research is presented in Table 2.1. The peak force and impulse data are extracted from the force history data for each test.

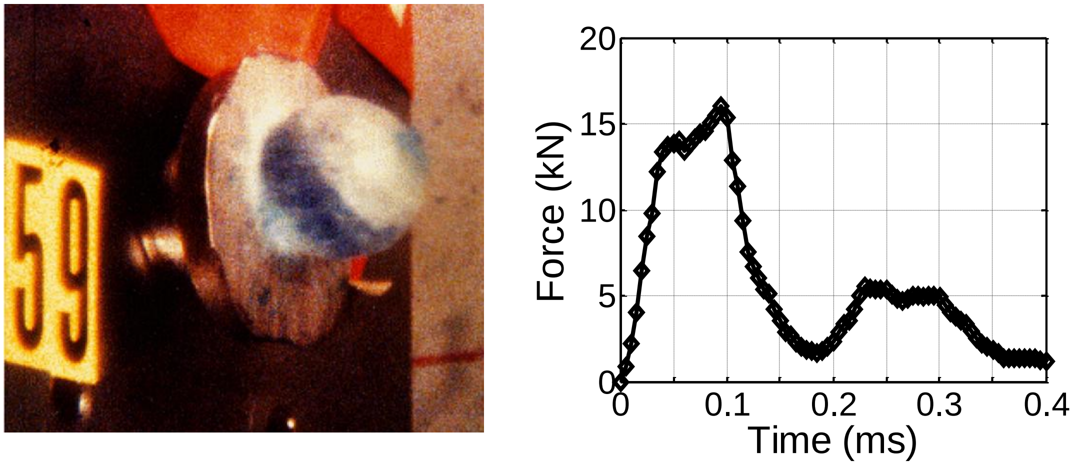

Figure 2.6: Visual observation and force history data of ice impact of SHI on force measurement apparatus; Test 59: 42.7 mm diameter SHI at 73.5 m/s

Table 2.1: Previous Experiments [2, 6] Test Summary

Test ID	Diameter (mm)	Velocity (m/s)	Kinetic Energy (J)	Peak Force (kN)	Impulse (N-s)
47	50.8	136.6	529	88.4	10.20
48	50.8	104.6	309	45.4	6.38
49	50.8	61.9	108	19.6	3.12
50	42.7	149.4	380	57.0	5.46
54	42.7	126.2	271	44.9	4.92
59	42.7	73.5	92	16.0	2.45
60	42.7	81.7	114	19.2	2.88
61	42.7	95.4	155	26.2	3.52
63	42.7	96.0	163	32.3	3.92

2.3. Numerical Models

Material models for SHI impact numerical simulations have been previously developed by Kim [2, 18], Kuene [4], and Park [5]. Carney et al. [10] developed an ice model by comparing results to impact experiments of ice cylinders.

2.3.1. Kim and Kedward DYNA3D Model

Kim and Kedward [2] developed a material model in the explicit FEA software DYNA3D (Lawrence Livermore National Laboratory version) and compared the results to experimental tests of both monolithic and flat-wise layered ice, as shown in Figure 2.7. The material model used DYNA3D Material “Type 13 Elastic-Plastic with failure”. The models uses failure strain and tensile failure pressure criteria to set shear stress components in failed elements to zero and thereby limiting the element behavior such that it carries only hydrostatic compression stresses (i.e., fluid-like). However, the same material model parameter values were used for all cases of SHI diameter and velocity, and did not include any dependencies on strain rate. The material parameter values were determined by comparing the simulation results with experimental data. An example comparison of Test 59 is shown in Figure 2.8. Note that while the overall shape of the force time history was generally well-matched, the peak force value was significantly off.

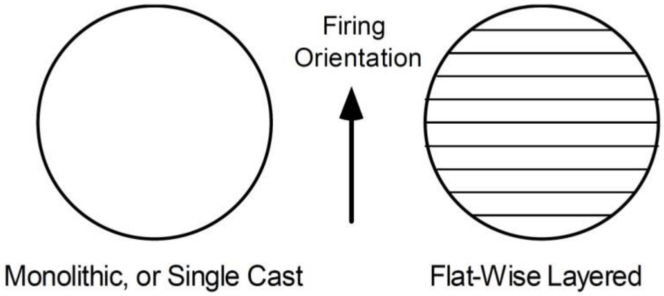

Figure 2.7: Two types of ice tested by Kim et al. [2, 6]

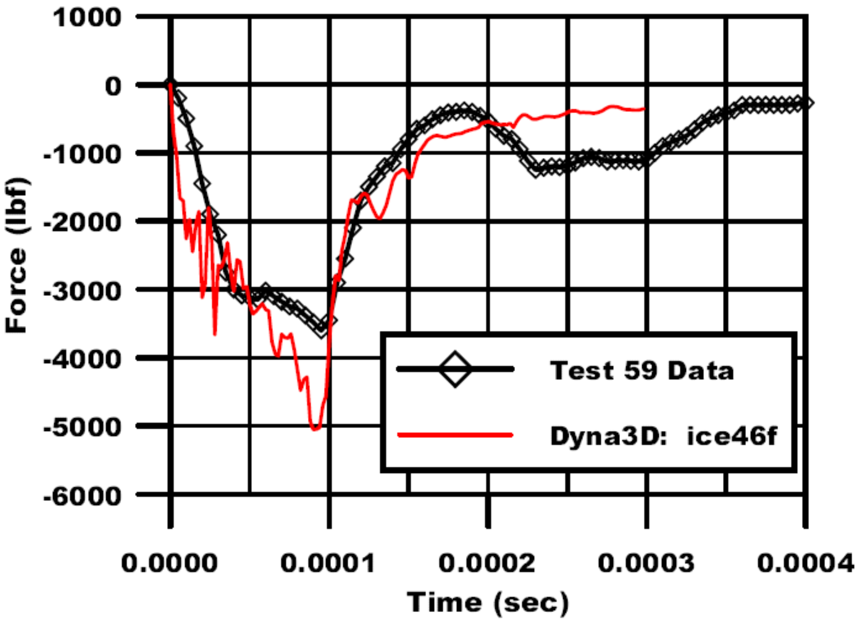

Figure 2.8: Test 59 comparison; 42.7 mm layered SHI at 73.5 m/s

2.3.2. Kuene LS-DYNA Model

Kuene extended the model developed by Kim and Kedward [2], using the same elastic-plastic with failure type material in the software LS-DYNA (commercialized version of DYNA3D). The material inputs, particularly yield strength and failure pressure, were varied for each test condition. A relationship was developed that allowed the analyst to select the appropriate values depending on the projectile size and velocity. The simulation results compared well with the previous model [2] and demonstrated much closer match to all the experimental data, as shown by example in Figure 2.9.

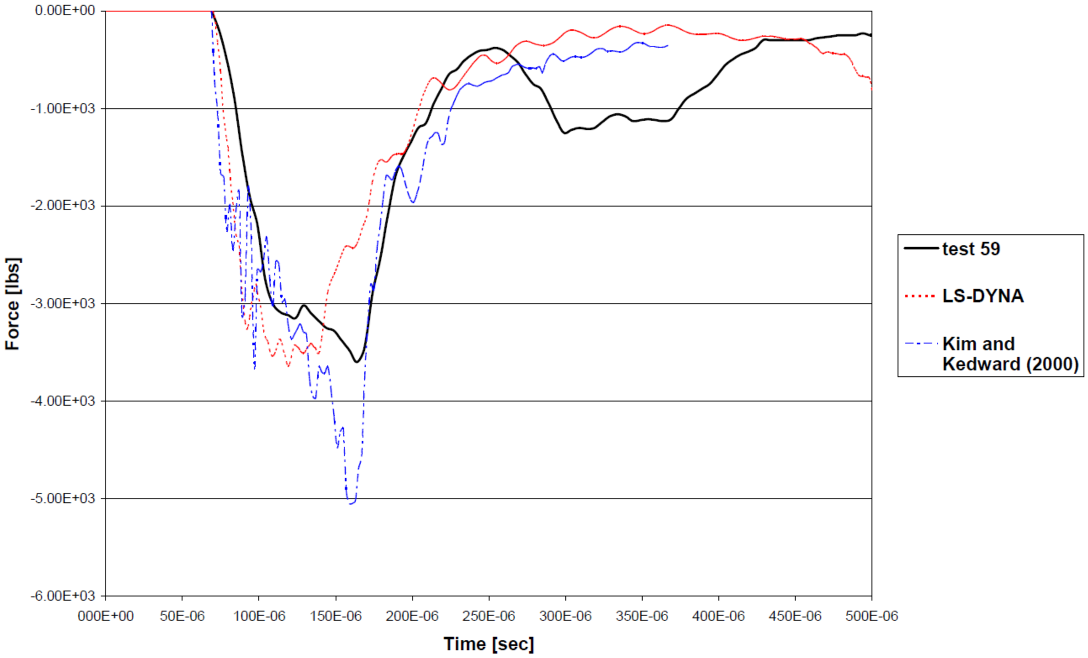

Figure 2.9: LS-DYNA simulation comparison to Kim et al.
Test 59 experimental results [3]

2.3.3 Park ABAQUS Model

An ABAQUS model similar to the model presented by Kuene [3] was developed by Park [4]. A 1:1 translation from LS-DYNA was not possible because the material model available in ABAQUS did not exactly match with the elastic-plastic with failure model in LS-DYNA. However, the modifiable parameters, yield strength and tensile failure, remained the same. Other effects such as element deletion and bulk viscosity were studied and recommended by Park [4]. The force histories compared well with the previous model results, as shown in Figure 2.10. Like Kuene's model [3], manual selection of material parameters was needed to achieve good correlation, such as that shown in Figure 2.10 for a wide range of ice diameter and velocity.

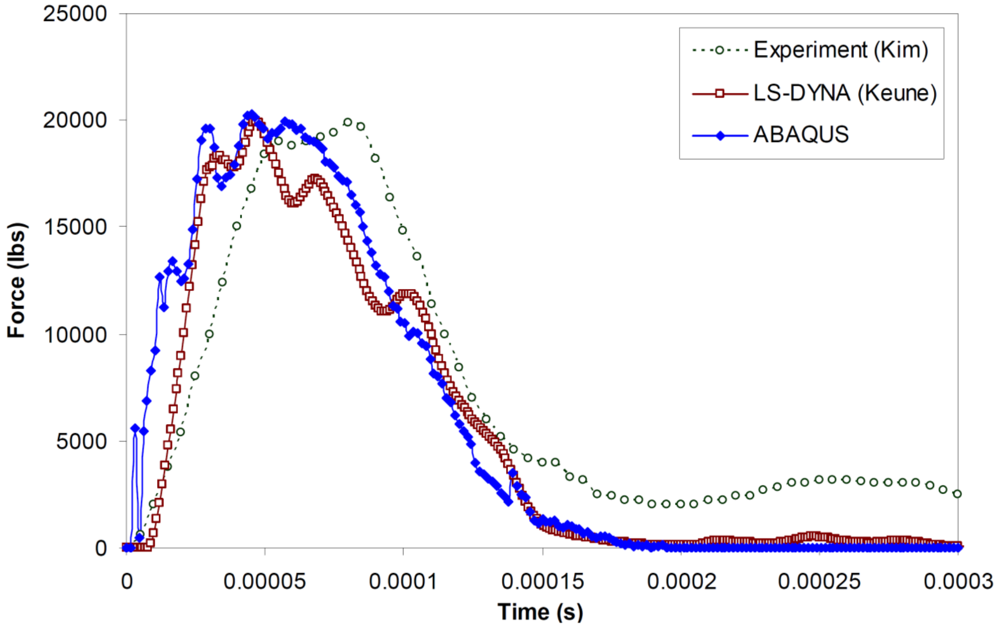

Figure 2.10: Comparison of Abaqus and LS-DYNA simulation results with Kim et al. Test 47 experimental force history results; 50.8 mm Layered SHI 136.5 m/s [4]

2.3.4. Carney et al. Strain Rate Dependent LS-DYNA Ice Material Model

A study by Carney et al. [10] was completed on the impact of ice cylinders, with efforts focused on understanding the threshold for critical damage to the Space Shuttle orbiter's leading edge due to ice impacts. Carney et al. [10] developed a phenomenological high strain rate ice material model with failure in LS-DYNA. The material model contained independent compression and tension failure levels and strain rate dependent failure parameters. A significant difference between previous models [2-4] was the use of LS-DYNA's multi-material Eulerian capability where the projectile was represented as an Eulerian mesh domain and the target as Lagrangian elements. The material model compared well to cylinder experimental impact force history measurements. A single comparison shown in Figure 2.11 to a Kim et al. [2] experiment showed good agreement of the initial force pulse, with large oscillations after 1.5 ms.

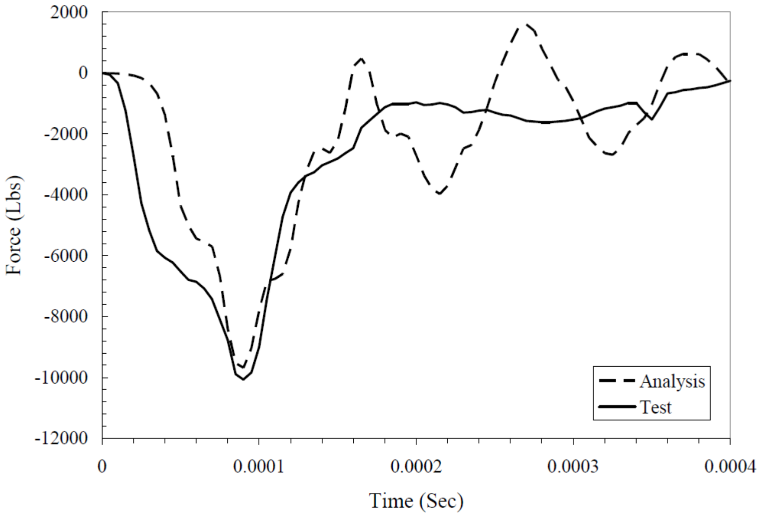

Figure 2.11: Comparison of LS-DYNA strain rate dependent simulation results [10] to Kim et al. Test 54 [2] experimental force history results; 42.7 mm diameter layered SHI at 126.2 m/s

CHAPTER 3. SIMULATED HAIL ICE IMPACT EXPERIMENTS

3.1. Test Setup

A gas gun shown in Figure 3.1 was used to project the SHI onto the force measurement bar apparatus shown in Figure 3.2 that recorded the force history of the impact. The gas gun uses compressed nitrogen held in a reservoir, together with a solenoid-actuated pneumatic ball valve, to quickly release the stored gas, which then propels a foam sabot carrying the SHI down the smooth-bore stainless steel tube barrel. As the sabot exits the barrel of the gun, it splits into two parts and is stopped by a 12.7 mm thick steel plate (see inset in Figure 3.1). The SHI continues through a hole in the sabot stop plate and passes through a velocity measurement system. The velocity measurement apparatus uses two lasers and photodiode sensors set at a known distance to determine speed of the projectile, with timing of the laser breaks measured by an oscilloscope. After leaving the velocity measurement system, the projectile continues on to impact the target.

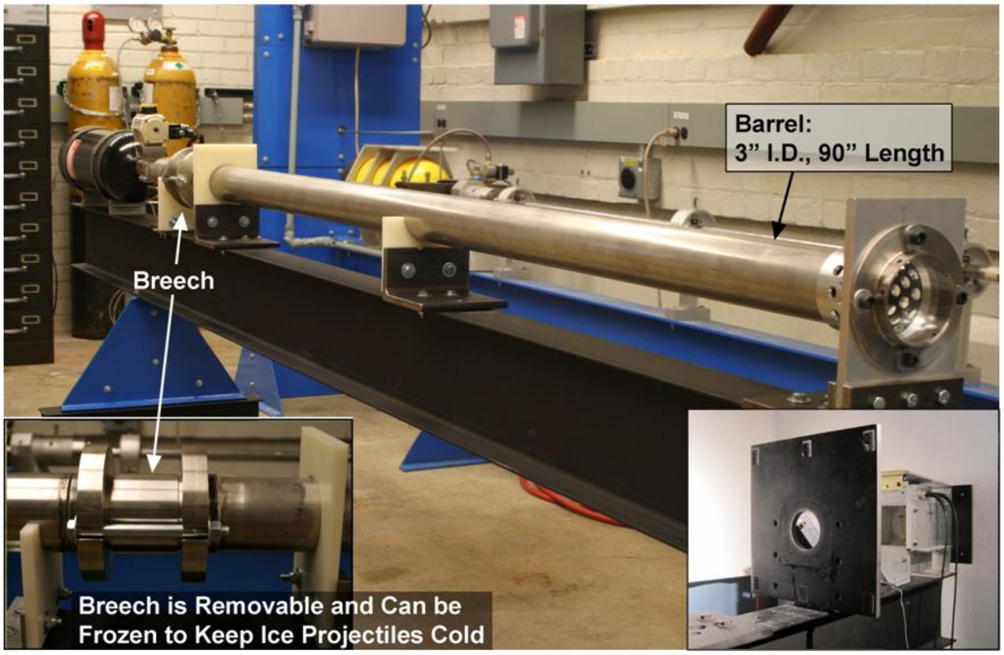

Figure 3.1: Gas gun apparatus used to project SHI

The target in this research is a force measurement bar constructed of a 3.05 meter aluminum tube, an impact end cap of 25.4 mm thick Aluminum,, and two strain gages placed at the same 45.7 cm distance from the impact cap but on opposite sides of the tube. When the SHI hits the impact end cap, it transfers a stress wave through the tube. Using a Wheatstone Bridge, the two strain gages can measure the average axial stress (assuming linear Hooke's Law) with all bending contributions eliminated by the half-bridge configuration. The voltage output is recorded with a bridge excitation and amplification system (Vishay 2310B) and then recorded by an oscilloscope at sample rate at 5 MHz. The final voltage time history is then converted to a force using a conversion factor of 901.8 N/mV based on measurements of the cross-sectional area of 13.86 cm^2 and aluminum bar Young's Modulus of 68.9 GPa, and strain gage excitation of 10V with 10X amplification factor.

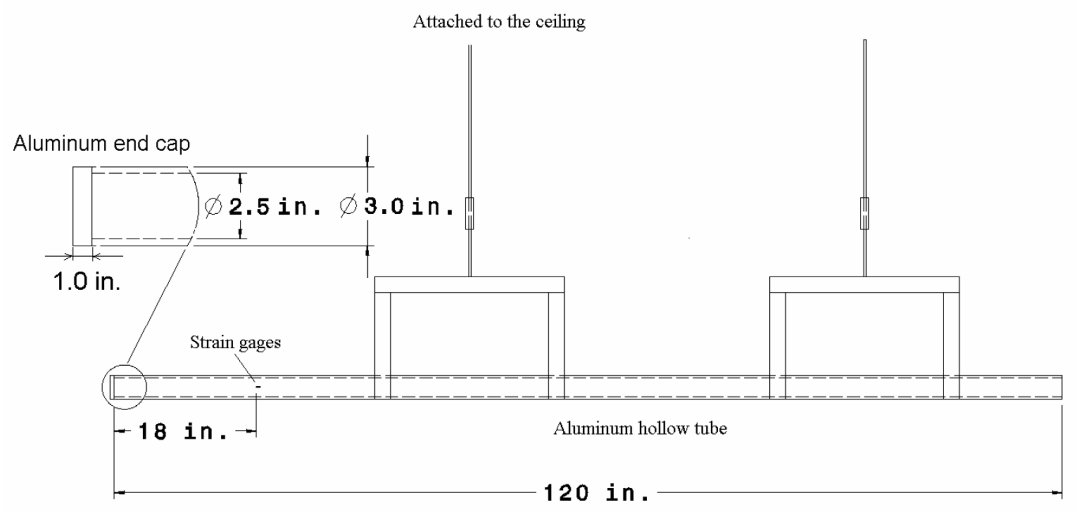

Figure 3.2: Schematic of force measurement bar apparatus

High speed observations were recorded during each experiment using up to two Phantom V. 7.3 high speed video cameras. The videos served two purposes: (i) to observe the integrity of SHI projectile just before impact and (ii) to observe the process of failure propagation. The images in Figure 3.3 (a-c) show an angled view of the impact progression of a SHI projectile impacting onto the FMB. By the last frame, the SHI has broken down into small fragments and powder spray.

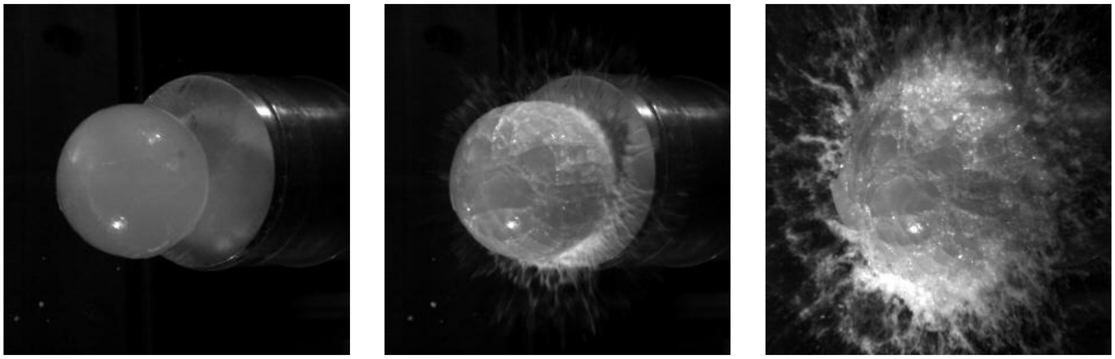

(a) t = 0 µs (b) t = 160 µs (c) t = 540 µs

Figure 3.3: High speed video of ice impact on FMB; UCSD Test 191: 61.0 mm diameter SHI at 61.8 m/s at 201 (J)

3.2. Experimentally-Measured Force Time History

Several new experiments had been conducted using the force measurement bar apparatus, adding to the previously discussed tests by Kim et al. [6], referred to as Data Set #1 (DS1). All remaining unpublished experiments using the force measurement bar apparatus are referred to as Data Set #2 (DS2). It is important to note that two other researchers (Hwun Park at Purdue and University in 2006 and Jennifer Rhymer at UCSD from 2007 to 2010) contributed heavily to the population of DS2 in addition to the experiments performed by this thesis' author.

The experiments in DS2 consist of 38.1, 50.8, and 61.0 mm SHI sizes and velocities from 19.3 to 193.7 m/s. In total, 56 experiments of monolithic SHI were performed (layered ice data has been excluded from DS2). An example measured force history, plotted in Figure 3.4, shows the two phases of the force history: a nearly linear force increase and then a sharp directional change with a decreasing force trend. All the measured force history data for each individual test is summarized in Appendix C. The kinetic energy versus peak force is plotted for all experiments (DS1 and DS2) in Figure 3.5, separated according to the SHI size. Figure 3.6 provides a view of the same results, but in a smaller kinetic energy range up to 400 J.

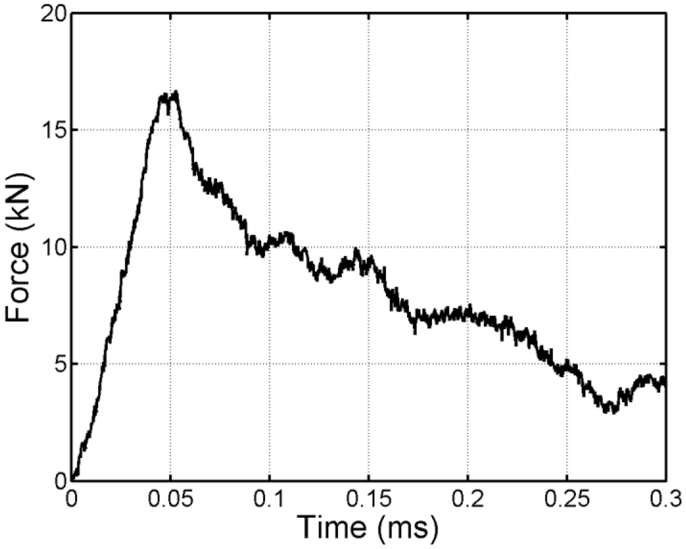

Figure 3.4: Force history from FMB; UCSD Test 202: 50.8 mm diameter SHI at 62.6 m/s (123.6 J)

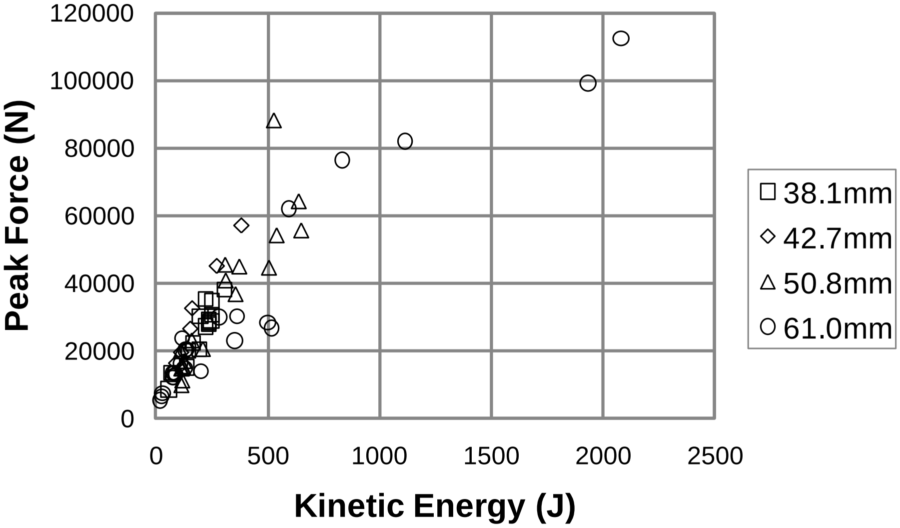

Figure 3.5: Peak force and kinetic energy relationship for all SHI impact tests

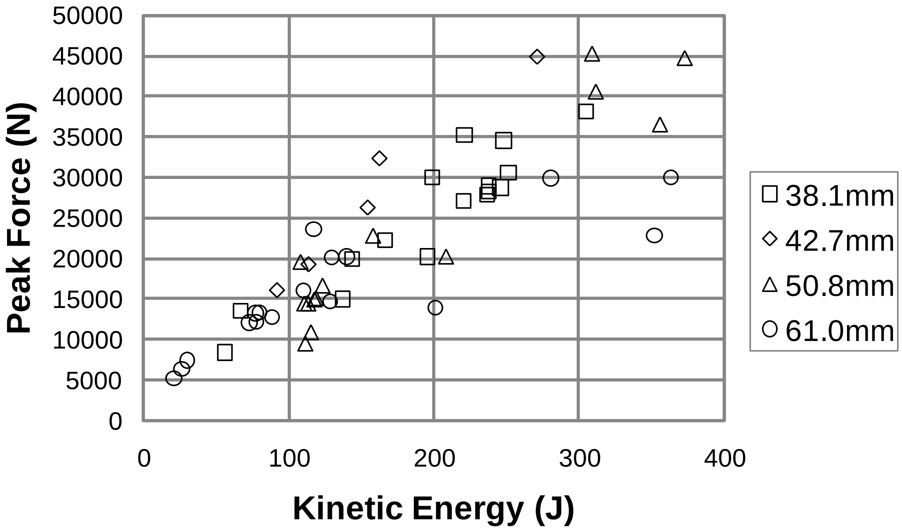

Figure 3.6: Peak force and kinetic energy relationship for SHI impact tests with energies less than 400 J

3.3. Repeatability of Ice Impact

One concern during the comparison of the simulation results to the experimental data was the noticeable scatter in peak force data. To assess the repeatability of the force history data, experiments using 50.8 mm SHI were conducted with multiple repetitions at the same velocity nominally (60 m/s). The force histories plotted in Figure 3.7 show each test is quite consistent in terms of peak force magnitude and impulse (in 1 ms window capturing entire force history data) as well as the overall transient response. Additional test information is summarized in Table 3.1. The results give confidence that the scatter in the data can exist for various reasons, including pre-existing flaws or issues with ice integrity at impact. With careful examination of the SHI projectile before each test and the use of high speed video observation to confirm integrity (i.e., ball not broken) at the time of impact, the four tests are found to be quite consistent and repeatable.

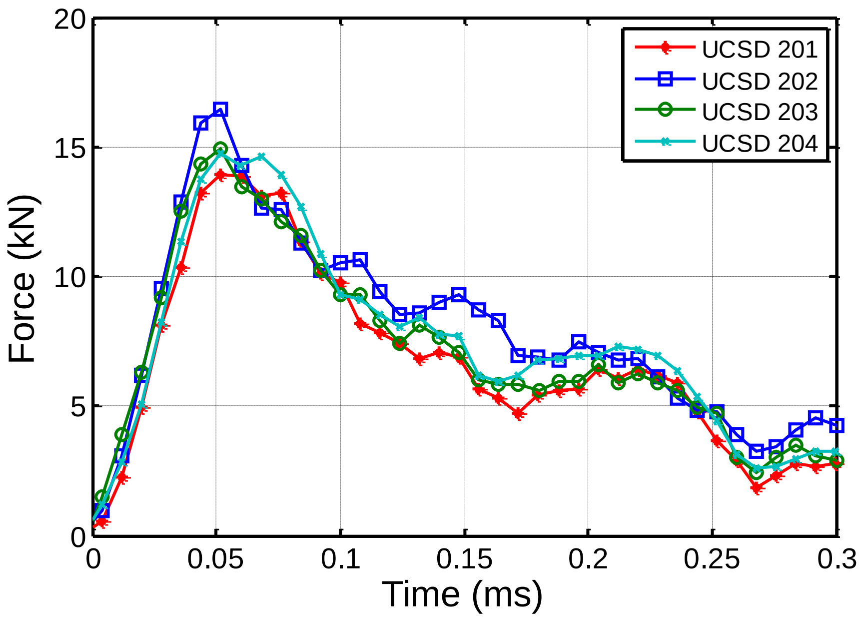

Figure 3.7: Repeated tests of 50.8mm SHI size at velocities ranging between 59.3 m/s and 62.6 m/s (targeted velocity of 60 m/s)

Table 3.1: Experimental measured quantities of repeated impact test study

Test ID	Diameter (mm)	Velocity (m/s)	Kinetic Energy (J)	Peak Force (kN)	Impulse (N-s) (1 ms window)
UCSD 201	50.8	59.3	111	14.5	2.95
UCSD 202	50.8	62.6	124	16.7	3.4
UCSD 203	50.8	61.2	118	15.0	3.12
UCSD 204	50.8	61.2	119	15.1	3.03

CHAPTER 4. NUMERICAL MODEL DEVELOPMENT

4.1 Model Description

A numerical model of a SHI projectile during impact was developed using the Abaqus/Explicit finite element solver. The addition of strain rate dependent material parameters is the main improvement from the previous Abaqus model [4]. Several other issues were also addressed during the development of the material model.

The model of the SHI projectile and rigid flat target was built using a Lagrangian mesh. A quarter-model of the spherical projectile, shown in Figure 4.1, with symmetry boundary conditions, was used in all analyses. The target consists of one layer of elements with all nodes rigidly constrained to zero displacement to represent a rigid target. The spherical projectile consists of 8-noded reduced integration hexahedral elements (C3D8R element type in Abaqus). Hard, frictionless contact was defined between the projectile and the target. The model was solved with a bulk viscosity value of 1.2 based on the sensitivity studies performed by Park [4].

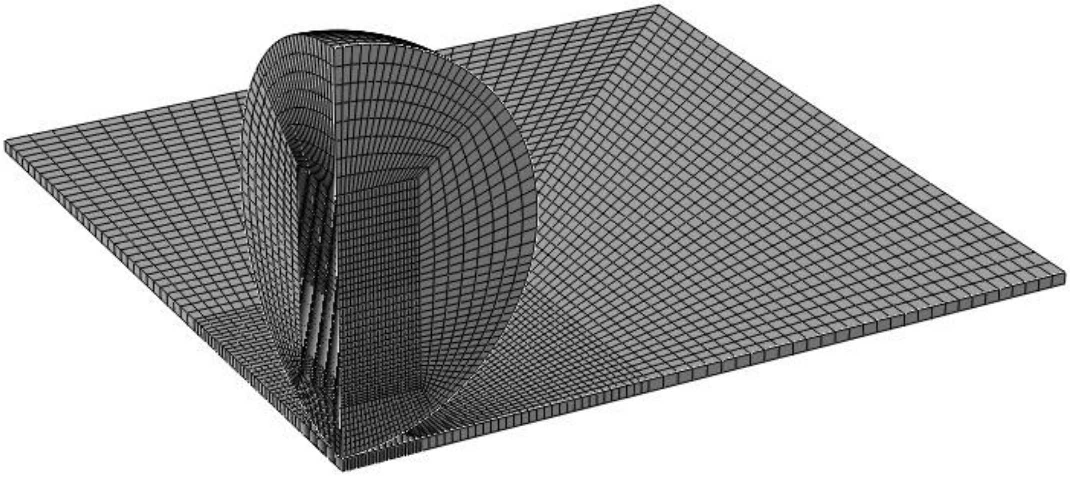

Figure 4.1: Quarter model mesh of SHI projectile and rigid target

4.2. Ice Material Parameters

The ice material model in Abaqus is composed of a simple elastic-plastic behavior with failure criterion based on tensile hydrostatic pressure. The plastic yield stress contains the strain rate dependency using the dynamic compressive strength data reported in the open literature.

4.2.1. Elastic and Mass Properties

The elastic properties of the ice material were chosen based on values found in the literature and used by the previous models [4, 5], which are published values by Petrenko and Whitworth [18]. Previous DYNA3D and LS-DYNA models required shear or bulk moduli, whereas Abaqus requires input of Young's modulus and Poisson's ratio. The Poisson's ratio was simply calculated using the isotropic relations between the elastic constants. The density for SHI (polycrystalline ice) is generally 920 kg/m^3, as reported in literature [3]. The new experiments have a measured SHI density between 870 and 925 kg/m^3. For the present model development and correlation efforts, a density of 900 kg/m^3 was chosen. The elastic and mass model inputs are summarized in Table 4.1.

Table 4.1: Elastic Ice Material Model Inputs

Elastic and Mass Material Inputs	
Young's Modulus: E (GPa)	9.38
Poisson's Ratio: v	0.33
Density: ρ (kg/m^3)	900

4.2.2. Strain Rate Dependent Yield Strength

The additional improvement to the previous Abaqus ice material model [4] is the strain rate dependent yield strength. In previous models, the yield strength was manually varied between 17 to 55 MPa, depending on the size and velocity of the projectile. By implementing the strain rate dependent yield strength, the yield strength varies throughout the volume of the SHI projectile based on the local strain rate of the individual elements, rather than being a constant for the entire projectile volume. The yield strength is defined for the present model based on the compressive strength versus strain rate relationship. As the plastic strain increases above the elastic limit, the stress remains constant at the particular yield stress it started yielding at. This is referred to as a zero plastic hardening modulus, or a perfectly plastic model, since high velocity ice impacts can be considered perfectly plastic [3, 20].

Linear-log curves were fit to the compressive strength versus strain rate data provided by Jones [14] and Kim and Kuene [5]. At the time this phase of the research was conducted, only these two experimental data sets were available to the author, thus Shazly et al. [15] was not included. Because the interest of the model is focused on dynamic strain rates (i.e. greater than 1 s^{-1}), only these two experimental data sets were used since they reported compressive strength data in the range of interest. As shown in Figure 4.2, a starting strength of 5.2 MPa was chosen as the origin of the linear-log curves, at a strain rate of 10^{-1} s^{-1} and continuing beyond the published data to 10^6 s^{-1}. An observation of the strain rates in the numerical simulation showed rates below 10^5 s^{-1}; but strength data were defined above these levels to ensure that there would not be any numerical solution issues if the elements experience strain rates at levels beyond those where the curve terminates.

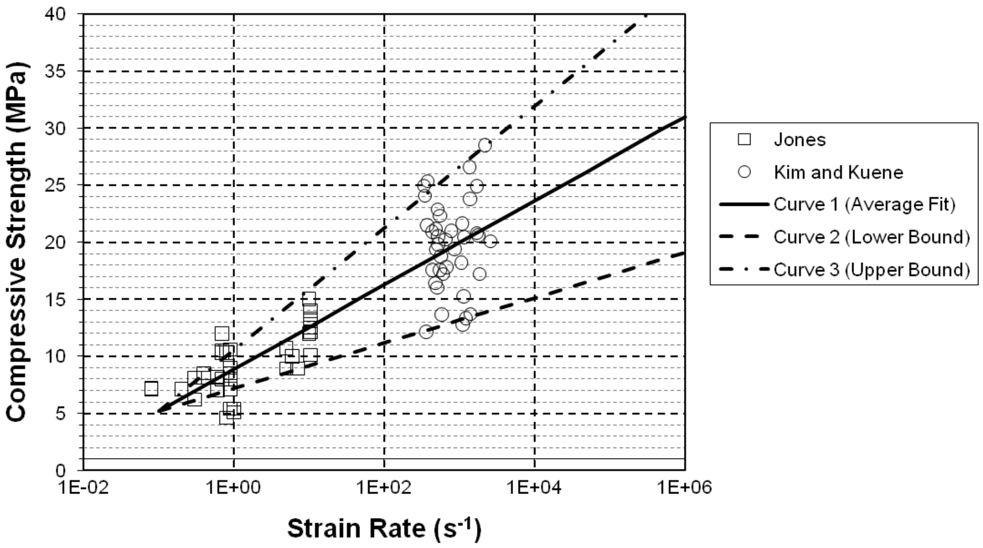

Figure 4.2: Curve fits to compressive strength versus strain rate data

Three curve fits, an average, lower bound, and upper bound, were created to fully include the entire spread of experimental data. The average curve provides a fit through all data whereas the two bounding curves include the upper and lower range of compressive strength at 10^3 s^{-1}, while having the same origin at 10^{-1} s^{-1}. The average curve was used to analyze each test case in the model development, and the lower and upper bound curves were used in select cases. These curves are defined as stress ratios scaling the 5.2 MPa yield strength over the range of strain rates. Appendix A provides exact values used for each curve.

4.2.3. Tensile Failure Pressure Criterion

Failure of the material is implemented based on a non rate-dependent hydrostatic tensile failure criterion. In Abaqus, the tensile failure pressure option has several options. The first is an element deletion option which will remove elements entirely from the simulation when the tensile failure criterion is reached. By removing the elements, however, a very important inertial component is removed from the simulation which is needed to predict the post-peak force portion of the time history curve. Additionally, the removal of these elements causes numerical spikes in the force history due to instantaneous removal of elements that are in contact with the target. Thus element deletion is not used in the present model.

The second option controls the type of failure desired in the pressure stress and deviatoric stresses. There are two options available: ductile and brittle. For the ice material model, it was chosen for the deviatoric stress failure to be “brittle” and the pressure stress to be “ductile”. Under this setting, once the pressure stress reaches the failure threshold, the deviatoric stress will be set to zero and only hydrostatic compression and hydrostatic tension stress up the cutoff value will be allowed in the element. Thus the failed elements behave like a fluid. The tensile failure criterion is illustrated in Figure 4.3, with an example stress state shown at Point O. During the simulation, when the stress state is predicted beyond the cutoff pressure, the new stress state is chosen based on the specified brittle or ductile settings. For settings used in this model, the new immediate stress state post-failure is represented by location two. After this modification of the stress state occurs, the element can no longer carry deviatoric stresses, but only hydrostatic stresses less than the cutoff pressure value (i.e., along the q = 0 line).

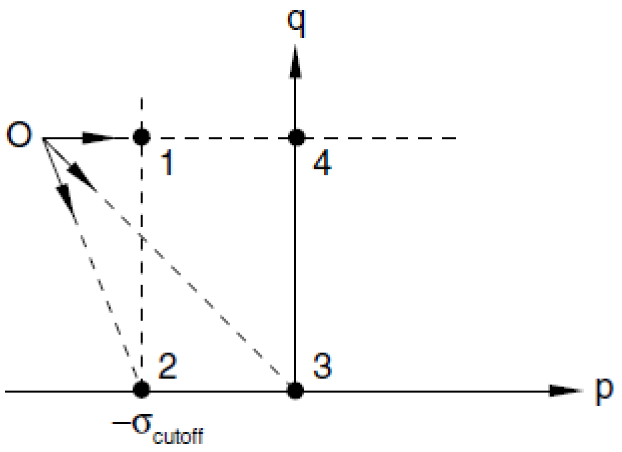

Figure 4.3: Stress state example of pressure (p) and deviatoric (q) stress states for the tensile failure model in Abaqus [21]

In previous models [3, 4], the pressure failure value parameter was manually varied in order to correlate the simulation to the data. Because the goal of the newly developed model is to remove manual tuning of parameters, a constant value was sought to provide close match with all tests. The tensile failure pressures used in the previous Abaqus model [4] ranged between 345 and 6985 kPa. A parametric study was performed using the strain rate sensitive yield strength to determine the appropriate magnitude level of the tensile failure pressure that will provide the best correlation to experimental force time histories. The results of the study, summarized in Figure 4.4, show that a low failure pressure (~689 kPa) is needed to provide good correlation to the experimental data.

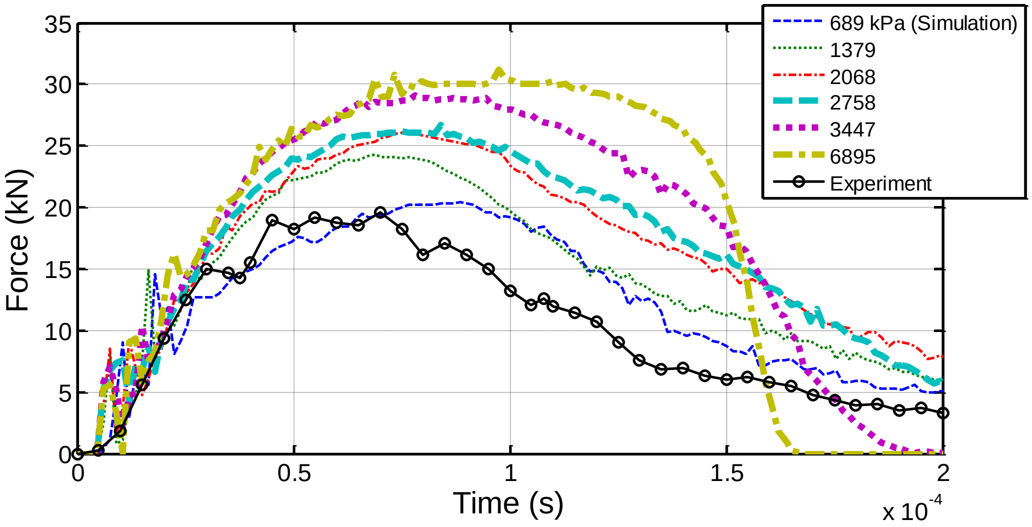

Figure 4.4: Tensile failure pressure study compared with experimental data from Kim et al. Test 49; 50.8 mm diameter SHI at 60.6 m/s (114 J)

After the initial comparison with a large range of magnitudes, a focused study with a condensed range of 345, 517, and 689 kPa tensile failure pressure values was performed. The results of the study performed at a low impact energy (77 J) is graphed in Figure 4.5 and shows only a slight difference in peak force between the 517 psi and 689 kPa curves, but better tail for the lower value. The same study was performed for a higher energy (593 J), plotted in Figure 4.6, show no sensitivity in response to the change in tensile failure pressure in the range of 345, 517, and 689 kPa. Based on these high and low energy cases comparing the effect of the tensile failure pressure, a tensile failure pressure magnitude of 517 kPa was chosen for the final material model.

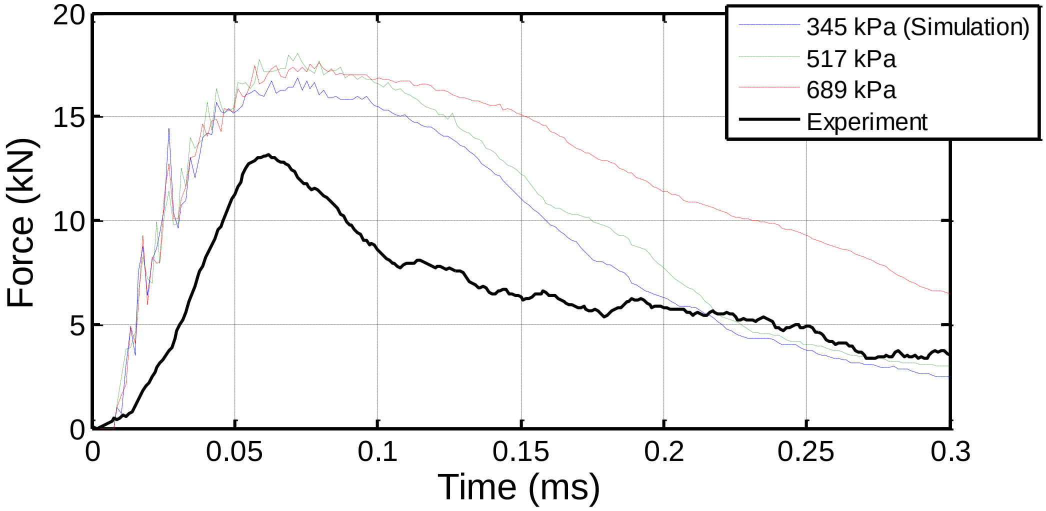

Figure 4.5: Tensile failure pressure at lower pressures with experimental data from Purdue Test 83, a low energy test; 61.0 mm SHI at 37.3 m/s (77 J).

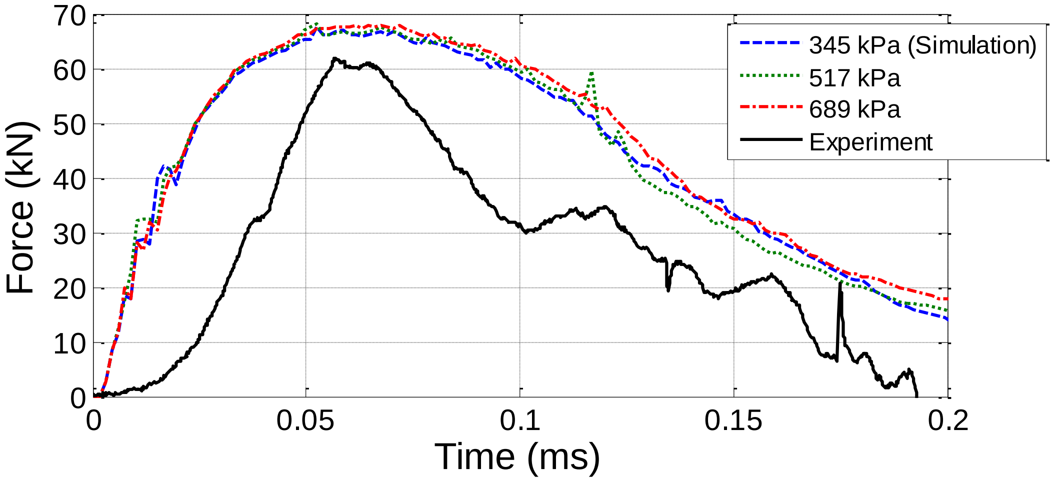

Figure 4.6: Tensile failure pressure at lower pressures with experimental data from UCSD Test 30, a high energy test; 61.0 mm diameter SHI at 105.0 m/s (593 J)

4.3. Software and Mesh Domain

The previous models developed for ice impact have differences in software and in the mesh domain. Three models were made for the LS-DYNA analysis software [2, 3, 10]; one was made in Abaqus [4]. Three models use a Lagrangian projectile mesh [2, 3, 4], while one uses an Eulerian projectile mesh [10].

The LS-DYNA strain rate sensitive model developed by Carney et al. [10] uses an Eulerian-Lagrangian capability, as shown in Figure 4.7, allowing the projectile to be meshed in an Eulerian domain while the target is still meshed in the Lagrangian domain. Because of the large deformation of the ice projectile mesh, a Lagrangian mesh causes the analysis to slow down the time step as elements become highly distorted towards the end of the simulation. It has also been shown that a Lagrangian mesh can take significantly longer to solve than an Eulerian or even Smooth Particle Hydrodynamic (SPH) models [22].

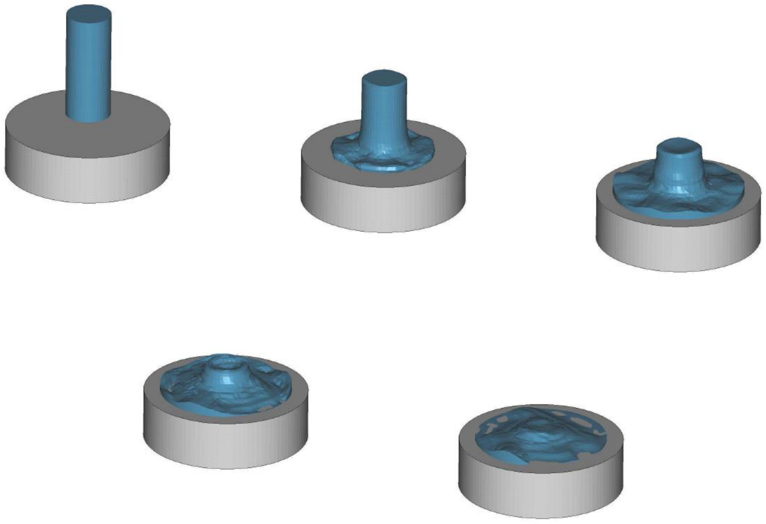

Figure 4.7: Ice cylinder impact simulation [10]

In 2008, Abaqus introduced a Coupled Eulerian-Lagrangian capability. This capability was examined for this project, but the results never matched the desired characteristics produced by the all-Lagrangian mesh. Since the Eulerian-Lagrangian capability in Abaqus was fairly new, the traditional Lagrangian mesh was chosen for the model development and correlation efforts because the major portion of the force impulse happens well before the mesh becomes distorted enough to cause significant numerical problems. As it desired that the material model developed should not be dependent on the mesh domain, the Eulerian-Lagrangian capability could be explored in the future as long as all the same material model options are available for an Eulerian material, as implemented in the Abaqus software.

4.4. Mesh Sensitivity Study

An important part to any finite element simulation model is a convergence study on the mesh size. For SHI simulation, the mesh size was found to be of extreme importance to accurately correlate with test data. In previous models, with material parameters being tuned to best match each test, the mesh convergence could easily be masked by the parameter tuning. With the strain rate dependent strength data included, and the goal of providing a model with no additional manual user input, a recommended mesh size needed to be determined.

A study using four mesh sizes was performed. The mesh seed sizes ranged from 0.381 to 1.27 mm for a 50.8 mm diameter spherical ice projectile, as shown in Figure 4.8. Additionally, a biased mesh, shown in Figure 4.9 was used in the study.

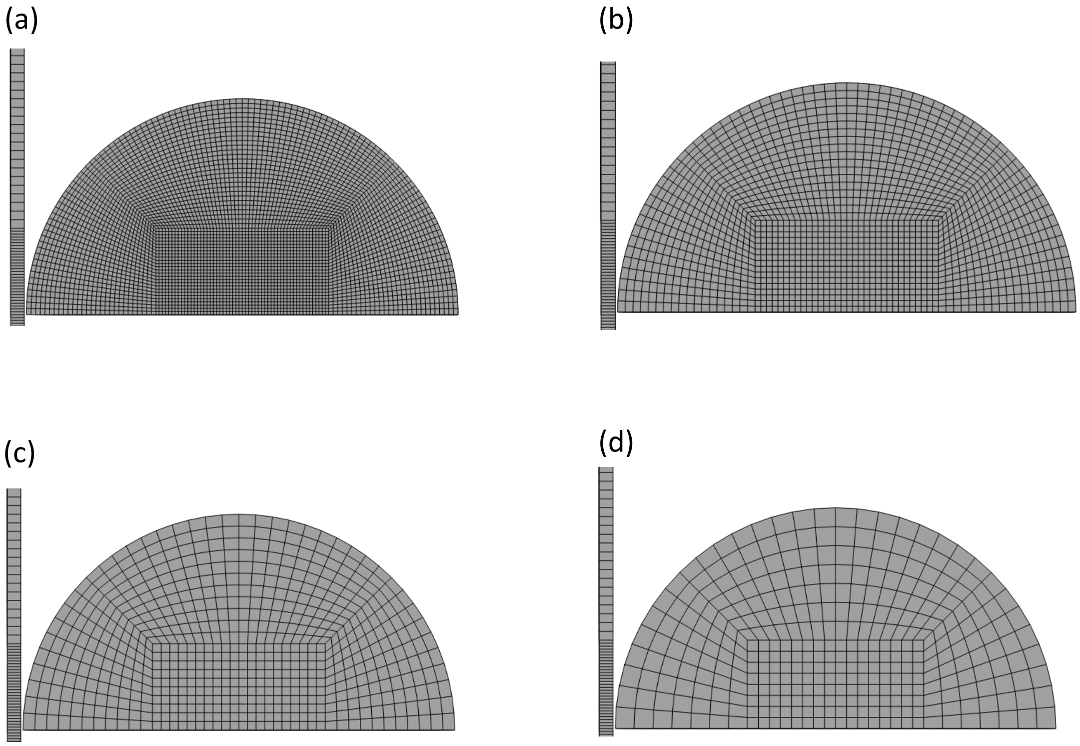

Figure 4.8: Mesh seed sizes of 50.8 mm diameter SHI: a) 0.381 mm b) 0.635 mm c) 1.016 mm d) 1.270 mm

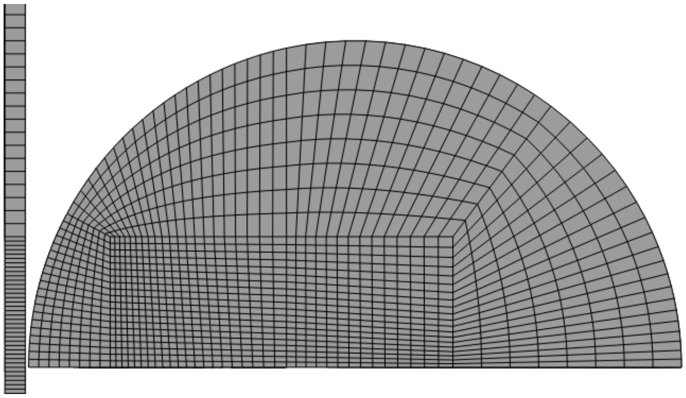

Figure 4.9: Biased mesh of 50.8 mm diameter SHI, smallest element is 0.354 mm

The results, plotted in Figure 4.10, show there is significant change in the shape of the force history as well as in the peak force as the mesh is refined. The solution time was also monitored along with the accuracy of the predicted force. The smallest seed size took nearly twelve hours to solve, while the largest seed size took only five minutes. In effort to improve solve time for correlation study efforts, but also to obtain accurate peak force results, a hybrid seed size was created by biasing the center partition of the ice sphere mesh containing the rectangular elements towards the contact point. The biased mesh, shown in Figure 4.9, allowed for more elements to exist in the area where the stress gradients are the most concentrated, allowing for a better gradient definition. The biased meshed does not produce the same post-peak force tail as the smallest seed size mesh, 0.381 mm, but matches the peak force. The simulation also solved in just over two hours, a significant improvement. The biased mesh was chosen as a compromise between accuracy and the solve time, sacrificing the convergence of the post peak force tail of the predicted force history.

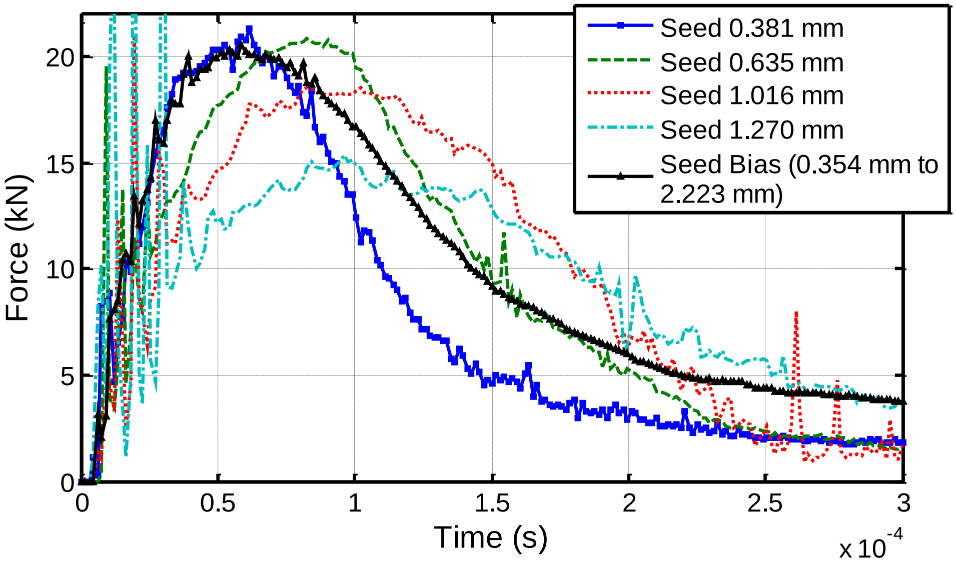

Figure 4.10: Mesh sensitivity study of SHI projectile; 50.8 mm diameter SHI at 60.6 m/s (114 J)

4.5. Summary of Ice Material Model Inputs

A summary of the ice material model input parameters are in Table 4.2. The ice material model input values and other settings can be added to Abaqus using the section of the input file outlined in Appendix A. The Abaqus material model input file syntax can replace the material definition of a temporary material generated if exported from Abaqus/CAE; but it is important to note that the input file is the only place available to specify the tensile failure pressure criterion (at present since Abaqus version 6.9-2).

These following model settings should be checked when using this model:

- Mesh sensitivity shows a minimum size of 0.381 mm, or 0. 75% of SHI diameter is required near the impact location.
- A linear of bulk viscosity of 1.2 and quadratic bulk viscosity of 0 [4] is specified in the Abaqus/Explicit settings.
- “Hard” and frictionless contact is defined between the surfaces of the projectile and target.

Table 4.2: Summary of Ice Material Model Inputs

Ice Material Model Inputs		**Additional Comments**
Young’s Modulus: E (GPa)	9.38	[4, 5, 18]
Poisson’s Ratio: v	0.33	Based on isotropic relations using bulk and shear moduli [4, 5, 18]
Density: ρ (kg/m^3)	900	Measured densities range from 870 to 925 kg/m^3
Tensile Failure Pressure	517 kPa	Chosen based on parametric study
Yield Stress	5.2 MPa	Specified for $\varepsilon_p = 0$ and $\varepsilon_p = 1$
Rate Dependent Yield Stress	[Tabular input]	See Appendix A for data for C1 – Avg., C2 – Lower, and C3 - Upper

CHAPTER 5: SIMULATION RESULTS AND EXPERIMENTAL COMPARISON

Impact tests of SHI performed by Kim et al. [6], several contributors both at Purdue University and the University of California at San Diego, and new additional tests provided key data for comparison of the numerical model results. Each experiment condition contains a transient force history during the hail impact event, lasting approximately 300 µs. The force history data were processed further to look at trends such as peak force versus kinetic energy and the total impulse. These comparisons are performed and presented in this chapter.

5.1. Simulation Results

Many numerical simulations were conducted at different SHI sizes and velocities to correlate with select experimentally measured force histories. Additional simulations were conducted for SHI size and velocity not matching any experiments in order to better populate the overall peak force versus kinetic energy trend. The force histories are compared in detail to confirm accuracy of the simulation results and the simulation-predicted peak force versus kinetic energy relationship is compared to all the simulations.

5.1.1. Force History Comparison

The force histories are compared for simulations solved at nominally the same size and velocities matching select experimental conditions. All simulations were conducted using the material model definitions presented in the previous chapter. As described in Tables 5.1 and 5.2, simulation results were compared to experimental force history data using the average curve (C1 – Avg.) and the lower bound curve (C2 – Lower). The simulation time varies between 0.15 and 0.3 ms. Figures 5.1 through 5.8 show the comparison of model-predicted force histories for the tests summarized in Table 5.1 to 5.2. Additional simulations were conducted for conditions not related to any specific test. All simulation force histories are plotted in Appendix D with comparison to experimental data where available.

A strong correlation between the experimental and simulation force histories is shown for several tests: UCSD Test 11, UCSD Test 29, Kim et al. Test 49, and Kim et al. Test 48. The rise and fall trend of the force history matches in magnitude and time to peak force, and the impulse magnitudes calculated (over the simulation length) also match closely between experiment and simulation. The remaining tests do not match as strongly (e.g., UCSD Test 195, UCSD Test 197, UCSD Test 184, Purdue Test 28, and Purdue Test 124), underestimating the peak force from 10 to 50% or showing less comparison to the force history. When using the C1 –Avg. yield strength versus strain rate relationship, the simulation peak force can over predict the experimental peak force (in the case of UCSD Test 197) by over 50%. It is important to note the different yield strength curves used in the correlation since the peak force magnitude is strongly affected by this choice. When using C2 – Lower, there is a better correlation than when using C1 – Avg. However, in one case, UCSD Test 11, the force history more closely matches when using C1 – Avg. In general though, more tests compare well with the lower bound of the compressive strength versus strain rate data. Thus the lower bound curve is suggested when correlating to experimental SHI impact tests, whereas the average or upper curves should be used when a more conservative estimate is needed.

Table 5.1: Summary of ice impact experimental quantities

Data Set	Test ID	Diameter (mm)	Velocity (m/s)	Kinetic Energy (J)
DS2	UCSD 11	50.8	144.3	641
DS2	UCSD 29	50.8	109.9	356
DS2	UCSD 195	50.8	60.6	114
DS1	Kim et al. 49	50.8	61.9	108
DS2	UCSD 197	50.8	82.2	209
DS1	Kim et al. 48	50.8	104.6	309
DS2	UCSD 184	61.0	81.2	363
DS2	Purdue 28	61.0	45.4	110
DS2	Purdue 124	61.0	189.2	1933

Table 5.2: Comparison of experimental and simulation results

		Test Results		Simulation Results			
Data Set	Test ID	Peak Force (kN)	Impulse (N-s)*	Simulation Duration (s)	Yield Strength Curve	Peak Force (kN)	Impulse (N-s)*
DS2	UCSD 11	64.3	6.67	0.2	C1	59.2	7.23
DS2	UCSD 29	36.6	4.95	0.3	C2	33.6	5.38
DS2	UCSD 195	14.5	2.17	0.3	C2	16.9	3
DS1	Kim et al. [3] 49	19.6	2.6	0.3			
DS2	UCSD 197	20.3	3.12	0.15	C1	32.8	3.39
DS1	Kim et al. [3] 48	45.4	4.06	0.15	C1	38.8	4.26
DS2	UCSD 184	30.0	3.09	0.15	C1	43.5	5.07
DS2	Purdue 28	16.0	1.07	0.15	C1	19.8	2.17
DS2	Purdue 124	99.2	9.17	0.15	C2	118.6	12.78

*Impulse computed over the time duration of simulation

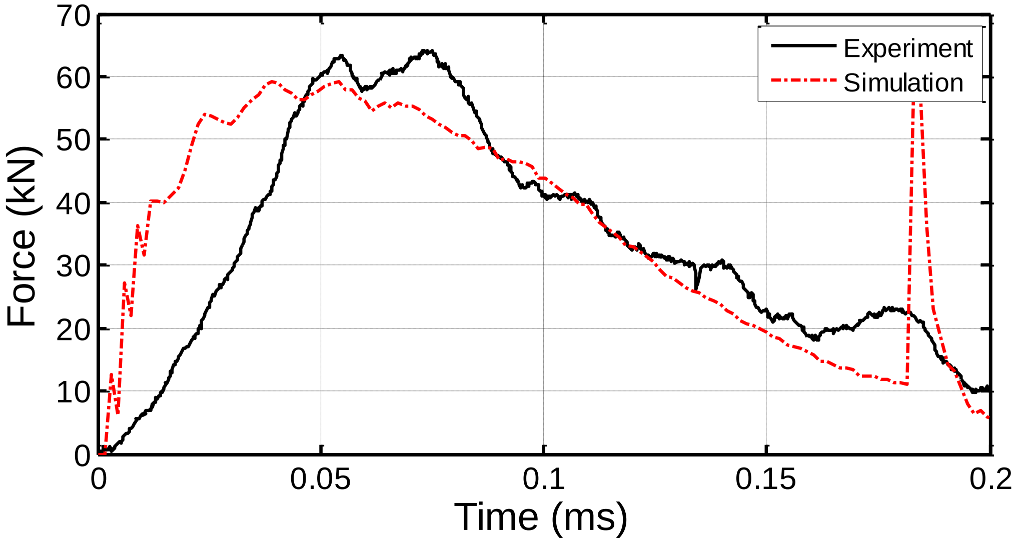

Figure 5.1: Simulation results: UCSD Test 11 comparison using C1 –Avg.; 50.8 mm sized SHI at 144.3 m/s (641 J)

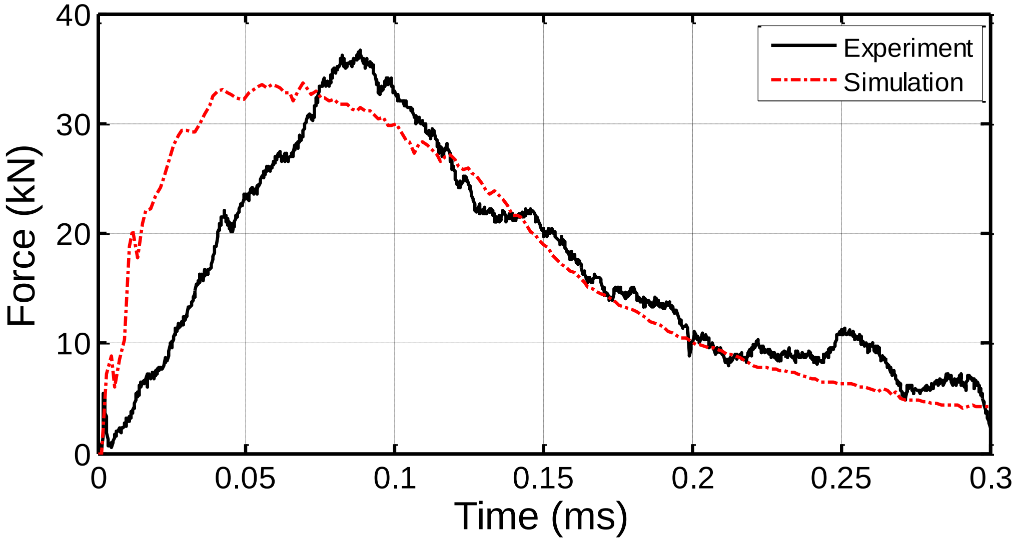

Figure 5.2: Simulation results: UCSD Test 29 comparison using C2 - Lower; 50.8 mm sized SHI at 109.9 m/s (356 J)

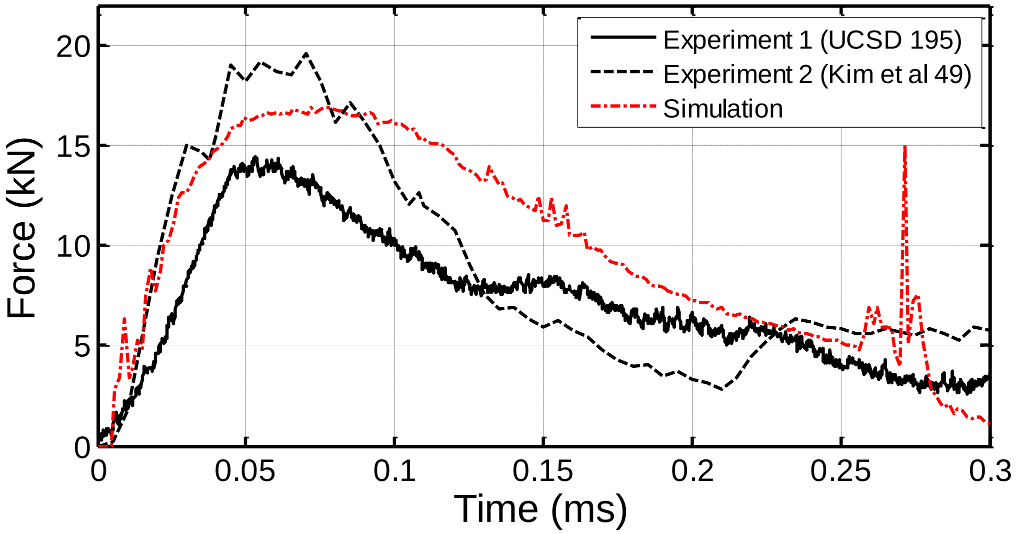

Figure 5.3: Simulation results: UCSD Test 195 and Kim et al. Test 49 comparison using C2 - Lower; 50.8 mm sized SHI at 60.6 m/s (114 J)

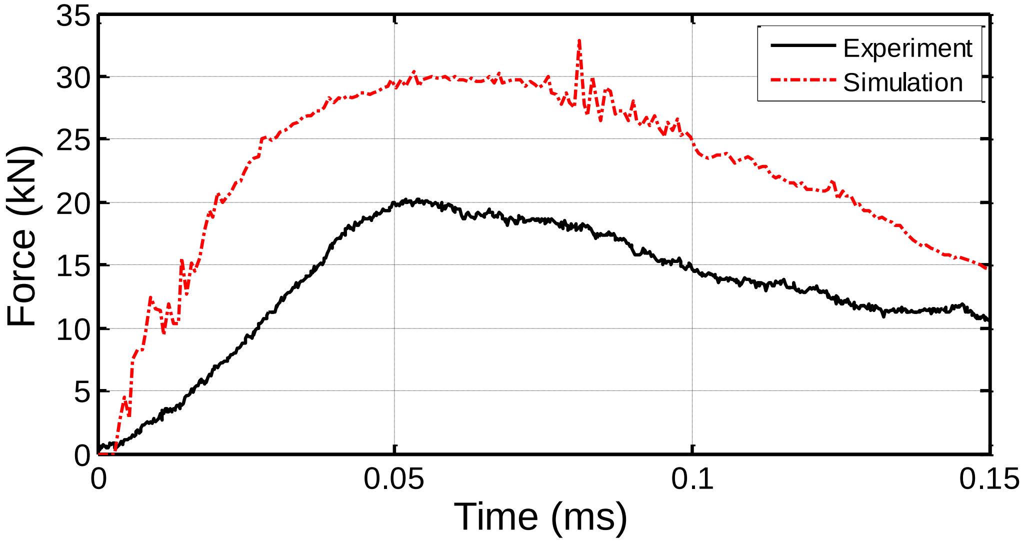

Figure 5.4: Simulation results: UCSD Test 197 comparison using C1 – Avg.; 50.8 mm sized SHI at 82.2 m/s (209 J)

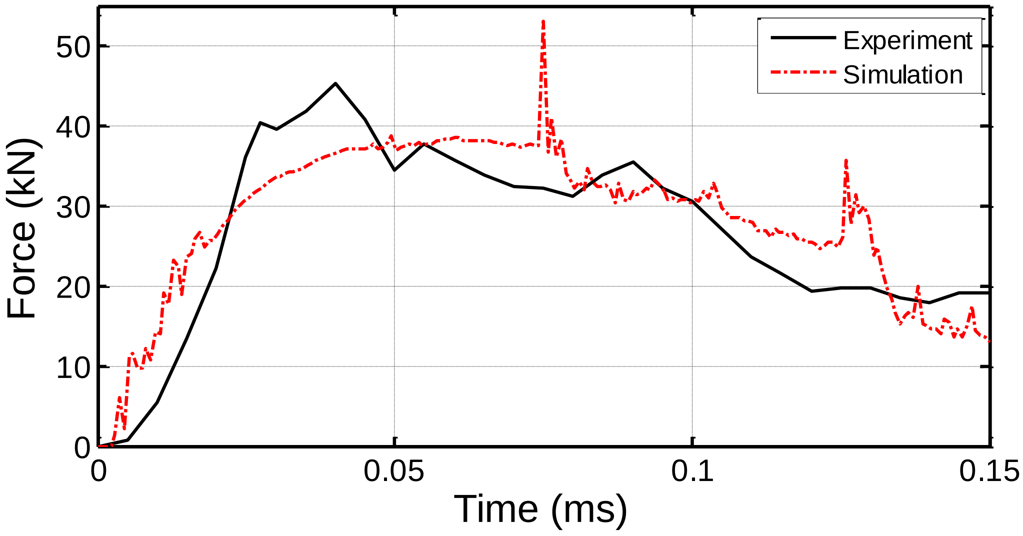

Figure 5.5: Simulation results: Kim et al. Test 48 comparison using C1 – Avg.; 50.8mm sized SHI at 104.6 m/s (309 J)

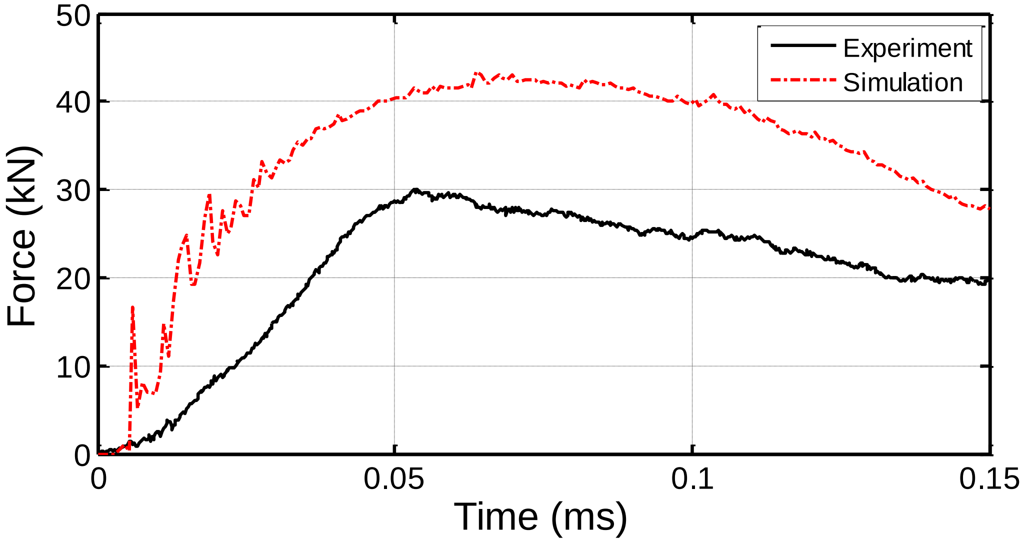

Figure 5.6: Simulation results: UCSD Test 184 comparison using C1 – Avg.; 61.0 mm sized SHI at 81.2 m/s (363 J)

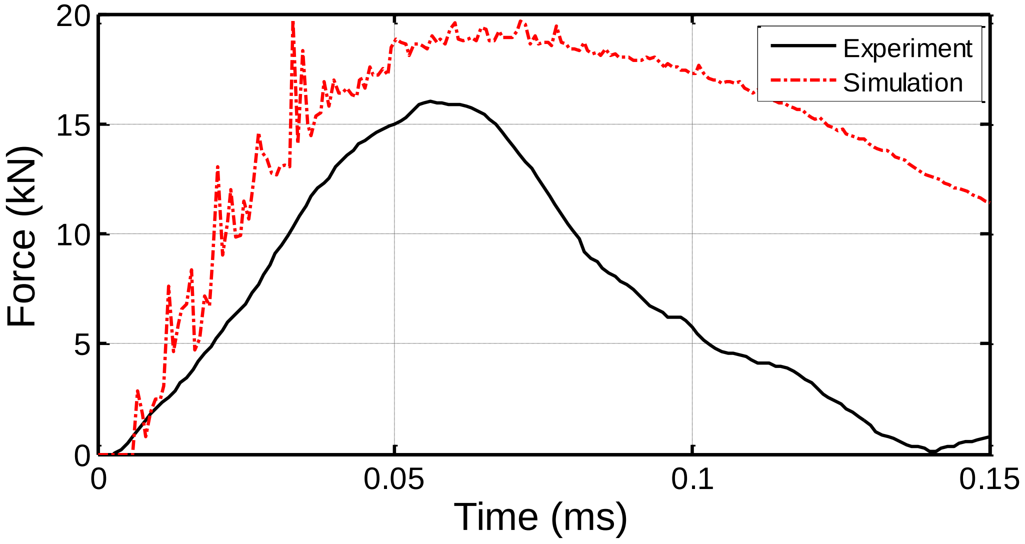

Figure 5.7: Simulation results: Purdue Test 28 comparison using C1 – Avg.; 61.0mm sized SHI at 45.4 m/s (110 J)

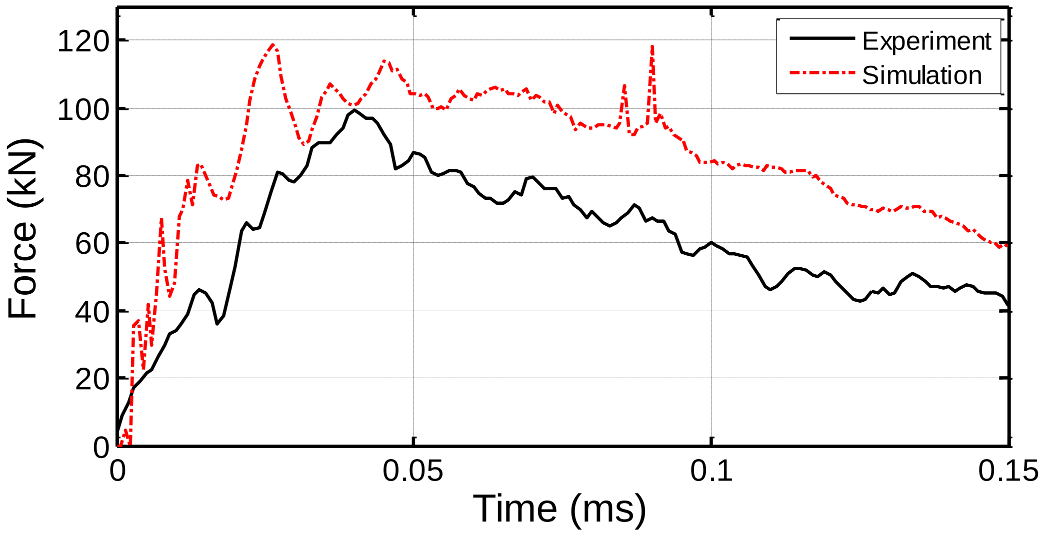

Figure 5.8: Simulation results: Purdue test 124 comparison using C2 – Lower; 61.0mm sized SHI at 189.2 m/s (1933 J)

5.1.2. Peak Force Versus Kinetic Energy

In all, 34 simulations were performed using the average fit (C1 – Avg) to the compressive strength data. Five simulations were performed using the lower bound curve (C2 - Lower) curve and five simulations were performed using the upper bound curve (C3- Upper). A comparison of the peak forces versus kinetic energy is plotted in Figure 5.9 with three power curve fits to each set of peak forces predicted by the three compressive strength curves. Figure 5.10 shows the same results comparison, but at a lower range of kinetic energy (less than 400 J). A summary of all simulations is tabulated in Appendix D.

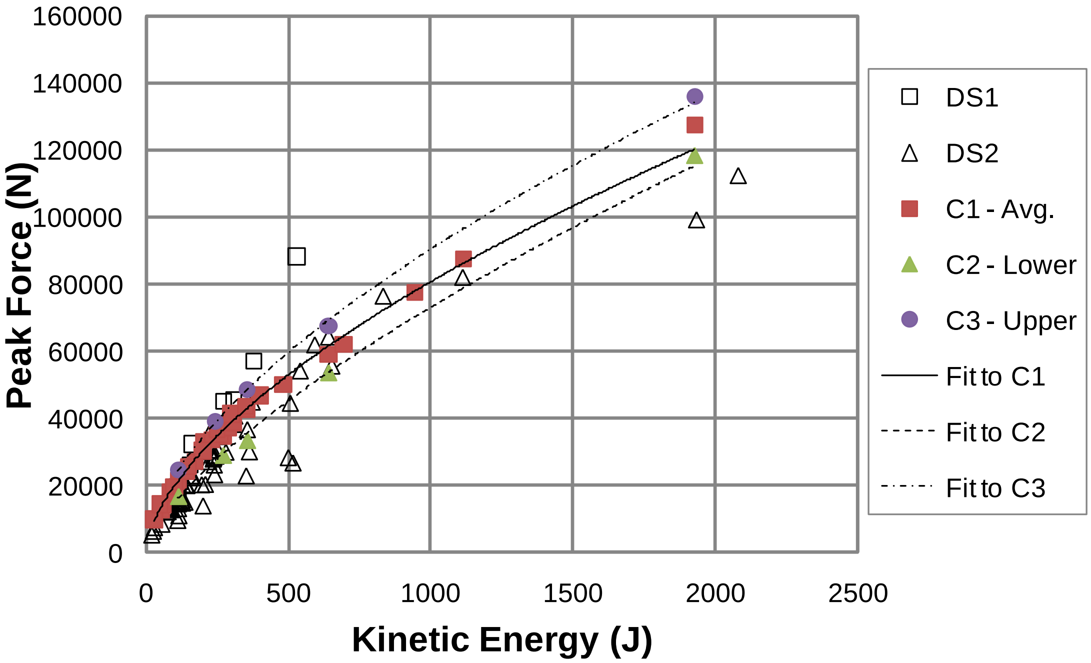

Figure 5.9: Kinetic energy and peak force relationship showing all simulation and experimental results

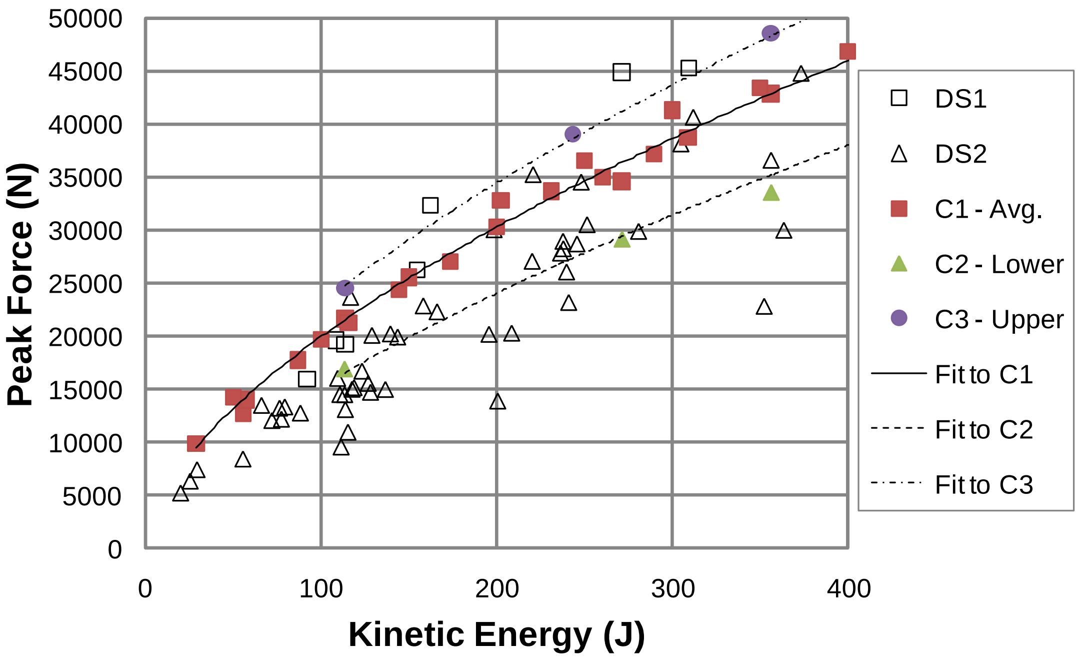

Figure 5.10: Kinetic energy and peak force relationship showing simulation and experimental results for kinetic energy range less than 400 J

As shown in Figures 5.9 and 5.10, the simulation results match the overall peak force trend of the experimental data, with a tendency to over predict the peak force at energies below 100J. The upper bound curve (C3 – Upper) shows peak forces at the high range, but not greater than the highest recorded data points, with a closer match the higher peak forces in DS1. The average curve (C1 – Avg.) predicts peak forces at the upper end of the scatter in data set DS2, composed entirely of monolithic ice. The lower bound curve (C2 - Lower) compares closest with the average peak force magnitudes in data set DS2. It is noted that the lower bound curve (C2 – Lower) does not bound the lower scatter in the experimental data. This is attributed to the variability in ice quality which might have produced such low peak forces.

5.2. Model Correlation with High Speed Video Observation of SHI Impact

Under observation by high speed video cameras (Phantom V. 7.3), several tests were conducted using the gas cannon and force measurement bar apparatus to study the process of failure propagation of the ice sphere in relation to the force history generated during the impact event. Videos were recorded at a frame rate of 90,000 frames/second (one frame every 11 µs). With the high frame rate, several frames were recorded before the development of peak force, providing direct visual observations that are insightful to the dynamic failure progression of the ice sphere.

The force history measurement in Figure 5.11 is from test UCSD 195 in data set DS2, produced by a 50.8 mm diameter SHI impact test at 60.6 m/s. The vertical grid marks in Figure 5.11 correspond to the select times during the impact event for which video frames are shown in Figure 5.12. The progression of images shows the ice sphere moving from left to right at times following initial contact (t = 0 µs) with the force measurement bar end cap. Five of the frames occur before the peak force, showing the formation and progression of the cracks within the SHI, before peak force occurs at a time between frames at 47 and 58 µs after initial impact.

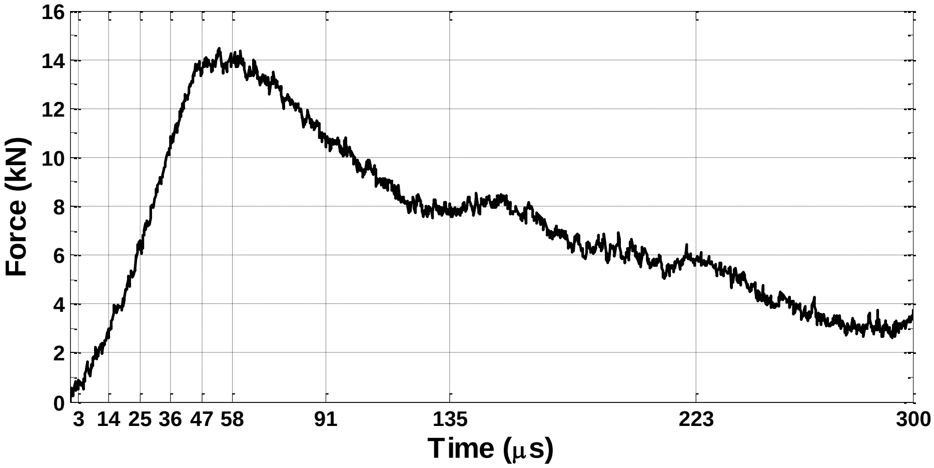

Figure 5.11: Experimental force history of Test; 50.8 mm SHI at 60.6 m/s (114 J)

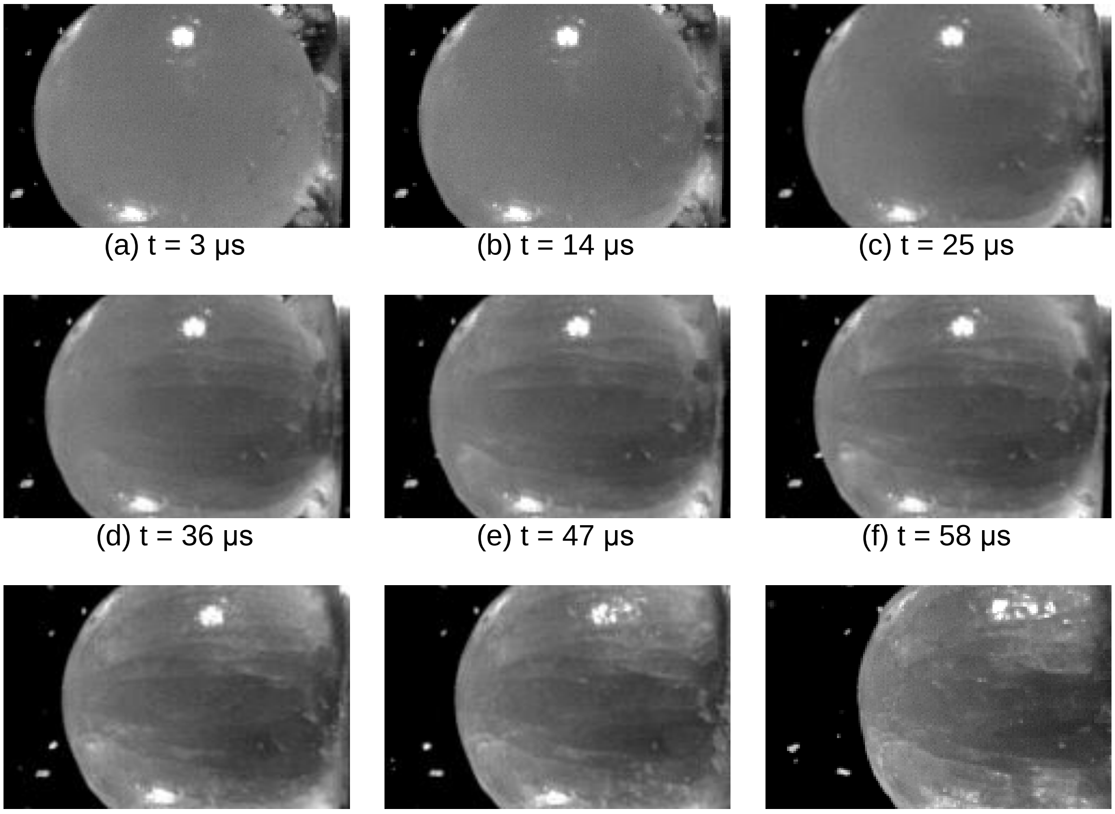

(a) t = 3 μs
(b) t = 14 μs
(c) t = 25 μs
(d) t = 36 μs
(e) t = 47 μs
(f) t = 58 μs
(g) t = 91 μs
(h) t = 135 μs
(i) t = 223 μs

Figure 5.12: High speed video frames of SHI impact on force measurement bar; Test UCSD 195 with 50.8 mm SHI at 60.6 m/s (114 J)

The cracks growing away from the initial impact location appear in Figure 5.12 to be longitudinally oriented with the direction of travel, with cracks terminating just before the rear face of the projectile (see Figures 5.12a to 5.12e). More cracks then develop in between the initial length-wise fractures (see Figures 5.12f to 5.12h). After this point, the projectile loses its overall spherical form (see Figure 5.12i). The force history begins decreasing after 58 μs (Figure 5.12e) which corresponds to when the transverse cracks start developing and the ice sphere is essentially breaking down into a collection of large ice fragments and powder. This timeframe marks a critical transition from elastic/ structural behavior to a momentum transfer of impinging broken ice debris, represented by the decreasing force trend. By 223 μs, the force is half of the peak value, despite the ice starting to lose its overall spherical shape. Beyond this point, the ice projectile continues to lose momentum via creation of new fracture surface area and transverse redirection of the crushed ice debris. It is significant to note, however, that the major portion of the impact event, namely development of peak force, occurs at a fast timescale, typically between 50 to 100 μs after initial impact.

The experimentally-observed cracking phenomenon has been predicted qualitatively by the simulations. Due to the tensile failure pressure criteria, when an element in the ice material reaches the cutoff pressure, all deviatoric stresses are set to zero. With a corresponding ice impact simulation predicting comparable force history results, which can been seen in Figures 5.11 and 5.13, the morphology of failed elements, shown in Figure 5.14, follows the crack patterns visible in Figure 5.12. Figure 5.14 has been created by viewing elements in the simulation which have a non-zero shear stress component and removing from view elements with a zero shear stress component. In this way only the failed elements are removed from the view. It is important to state that the elements removed from the view are not removed from the simulation. For comparison, three sequential views of the deformation including the failed elements are shown in Figure 5.15. During the numerical solution, these failed elements can still carry pressure stresses in compression and tensile hydrostatic stresses up to the pressure failure criterion cutoff value. Inclusion of these failed elements is important as they play a role in the post peak force momentum transfer which defines the tail of the force history.

Vertical grid lines in Figure 5.13 correspond to the images showing failed elements in Figure 5.14. For better clarity, the quarter model results were patterned cylindrically to represent a view of a complete SHI projectile. Note that Figure 5.14 shows the failed elements propagating from the impact front face to the backside, extending in length until the time of peak force, predicted to occur at 75 μs (see Figure 5.13). While the model-predicted breakup of the ice sphere is not documented throughout the entire simulation time duration, the initial response with the length-wise cracks forming up until the development of peak force demonstrates that the model is representing the basic physics of the ice sphere response up until the formation of peak forces. However to a lesser degree of representation, the experimentally observed lateral spreading of the broken ice debris flow (see Figure 5.16) following well after the peak force at t = 300 μs is not well predicted in the simulation deformation at the same time (see Figure 5.15). Therefore it is important to distinguish that this model is particularly suited for predicting early time-scale events such as localized failures in the structures impacted by high velocity hail ice, and not the spray pattern and debris flow of ice after it strikes the surface.

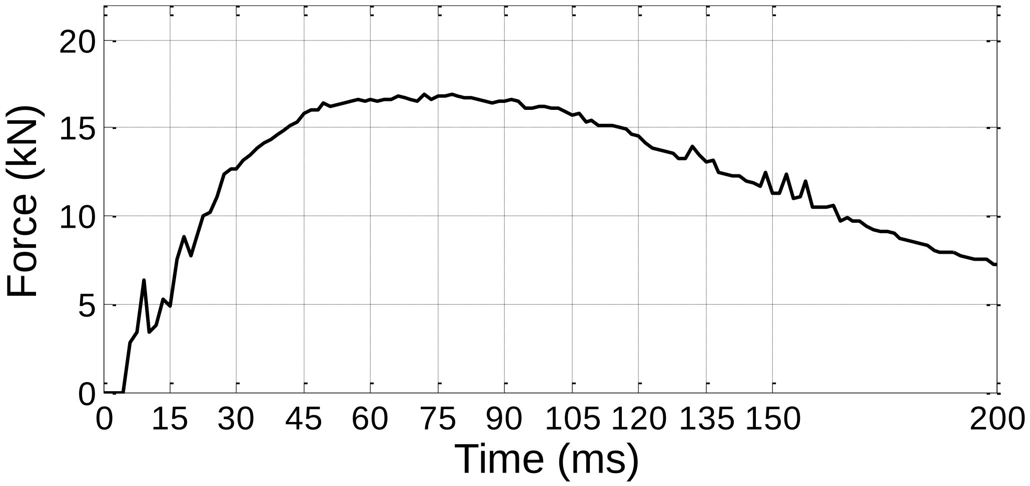

Figure 5.13: Simulation force history with simulation view output frame gridlines marked; 50.8 mm diameter SHI at 60.6 m/s (114 J)

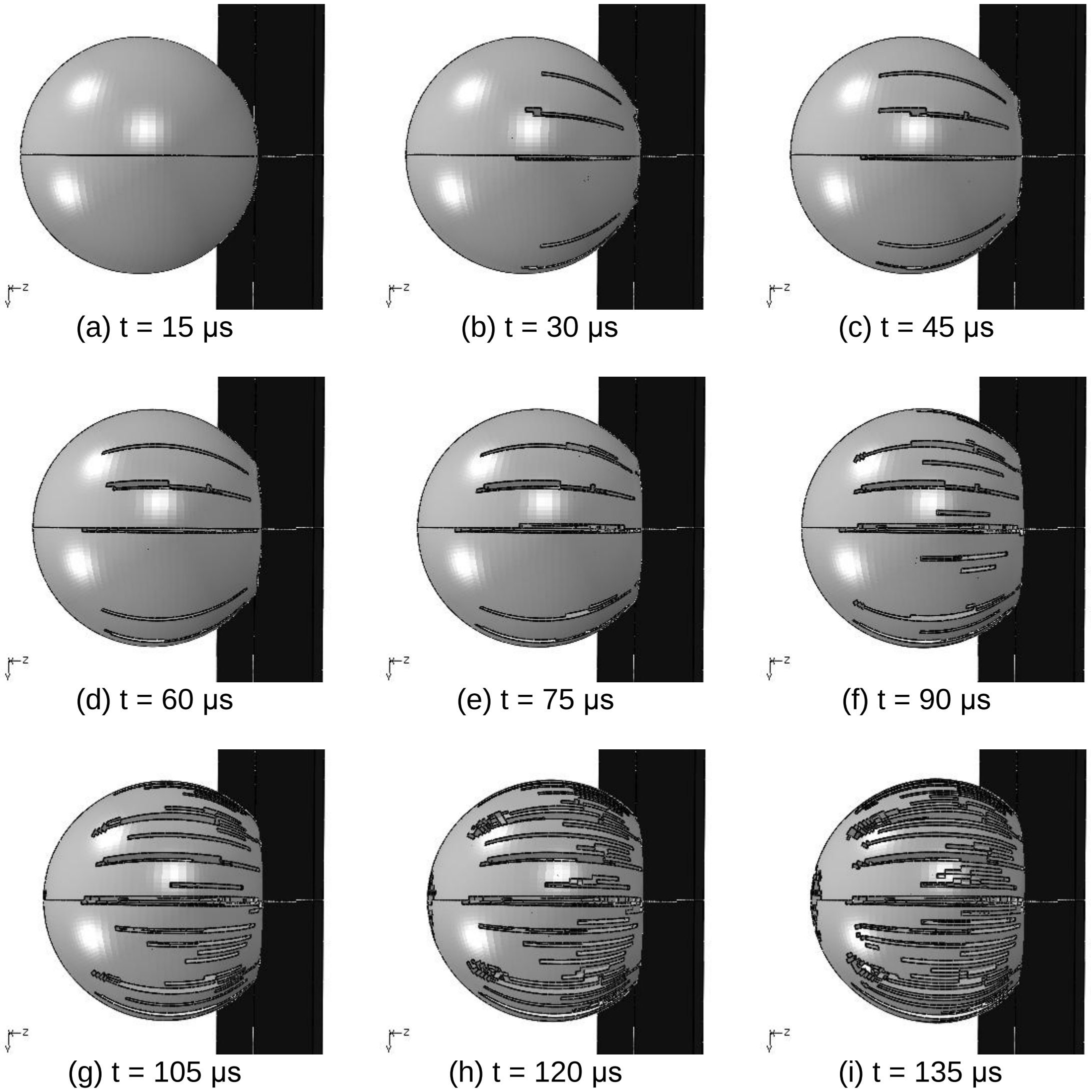

(a) t = 15 μs (b) t = 30 μs (c) t = 45 μs

(d) t = 60 μs (e) t = 75 μs (f) t = 90 μs

(g) t = 105 μs (h) t = 120 μs (i) t = 135 μs

Figure 5.14: Deformation of cylindrically patterned view of quarter-symmetric simulation, at 15 μs spacing, with elements failed by tensile failure pressure criterion removed from the viewport; 50.8 mm diameter SHI at 60.6 m/s (114 J)

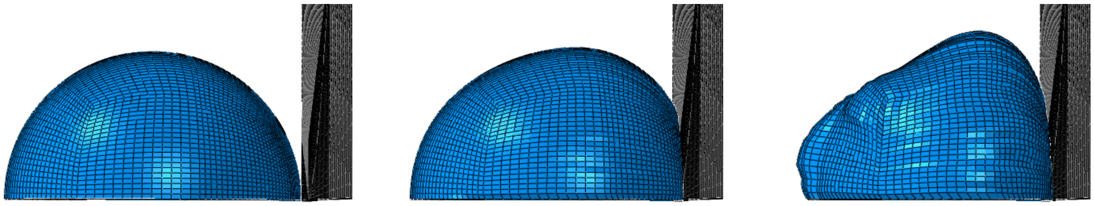
(a) t = 0
(b) t = 120 μs
(c) t = 300 μs

Figure 5.15: Deformation predicted by simulation at t = 0, 120, and 300 μs with all elements shown; 50.8 mm diameter SHI at 61 m/s (114 J)

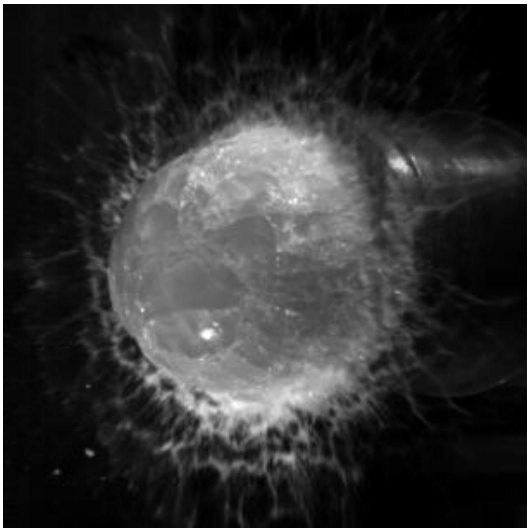

Figure 5.16: High speed video frame of ice impact at 300 μs; 61.0 mm diameter SHI at 61.8 m/s (201 J)

CHAPTER 6: DISCUSSION AND CONCLUSIONS

A strain rate dependent material model was developed for use in the commercial finite element analysis software Abaqus/Explicit to simulate the impact of spherical-shaped hail ice. The simulation results compare well with experimental measurements of forces generated by SHI impact tests. The material model incorporated three bounding compressive strength versus strain rate curves based on measured rate-dependent strength data. A lower bounding curve shows better comparison to the majority of the ice sphere impact peak force measurement data, while an average curve provides an upper bound to all of the experimental data. The upper bounding curve predicts a conservative force history with peak forces being generally greater than the majority of the data set.

High speed video observation of the ice sphere impact event provides insightful information into the dynamic progression of damage within the SHI projectiles during impact. A visual comparison of the simulation-predicted ice sphere fracture process to the crack growth observed in the experimental videos show the tensile pressure failure criterion captures the key mechanism that simulates breakup of the ice sphere, particularly during the early stages of the impact event. Observed experimentally and predicted by the simulations, when the cracks reach near the back end of the sphere, the impact force reaches its peak value and thereafter decreases as the ice sphere further breaks down into smaller fragments. Thus, the forces created by high velocity ice impact can be defined by two major phases: (i) elastic/structural response during initial time following first contact in which cracks develop and the impact force is increasing, and (ii) fragmentation and cracking which imparts mainly a momentum based loading that is characterized by the decreasing force trail following the peak force.

From the model development process, several important conclusions can be drawn:

- A low tensile failure pressure is needed to match the experimental data. This tensile failure pressure criterion is responsible for the crack-like failure phenomenon seen in both the simulation and the experiments.
- The mesh of the projectile must be fine enough (0.354 mm element size at impact front face) to accurately predict the force history. The mesh sensitivity shows the front end mesh drives the rise of the force and peak force, while the mesh in the back side of the projectile can affect the tail of the simulation. A larger mesh can be used in the rear of the sphere (i.e., a biased mesh) to improve simulation time.
- A Lagrangian domain mesh can be used for spherical ice impact simulation. The model can be solved in practical time duration (2 to 8 hours) for a simulation time that is no longer than the time required to accurately capture the force impulse (0.15 to 0.3 ms). Simulations where long durations are needed, such as the study of penetration damage and failed ice debris flow, an Eulerian or Smooth Particle Hydrodynamic formulation of the projectile should be considered.
- The simulation model presented is well suited for predicting early time-scale events such as localized failures in the structures impacted by high velocity hail ice, but not the spray pattern and debris flow of ice after it strikes the surface.

Recommendations for future improvements for the material model and usage are:

1. Further refinement of the material model so as to predict the more sharp force peak measured in the experimental data. The simulation results show a more gradual change force peak than observed in the experimental data.
2. Studying the material model's transferability to the Eulerian capability in Abaqus.

APPENDICES

Appendix A. Abaqus File Inputs

The contents in this Appendix describe the ice material model input syntax for Abaqus/Explict and the model settings used during the correlation of the simulations to experimental data. The material input described is only a section of the entire model input file (*.inp) needed to submit a simulation in Abaqus. It is expected that the user has an understanding of the structure of an Abaqus input file. More information regarding the input file structure can be found in the Abaqus Documentation [21]. It is recommended the user has already set up and solved (or shown a simulation begins), in Abaqus/Explicit, an impact simulation using their projectile and target meshes. Details on creating and meshing the quarter-symmetric SHI sphere are presented in Appendix B. However, unless simulating a quarter-symmetric target or normal impact, a half-sphere or even full-sphere may need to be used (See Park's [4] Appendix B for details on meshing and creating a full sphere projectile). Thus, the user is responsible for understanding and properly defining the boundary conditions for their projectile and target in their impact simulation.

A.1. Material Input

The only route of implementing this material is to manually edit an input file outside the Abaqus/CAE framework. The *TENSILE FAILURE keyword is not available for input via Abaqus/CAE, so input deck editing is required. The target, projectile mesh, boundary conditions, and initial conditions can be created within Abaqus/CAE, or any other pre-processing tool. The *.inp input file can be created and adjusted per these instructions before the simulation is submitted.

The section of the input file containing the ice material model inputs is provided in Table A.1. This block should replace the entire material definition section related to the ice material. The material input keywords for the ice material and the values specified in metric units. Line numbers are provided in the first column for further explanation and reference, but only the second column of the table should be added to the input file. The keywords used in the material model are:

- *MATERIAL: Line one begins the material definition with the *MATERIAL keyword. Lines two and three contain the *ELASTIC keyword with the Young's Modulus and Poisson's ratio.
- *DENSITY: Lines four and five contain the *DENSITY keyword definition and the density input, respectively.
- *PLASTIC: Lines six through eight define the *PLASTIC with the yield value at zero plastic strain in the second line and the yield value at a plastic strain of 1 m/m in the third line.
- *TENSILE FAILURE: Lines nine and ten contain the *TENSILE FAILURE keyword and the specified inputs. In this model the shear failure option is set to brittle while the tensile option is set to ductile. By not including the element deletion option, the default is set to "NO", or no elements are deleted during simulation. The second line contains the input value for the cutoff stress.
- *RATE DEPENDENT: Lines 11 through 27 contain the *RATE DEPENDENT keyword inputs for adding the strain rate dependent plastic yield stress. Tabulated inputs for the different curves are listed in Tables A.2 through A.4. Each line contains the ratio of the strength, first number, at the corresponding strain rate, second number after

comma separator. It should be noted the first two rows are identical for all three tables. The first row defines the stress ratio at zero strain rate. The second row is used to add one additional point next to the origin as study to assist in the curve fitting internal to the Abaqus solver. Studies using a single element yielding at various strain rates showed this second row to be necessary.

Table A.1: Ice material input for an Abaqus input file (*.inp) in metric units

Line #	Contents for Input File
1	`*Material, name=Ice`
2	`*Elastic`
3	` 9.38E9, 0.33`
4	`*Density`
5	` 900,`
6	`*Plastic`
7	`5.2E6,0.`
8	`5.2E6,1`
9	`*TENSILE FAILURE, SHEAR=BRITTLE,PRESS=DUCTILE`
10	`5.17E+05`
11	`*Rate Dependent, type=YIELD RATIO`
12	`1, 0`
13	`1.01, 0.1`
14	`1.495577759, 0.5`
15	`1.709011483, 1`
16	`2.204589242, 5`
17	`2.418022966, 10`
18	`2.913600725, 50`
19	`3.127034449, 100`
20	`3.622612208, 500`
21	`3.836045932, 1000`
22	`4.331623691, 5000`
23	`4.545057415, 10000`
24	`5.040635174, 50000`
25	`5.254068897, 100000`
26	`5.749646657, 500000`
27	`5.96308038, 1000000`

Table A.2: C1 – Avg. Yield Strength Ratio Input

Stress Ratio	Strain Rate (s^{-1})
1	0
1.01	0.1
1.495577759	0.5
1.709011483	1
2.204589242	5
2.418022966	10
2.913600725	50
3.127034449	100
3.622612208	500
3.836045932	1000
4.331623691	5000
4.545057415	10000
5.040635174	50000
5.254068897	100000
5.749646657	500000
5.96308038	1000000

Table A.3: C2 - Lower Yield Strength Ratio Input

Stress Ratio	Strain Rate (s^{-1})
1	0
1.01	0.1
1.267017189	0.5
1.382015232	1
1.649032421	5
1.764030465	10
2.031047654	50
2.146045697	100
2.413062886	500
2.52806093	1000
2.795078118	5000
2.910076162	10000
3.177093351	50000
3.292091395	100000
3.559108583	500000
3.674106627	1000000

Table A.4: C3 - Upper Yield Strength Ratio Input

Stress Ratio	Strain Rate (s^{-1})
1	0
1.01	0.1
1.719300708	0.5
2.029086661	1
2.748387369	5
3.058173322	10
3.777474029	50
4.087259982	100
4.80656069	500
5.116346643	1000
5.835647351	5000
6.145433304	10000
6.864734012	50000
7.174519965	100000
7.893820672	500000
8.203606625	1000000

A.2. Contact and Bulk Viscosity

The other important model details are the contact (interaction) settings and bulk viscosity. For contact, “hard” and “frictionless” contact was defined between the outer surface of the sphere and the target surface. The syntax used in the input file is listed in Table A.5. The interaction and behavior can also be created in Abaqus/CAE. Note, a separate definition (*CONTACT) defining contact between the two surfaces is not shown, but is required and is included in the STEP section.

Table A.5: Contact properties addition to input file

Line #	Contents for Input File
1	`*Surface Interaction, name=ContactProperty`
2	`*Friction`
3	`0.,`
4	`*Surface Behavior, pressure-overclosure=HARD`

The contents of Table A.6 show the addition of the *BULK VISCOSITY keyword, using a linear bulk viscosity of 1.2 and quadratic bulk viscosity of zero (with default being zero when unspecified with custom linear bulk viscosity). It is essential to use this line in the simulation. The *STEP and *DYNAMIC input value defining the simulation length is up to the user discretion, but are shown for reference. In this case, a simulation time of 150 μs is specified. These settings can also be defined and changed within Abaqus/CAE.

Table A.6: Bulk viscosity addition to input file

Line #	Contents for Input File
1	`*Step, name=Shoot`
2	`*Dynamic, Explicit`
3	`, 0.00015`
4	`*Bulk Viscosity`
5	`1.2,`

Appendix B. Projectile Mesh Creation

The following is the procedure for creating the biased mesh for the quarter spherical model shown in Figure B.1. Step by step instructions for making the projectile mesh are listed below in the captions of Figures B.2 through B.16. Abaqus/CAE was used in this procedure, but any pre-processor with similar commands can be used.

The key features for creating the biased spherical mesh are the interior box partition, the projected partitions off the face of the box to the surface of the sphere, and the biased seed option on the interior box in the direction away from the impact face. A sketch shown in Figure B.1 has dimensions the key datum point locations with a normalized unit diameter (any X, Y, or Z orientation can be used). With a normalized diameter, the target normalized minimum element size is 0.0075.

Table B.1: Coordinates of Partition Datum Points for Biased Mesh

Point*	X**	Y**	Z**
1	0	0	-0.125
2	0	0	-0.65
3	-0.2	0	-0.125
4	-0.2	0	-0.65
5	0	0.2	-0.125
6	0	0.2	-0.65
7	0.2	0.2	-0.125
8	0.2	0.2	-0.65

*Origin is at front impact point
**Coordinate specified as ratio of diameter (e.g. so for D=50.8 mm, X = 0.0254 m)

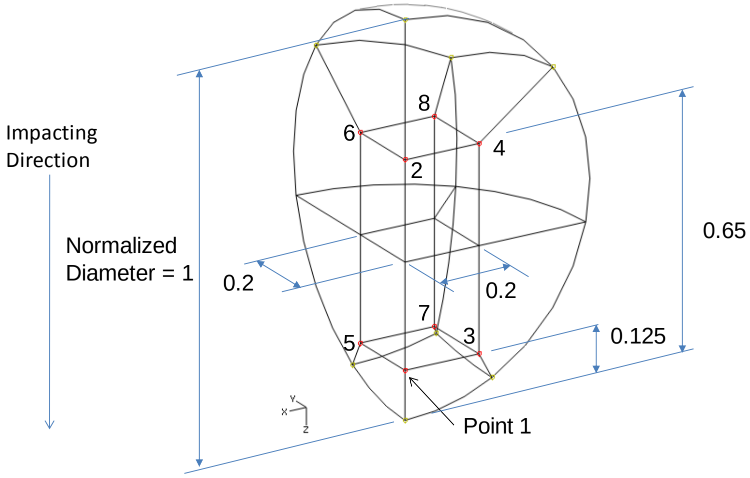

Figure B.1: Sketch of key sphere dimensions with normalized unit diameter; labels of datum points also shown

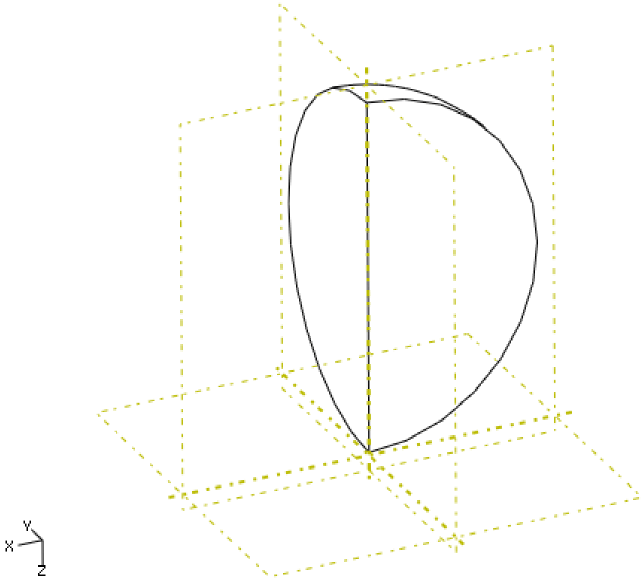

Figure B.2: Step 1: Create quarter revolution of a sphere from a hemispherical sketch

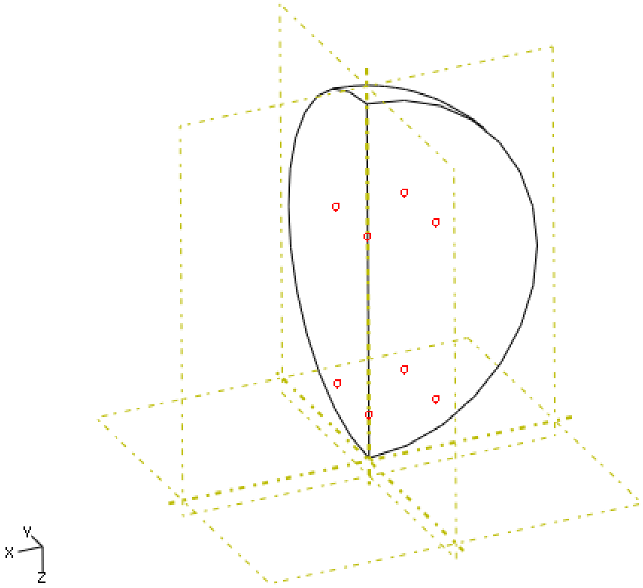

Figure B.3: Step 2: Create 8 datum points with the coordinates as ratios of the diameter of the sphere provided in Table B.1.

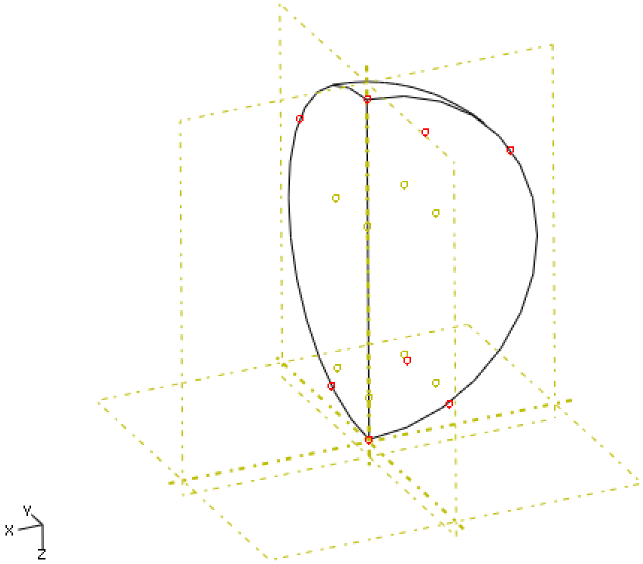

Figure B.4: Step 3: Project each datum point onto exterior surface of sphere

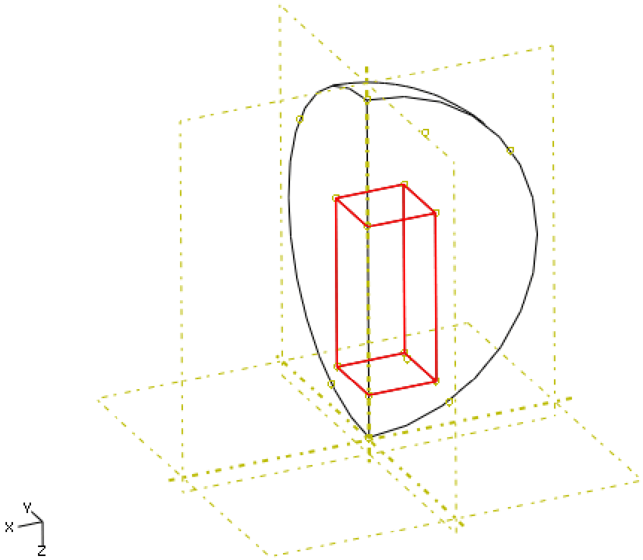

Figure B.5: Step 4: Create wires connecting each datum point in a box as shown.

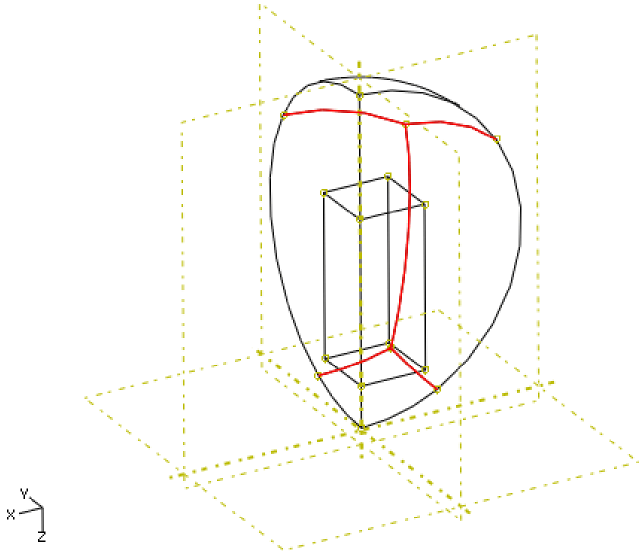

Figure B.6: Step 5: Partition exterior face connecting exterior surface datum points as shown

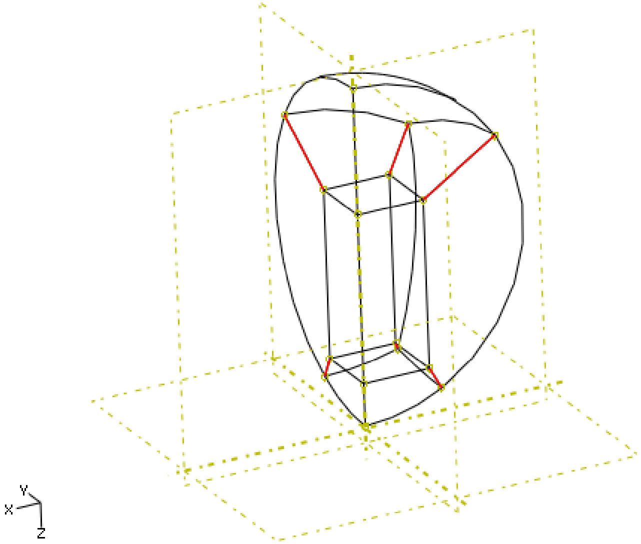

Figure B.7: Step 6: Create wires connecting interior box datum points to corresponding projected surface datum point.

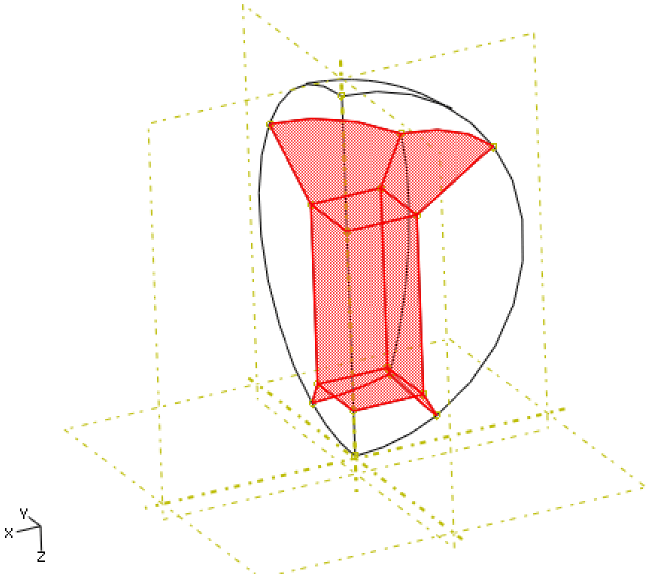

Figure B.8: Step 7: Add interior faces using the wires created previously

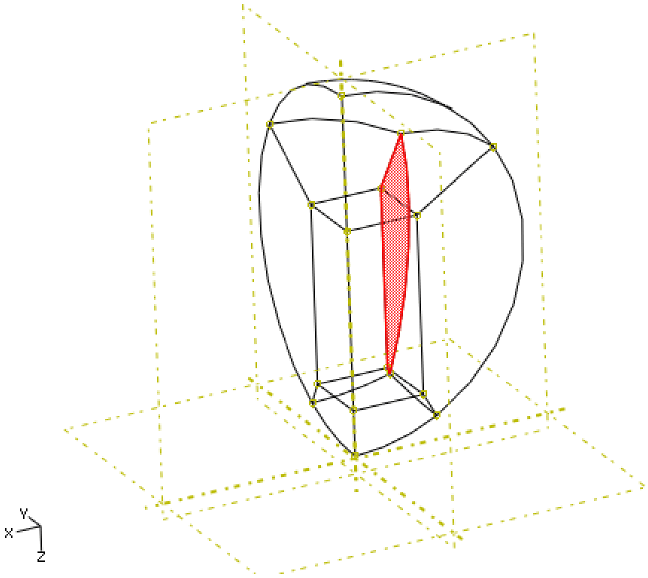

Figure B.9: Step 8: Add partition to the remaining cell with partition command

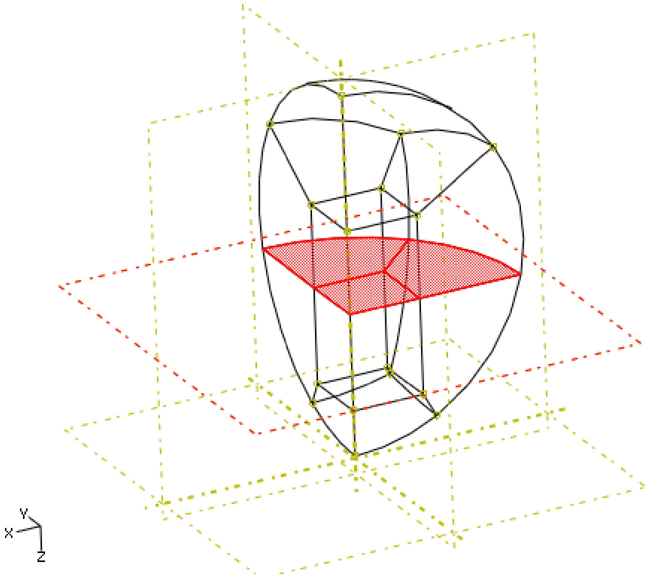

Figure B.10: Step 9: Partition sphere into two using datum plane at equatorial position

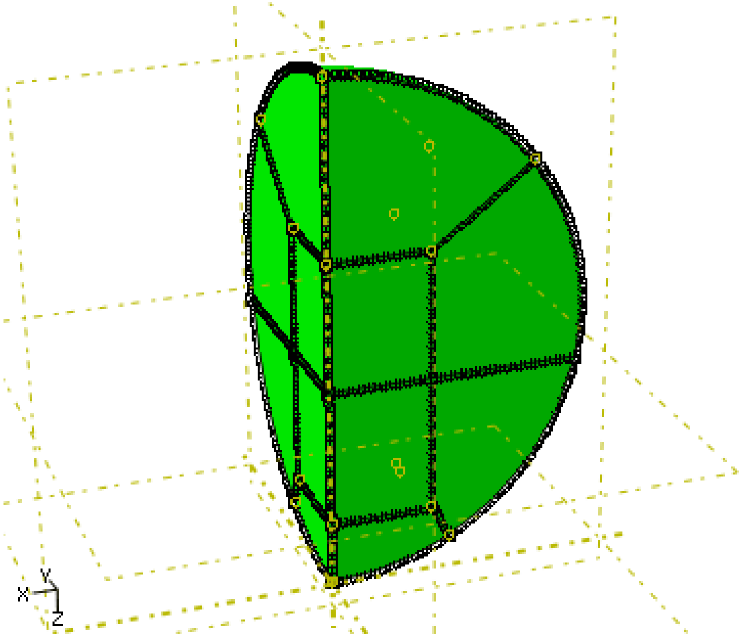

Figure B.11: Step 10: Create seed definitions on a structured mesh (green highlight); use a 0.01 x Diameter base seed size.

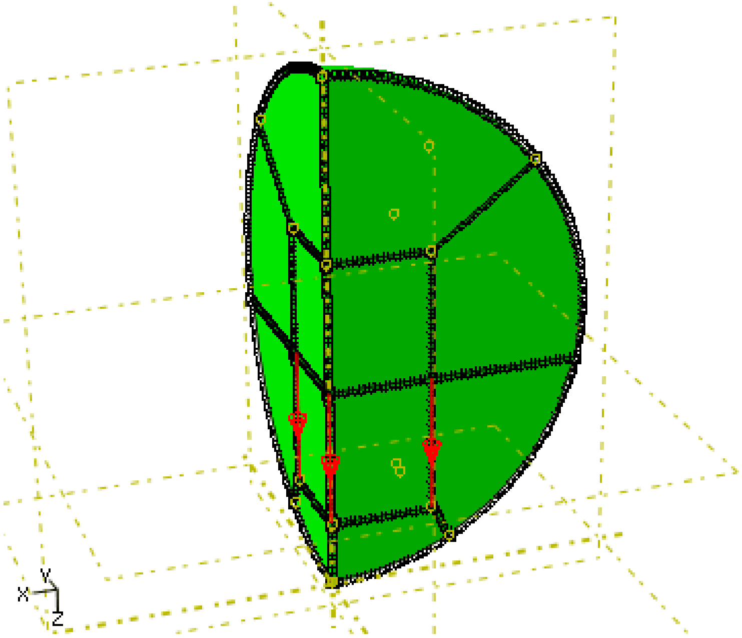

Figure B.12: Step 11: For two edges on lower inner rectangular box, use a bias ratio 3.0 such that elements are smaller near the impact face (bottom) and create 21 elements on edge.

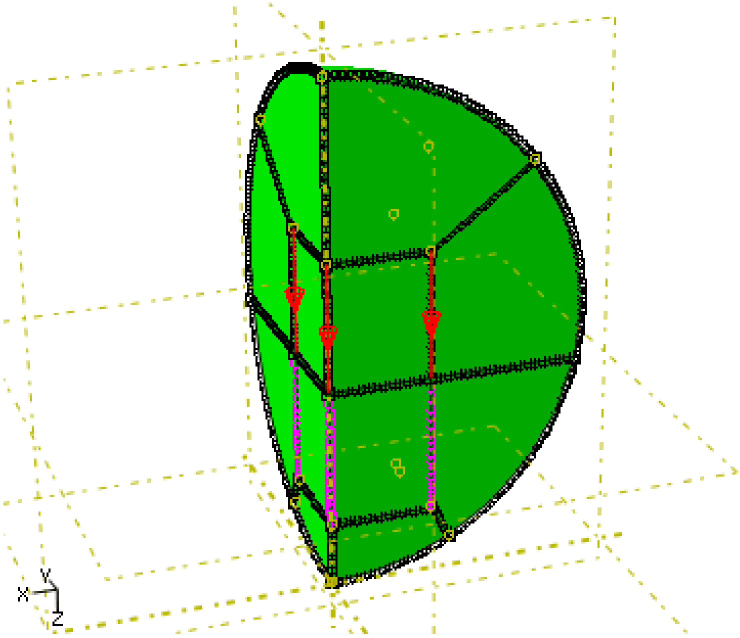

Figure B.13: Step 12: For two edges on upper inner rectangular box, use a bias ratio 1.5 such that elements are smaller near the impact face (bottom) and create 9 elements on edge.

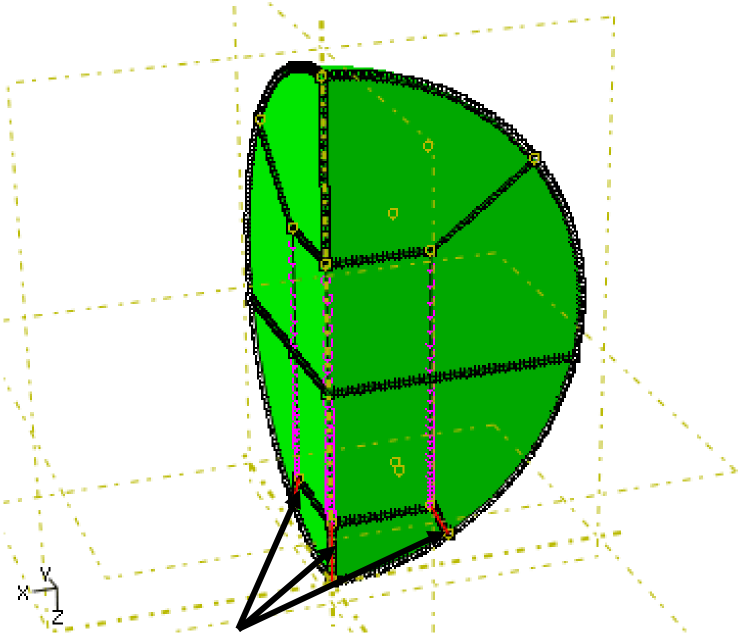

Figure B.14: Step 13: For two small edges leading to exterior surface define 8 evenly spaced elements along edge.

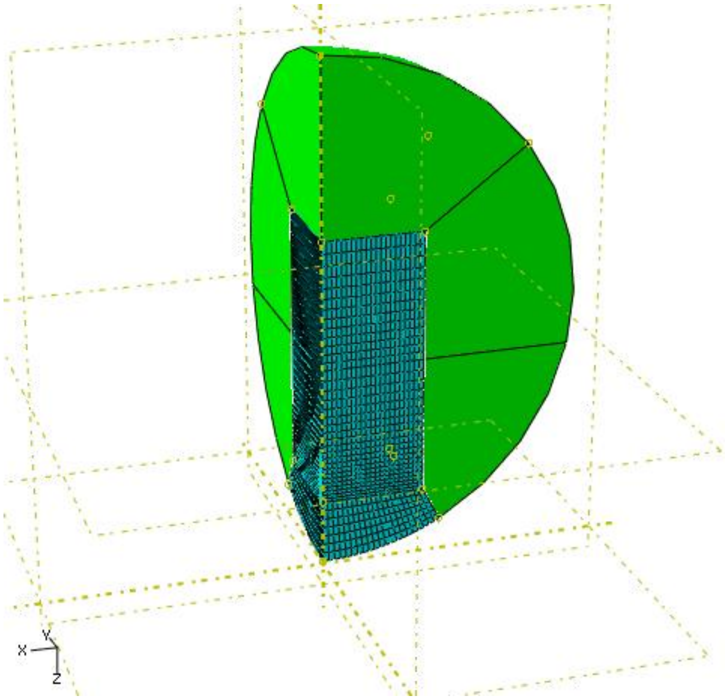

Figure B.15: Step 14: Mesh partitions center partitions as shown.

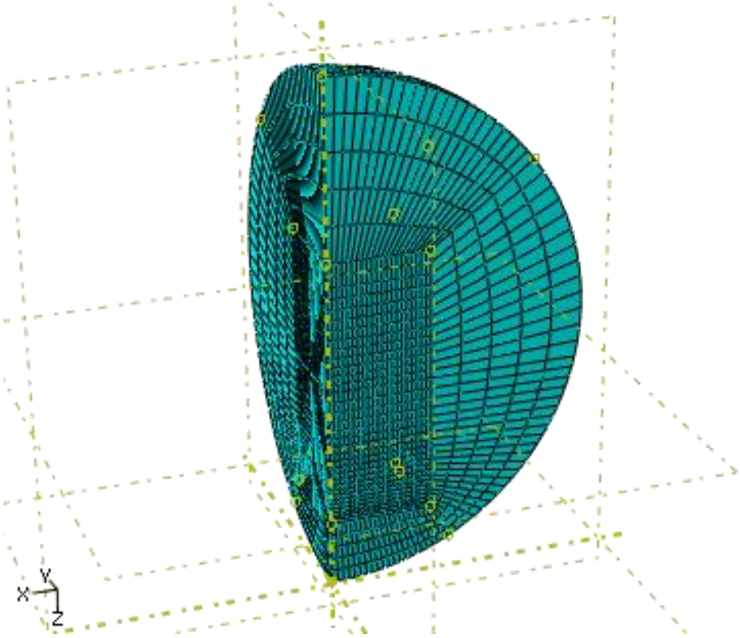

Figure B.16: Step 15: Mesh the remaining partitions

Appendix C. Summary of Experimental Tests

Table C.1: Complete list of Monolithic SHI Impact Tests Conducted Using Force Measurement Bar Apparatus

Test ID	SHI Diam. (mm)	SHI Mass (g)	Velocity (m/s)	Kinetic Energy (J)	Peak Force (kN)	Impulse (N-s) (1 ms window)
Purdue 28	61.0	106.5	45.4	110	16.0	1.09
Purdue 54	61.0	104.9	39.0	80	13.3	1.11
Purdue 70	61.0	103.6	41.4	89	12.7	0.8
Purdue 75	61.0	106	49.2	128	14.7	0.49
Purdue 82	61.0	109.7	37.7	78	12.1	0.35
Purdue 83	61.0	110.2	37.3	77	13.2	1.96
Purdue 84	61.0	110.9	36.2	72	12.0	2.05
Purdue 91	61.0	110.7	46.0	117	23.7	2.37
Purdue 92	61.0	110.9	48.3	129	20.1	2.55
Purdue 93	61.0	110.2	50.4	140	20.2	2.72
Purdue 111	61.0	108	23.5	30	7.4	0.97
Purdue 112	61.0	106.7	22.1	26	6.3	0.82
Purdue 113	61.0	110.3	19.3	21	5.2	0.62
Purdue 124	61.0	108	189.2	1933	99.2	8.24
Purdue 125	61.0	110.8	193.7	2079	112.4	16.28
Purdue 136	61.0	109.9	95.4	500	28.3	4.54
UCSD 1	38.1	23.4	69.2	56	8.4	1.38
UCSD 2	38.1	24.3	117.0	166	22.3	2.55
UCSD 3	38.1	24.6	142.0	248	34.5	3.03
UCSD 4	38.1	24.4	158.0	305	38.2	3.33
UCSD 5	38.1	25	141.8	251	30.5	3.08
UCSD 6	38.1	24	135.7	221	35.3	2.53
UCSD 7	38.1	24.3	126.9	196	20.2	2.7
UCSD 8	38.1	25.4	106.4	144	19.9	2.25
UCSD 9	50.8	60.3	111.2	373	44.8	4.58
UCSD 10	50.8	62	132.2	541	54.1	5.68
UCSD 11	50.8	61.6	144.3	641	64.3	6.85
UCSD 12	50.8	62.5	99.9	312	40.7	3.47
UCSD 28	38.1	23.2	108.6	137	15.0	2.38
UCSD 29	50.8	58.9	109.9	356	36.6	4.95
UCSD 30	61.0	107.5	105.0	593	61.9	5.21

Table C.1 Continued: Complete list of Monolithic SHI Impact Tests Conducted Using Force Measurement Bar Apparatus

UCSD 31	38.1	23.9	135.8	220	27.1	3.27
UCSD 32	50.8	58.3	149.6	652	55.6	6.47
UCSD 33	61.0	107	144.2	1112	82.1	7.38
UCSD 34	38.1	21.7	135.3	199	30.0	2.77
UCSD 35	50.8	57	133.4	507	44.5	3.17
UCSD 36	61.0	106.7	124.9	833	76.5	7.9
UCSD 37	38.1	23.6	75.1	67	13.5	1.56
UCSD 38	50.8	58	73.9	158	22.9	2.44
UCSD 39	61.0	106.5	72.6	281	29.9	3.23
UCSD 184	61.0	110.1	81.2	363	30.0	7.2
UCSD 186	50.8	57.1	63.6	116	10.9	2.01
UCSD 187	50.8	54.8	63.9	112	9.5	1.84
UCSD 188	61.0	105.5	98.9	516	26.7	5.27
UCSD 190	61.0	108.9	80.4	352	22.8	4.59
UCSD 191	61.0	105.2	61.8	201	13.9	3.63
UCSD 195	50.8	62	60.6	114	14.5	2.18
UCSD 197	50.8	61.8	82.2	209	20.3	4.03
UCSD 201	50.8	63.2	59.3	111	14.5	2.95
UCSD 202	50.8	63.1	62.6	124	16.7	3.4
UCSD 203	50.8	63.1	61.2	118	15.0	3.12
UCSD 204	50.8	63.6	61.2	119	15.1	3.03
UCSD 207	38.1	26.6	133.7	238	29.0	3.36
UCSD 208	38.1	25.7	136.1	238	28.3	3.45
UCSD 209	38.1	26.1	134.6	236	27.8	2.37
UCSD 210	38.1	26.8	135.4	246	28.7	4.14

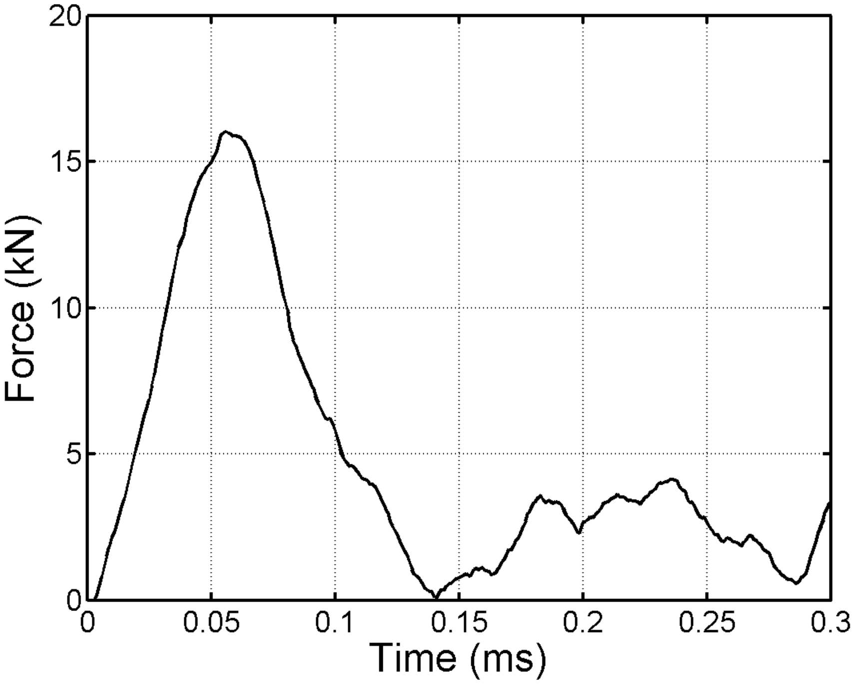

Figure C.1: Purdue Test 28; 61.0 mm diameter SHI at 45.4 m/s (110 J)

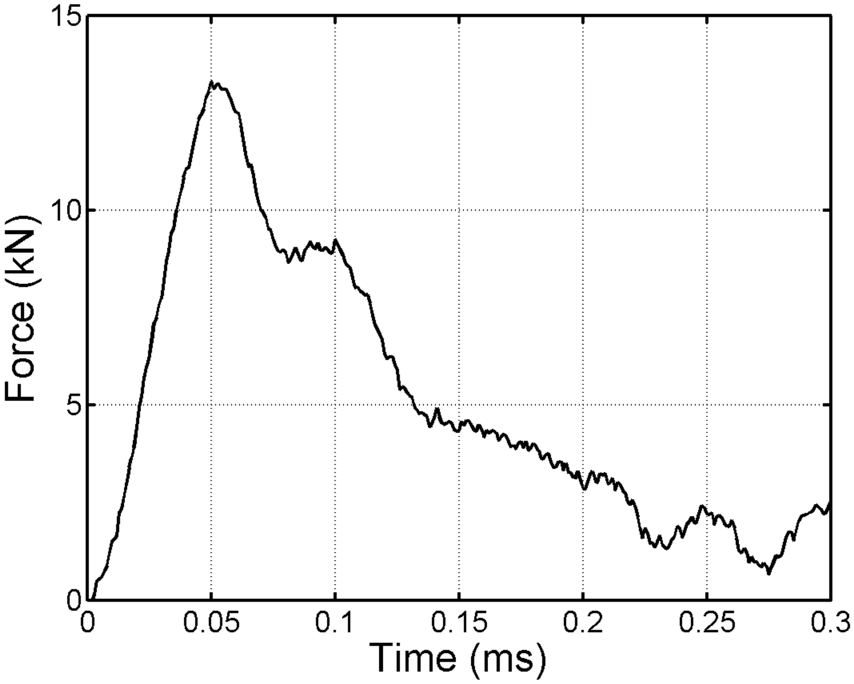

Figure C.2: Purdue Test 54; 61.0 mm diameter SHI at 39.0 m/s (80 J)

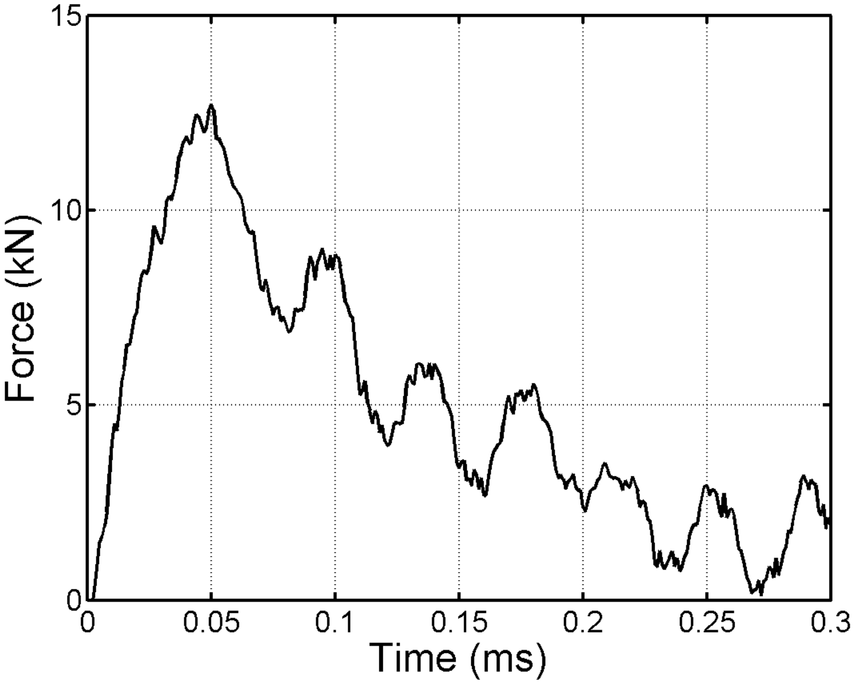

Figure C.3: Purdue Test 70; 61.0 mm diameter SHI at 41.4 m/s (89 J)

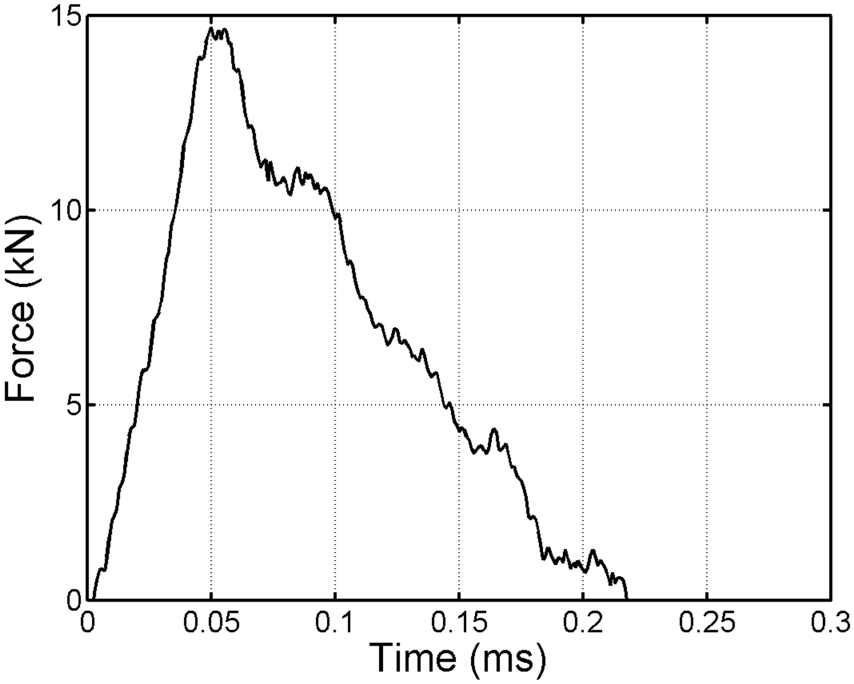

Figure C.4: Purdue Test 75; 61.0 mm diameter SHI at 49.2 m/s (128 J)

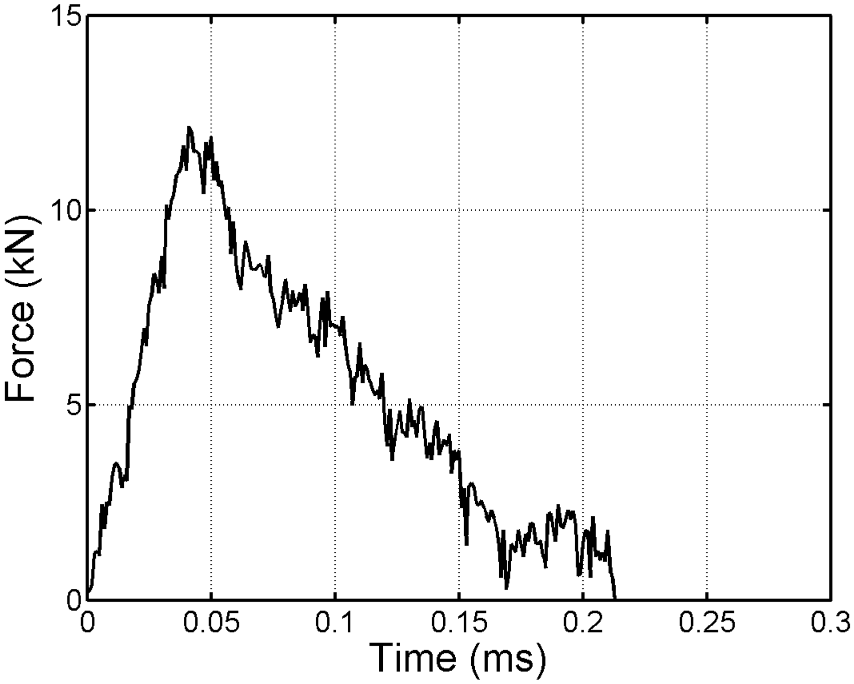

Figure C.5: Purdue Test 82; 61.0 mm diameter SHI at 37.7 m/s (78 J)

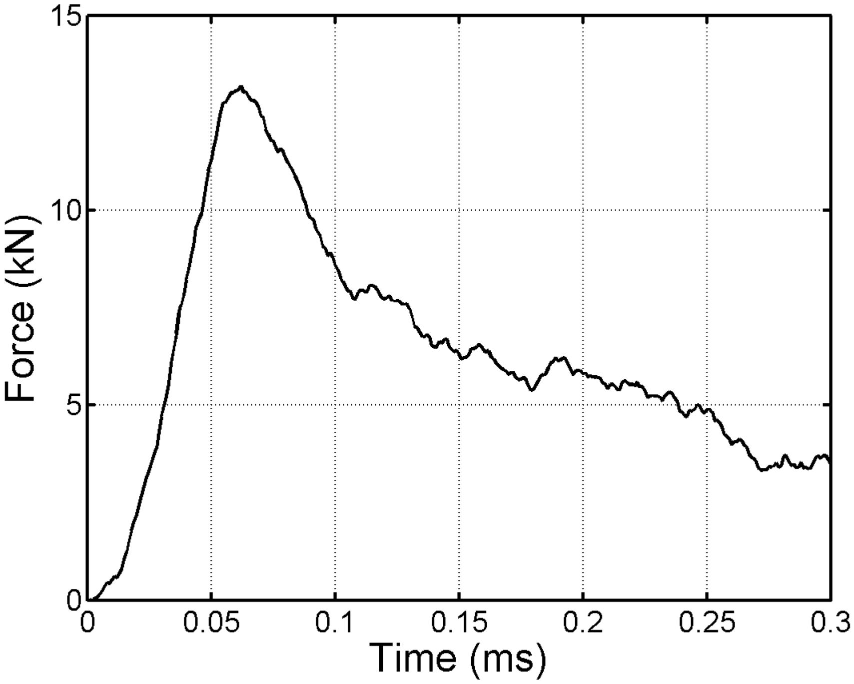

Figure C.6: Purdue Test 83; 61.0 mm diameter SHI at 37.3 m/s (77 J)

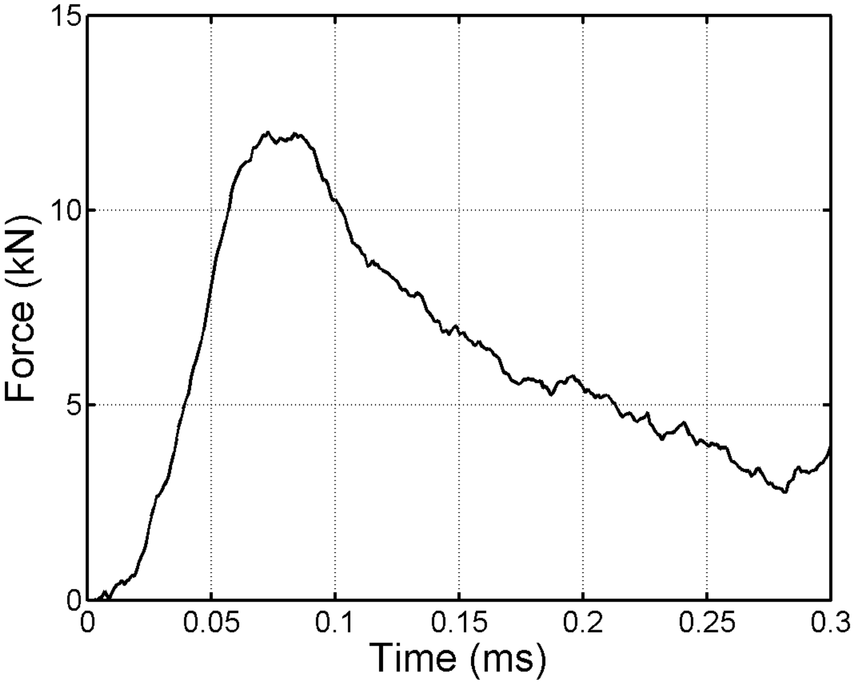

Figure C.7: Purdue Test 84; 61.0 mm diameter SHI at 36.2 m/s (72 J)

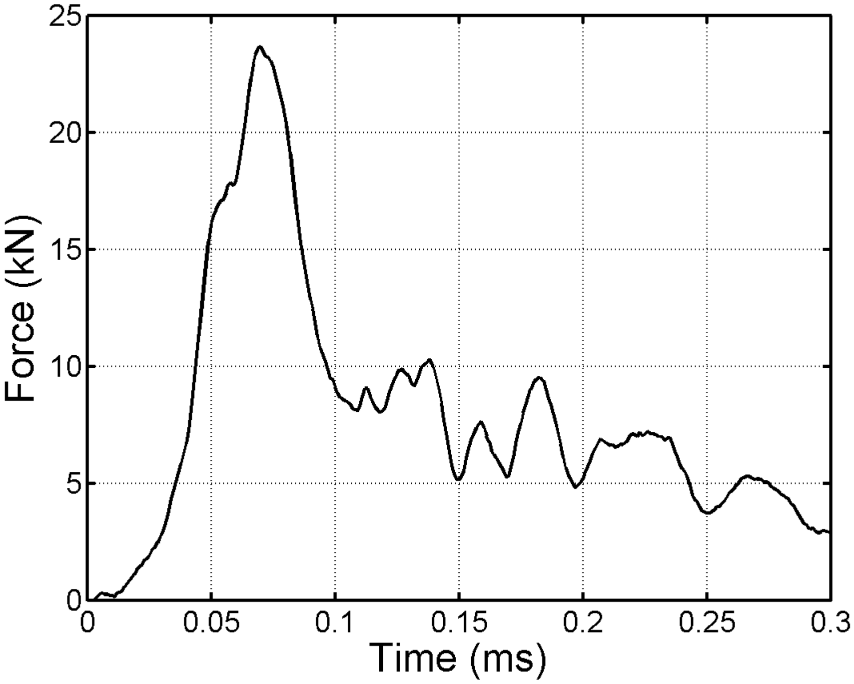

Figure C.8: Purdue Test 91; 61.0 mm diameter SHI at 46.0 m/s (117 J)

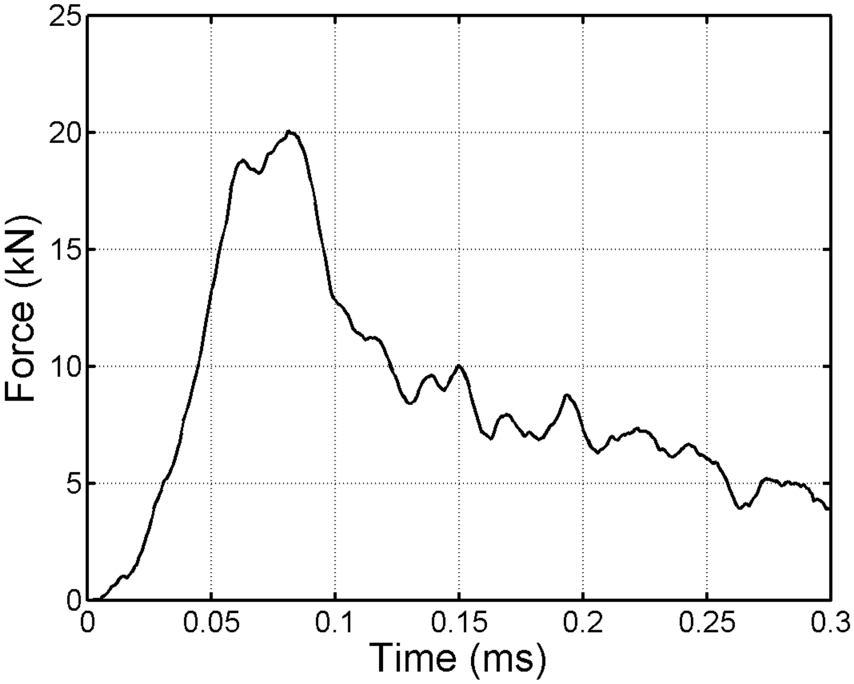

Figure C.9: Purdue Test 92; 61.0 mm diameter SHI at 48.3 m/s (129 J)

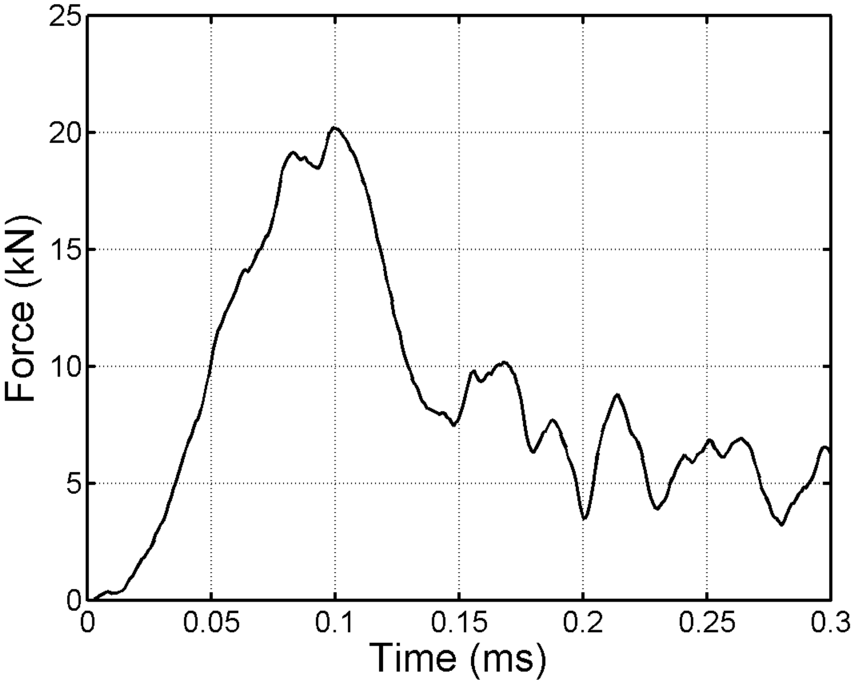

Figure C.10: Purdue Test 93; 61.0 mm diameter SHI at 50.4 m/s (140 J)

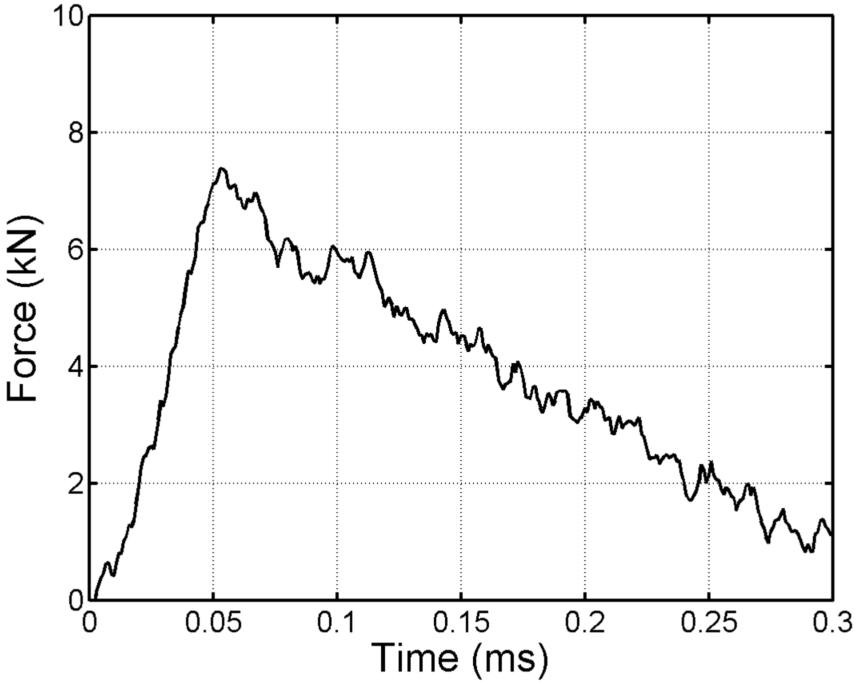

Figure C.11: Purdue Test 111; 61.0 mm diameter SHI at 23.5 m/s (30 J)

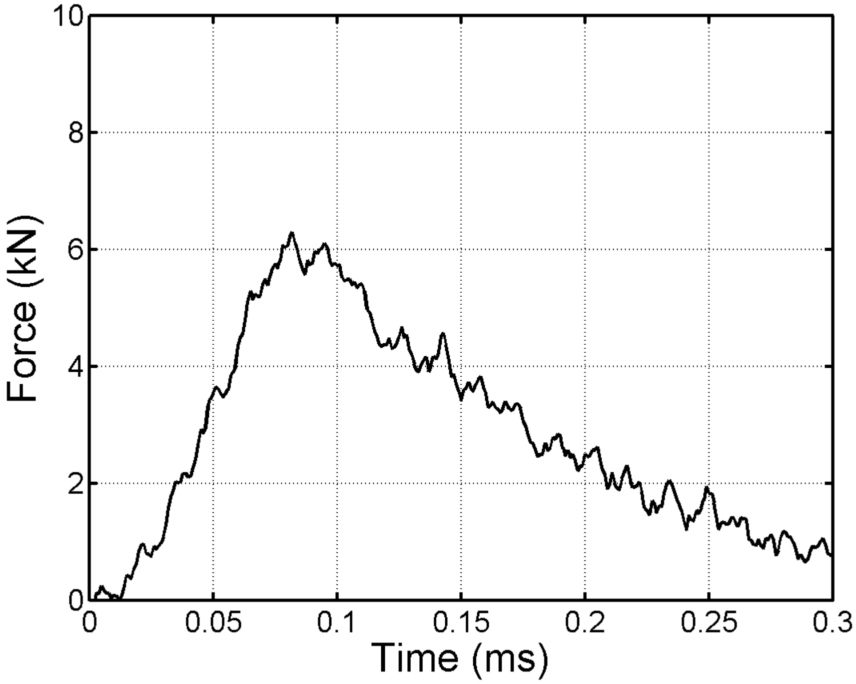

Figure C.12: Purdue Test 112; 61.0 mm diameter SHI at 22.1 m/s (26 J)

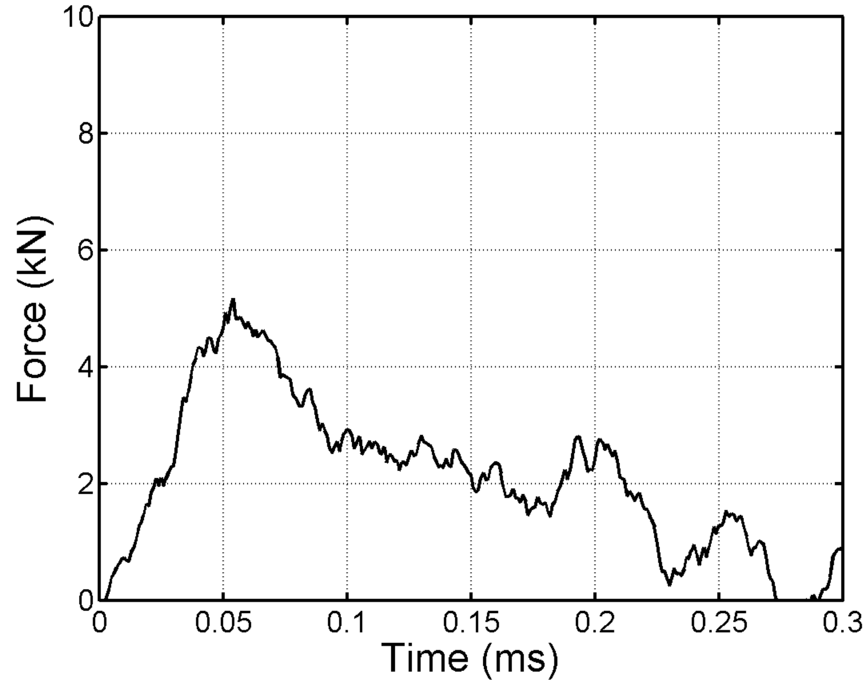

Figure C.13: Purdue Test 113; 61.0 mm diameter SHI at 19.3 m/s (21 J)

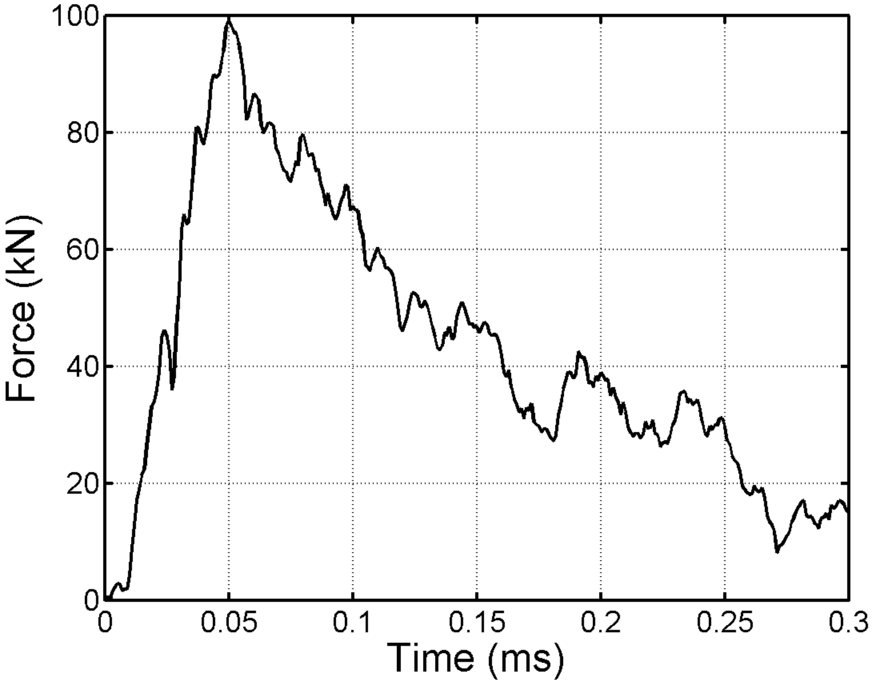

Figure C.14: Purdue Test 124; 61.0 mm diameter SHI at 189.2 m/s (1933 J)

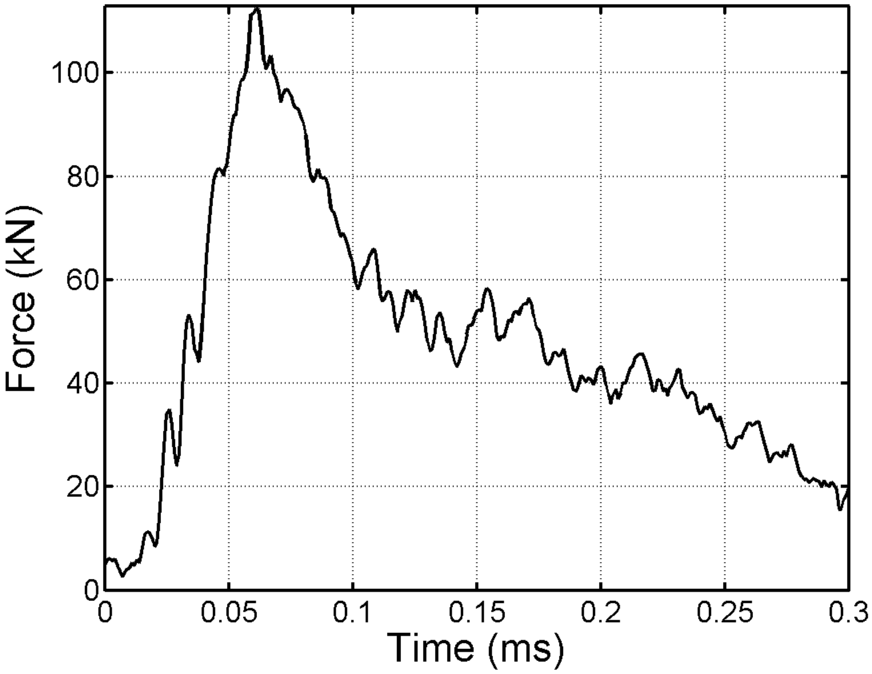

Figure C.15: Purdue Test 125; 61.0 mm diameter SHI at 193.7 m/s (2079 J)

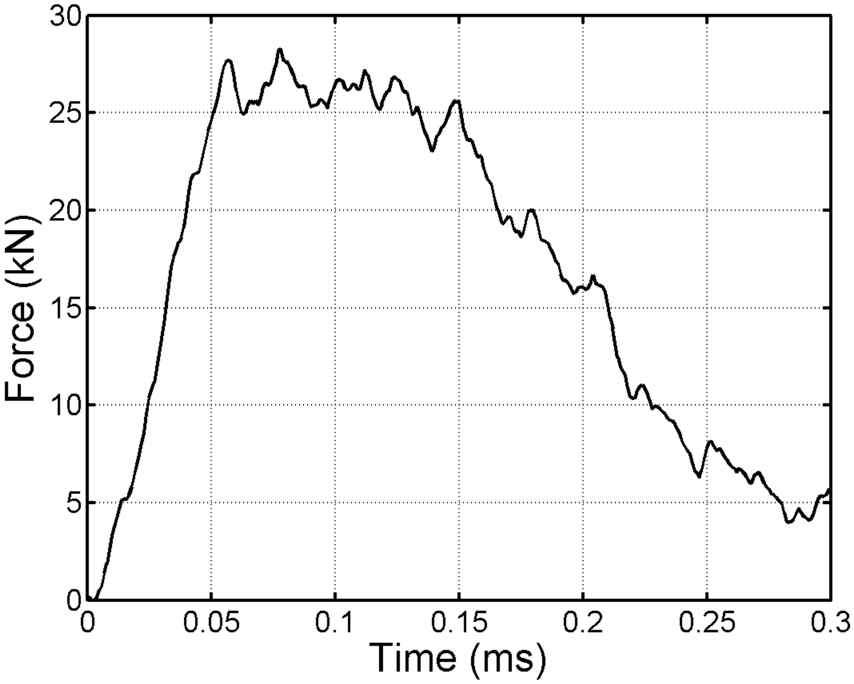

Figure C.16: Purdue Test 136; 61.0 mm diameter SHI at 95.4 m/s (500 J)

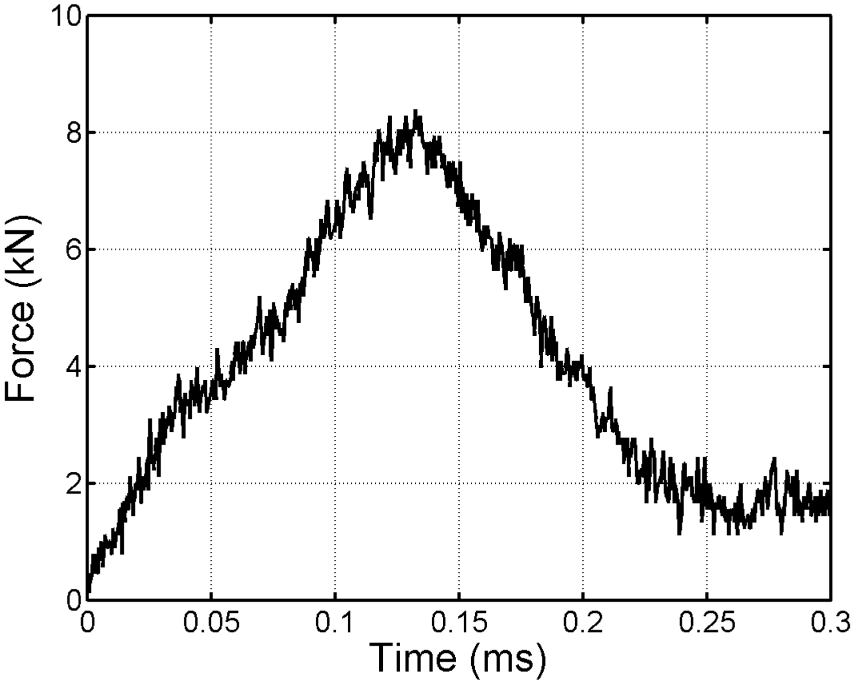

Figure C.17: UCSD Test 1; 38.1 mm diameter SHI at 69.2 m/s (56 J)

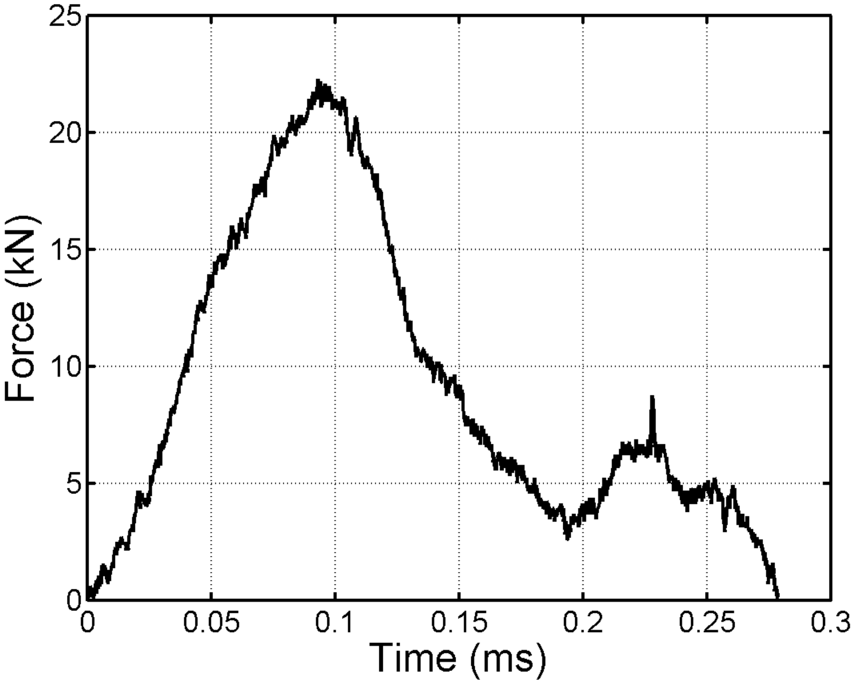

Figure C.18: UCSD Test 2; 38.1 mm diameter SHI at 117.0 m/s (166 J)

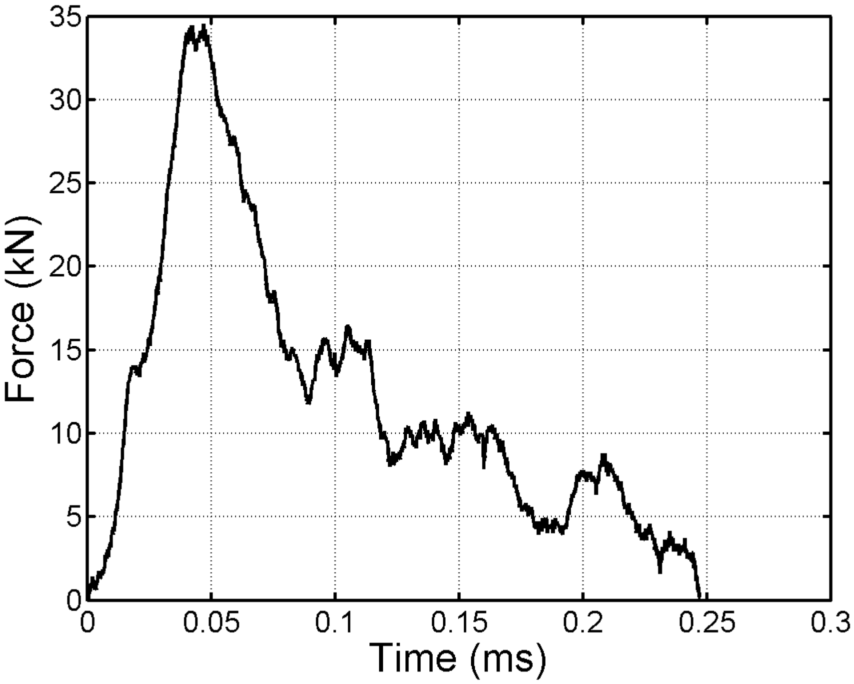

Figure C.19: UCSD Test 3; 38.1 mm diameter SHI at 142.0 m/s (248 J)

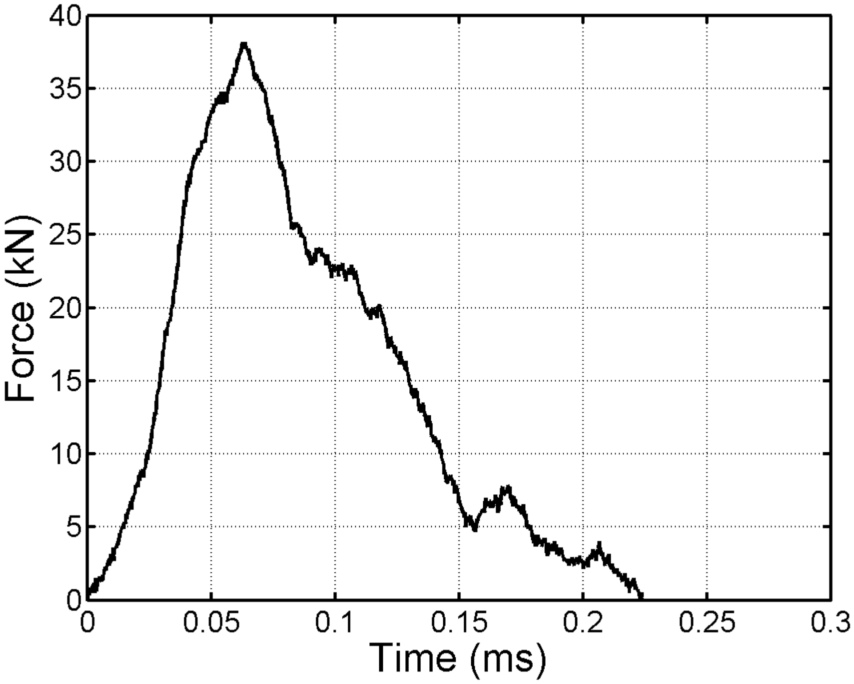

Figure C.20: UCSD Test 4; 38.1 mm diameter SHI at 158.0 m/s (305 J)

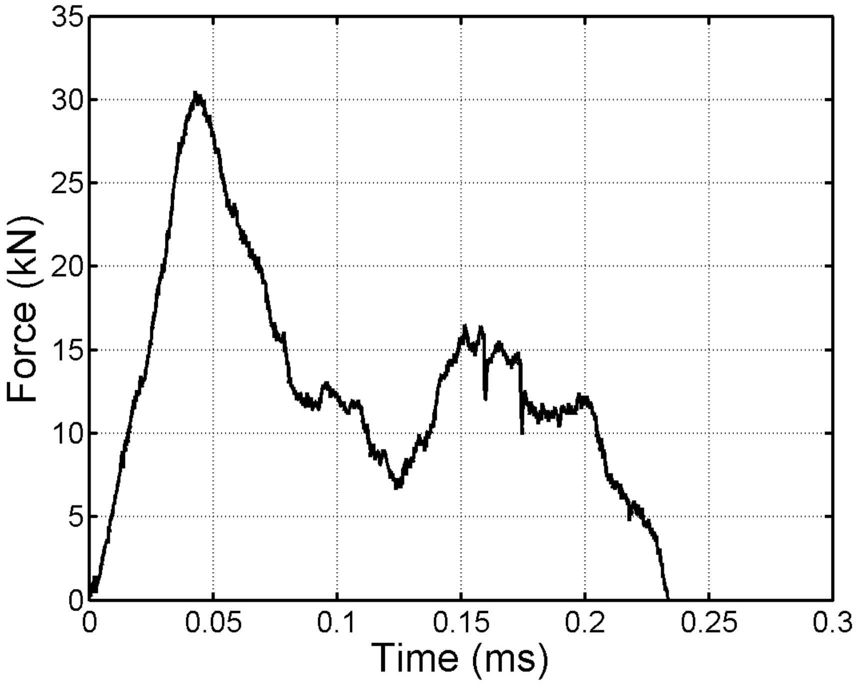

Figure C.21: UCSD Test 5; 38.1 mm diameter SHI at 141.8 m/s (251 J)

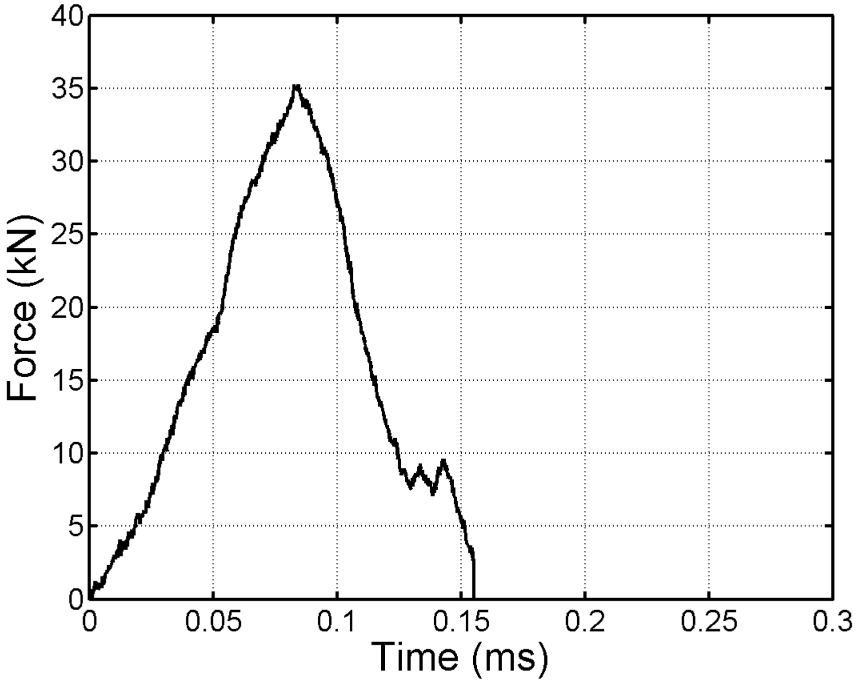

Figure C.22: UCSD Test 6; 38.1 mm diameter SHI at 135.7 m/s (221 J)

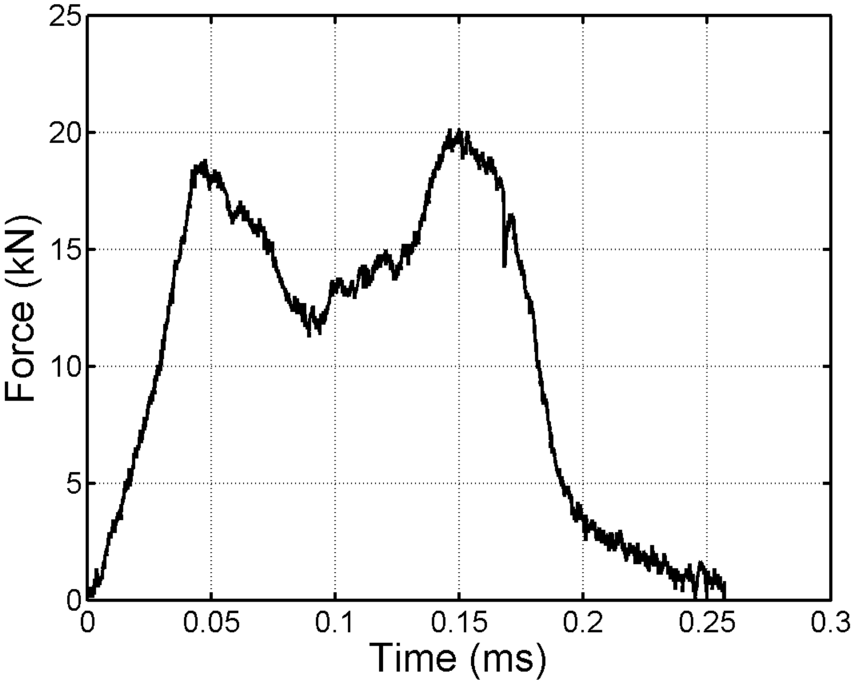

Figure C.23: UCSD Test 7; 38.1 mm diameter SHI at 126.9 m/s (196 J)

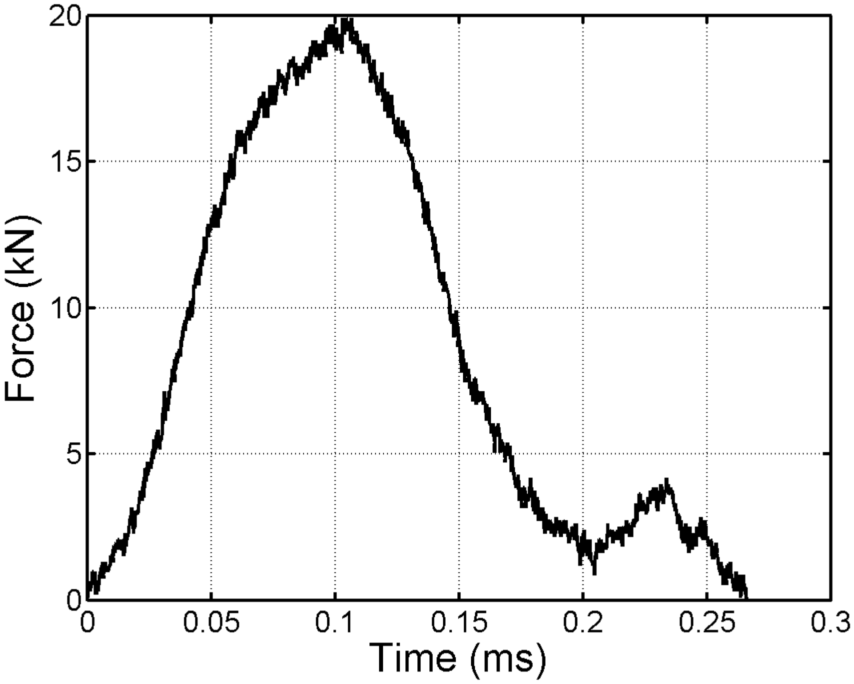

Figure C.24: UCSD Test 8; 38.1 mm diameter SHI at 106.4 m/s (144 J)

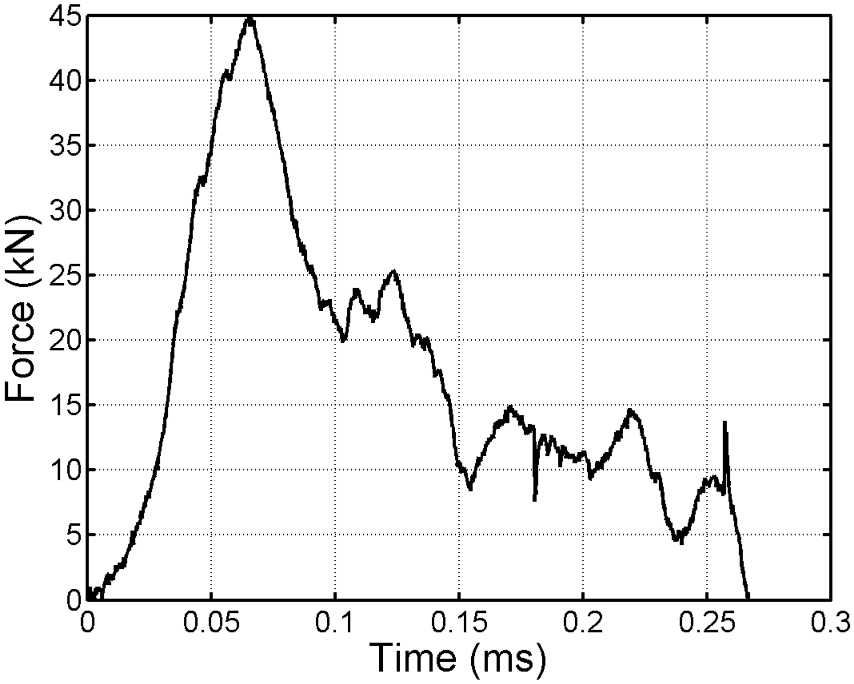

Figure C.25: UCSD Test 9; 50.8 mm diameter SHI at 111.2 m/s (373 J)

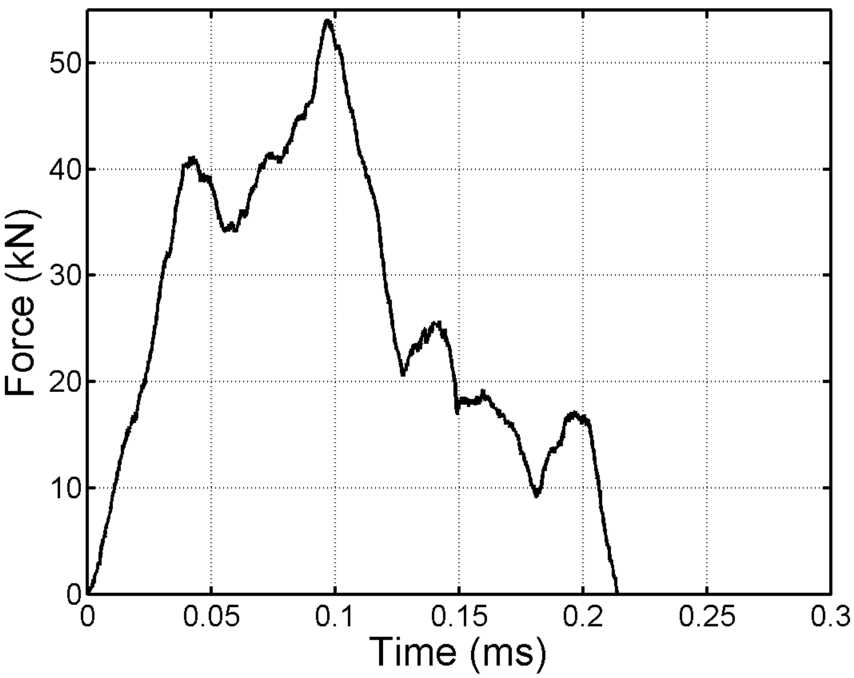

Figure C.26: UCSD Test 10; 50.8 mm diameter SHI at 132.2 m/s (541 J)

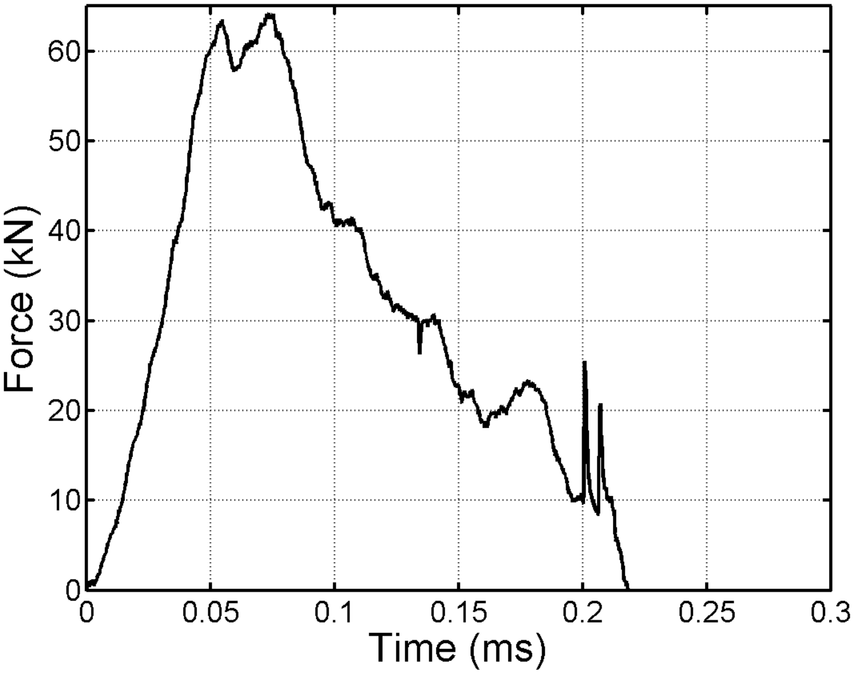

Figure C.27: UCSD Test 11; 50.8 mm diameter SHI at 144.3 m/s (641 J)

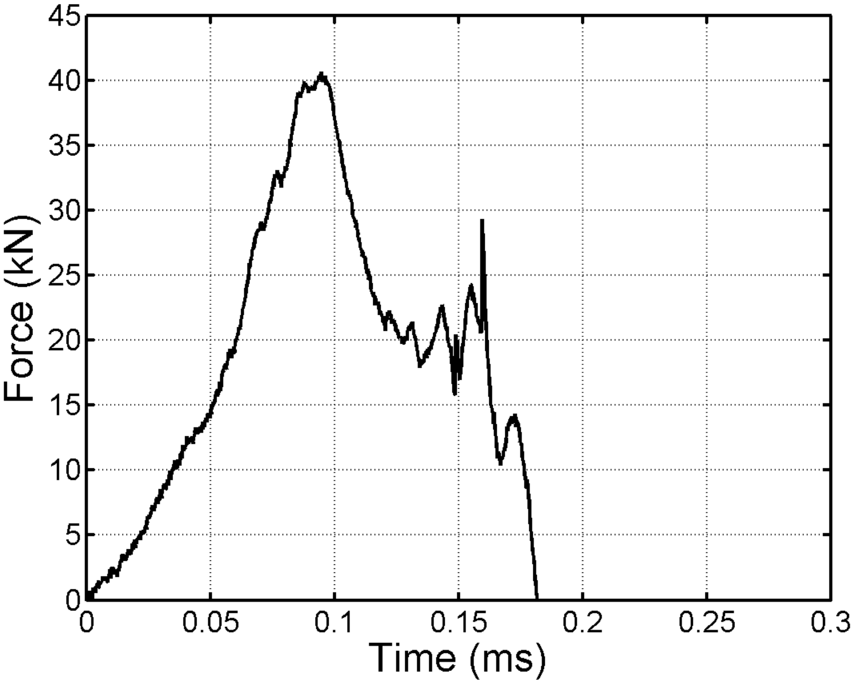

Figure C.28: UCSD Test 12; 50.8 mm diameter SHI at 99.9 m/s (312 J)

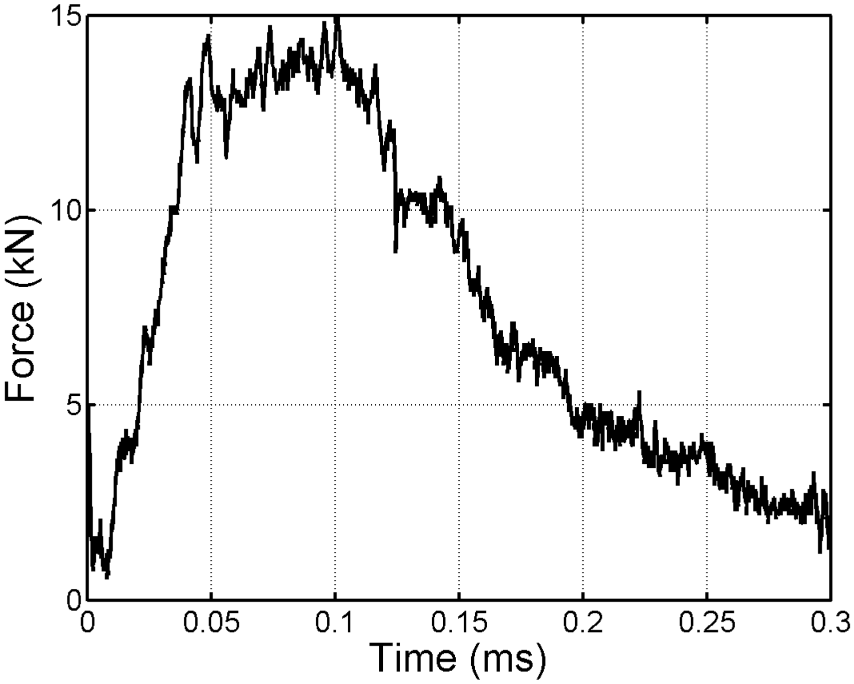

Figure C.29: UCSD Test 28; 38.1 mm diameter SHI at 108.6 m/s (137 J)

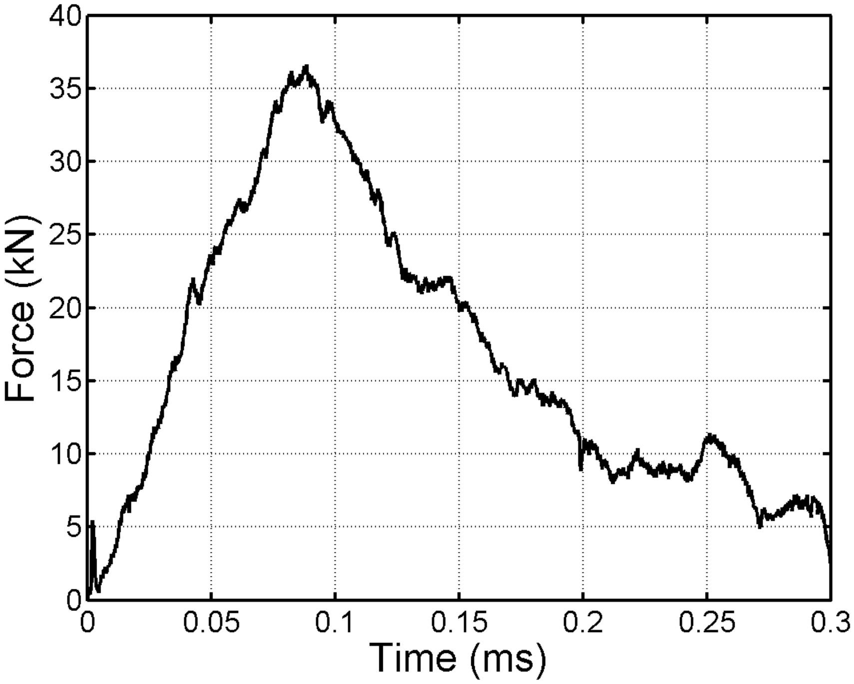

Figure C.30: UCSD Test 29; 50.8 mm diameter SHI at 109.9 m/s (356 J)

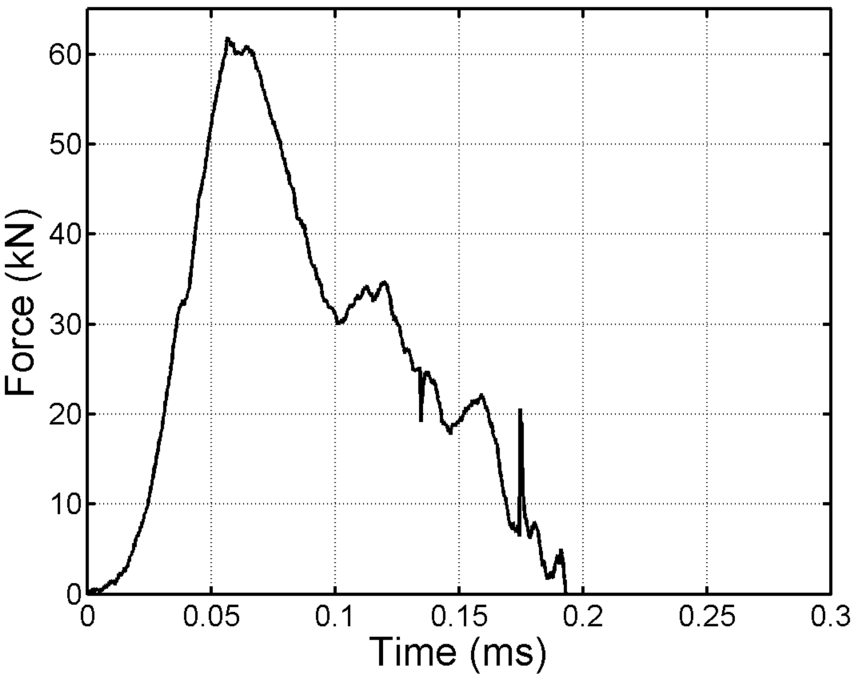

Figure C.31: UCSD Test 30; 61.0 mm diameter SHI at 105.0 m/s (593 J)

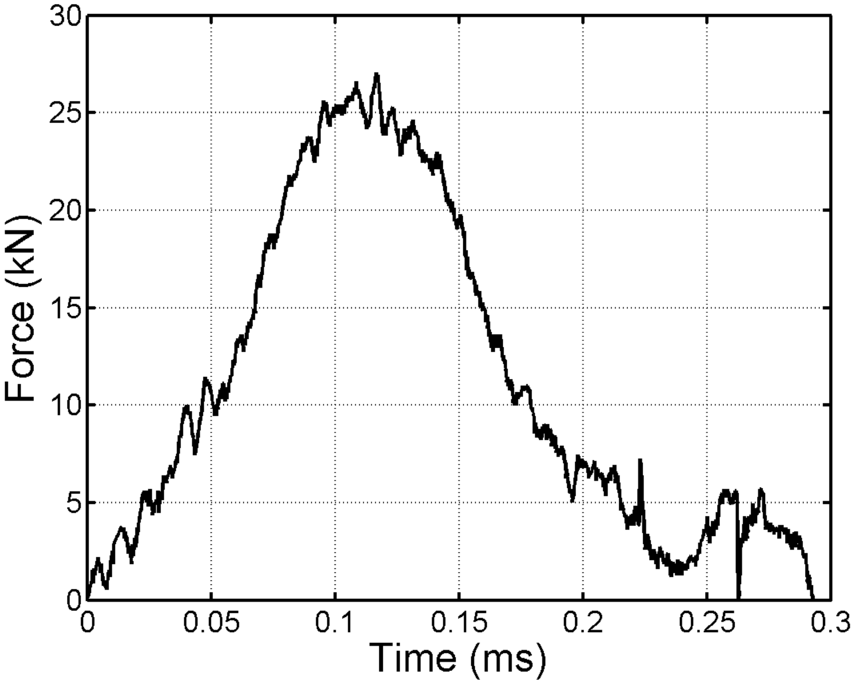

Figure C.32: UCSD Test 31; 38.1 mm diameter SHI at 135.8 m/s (220 J)

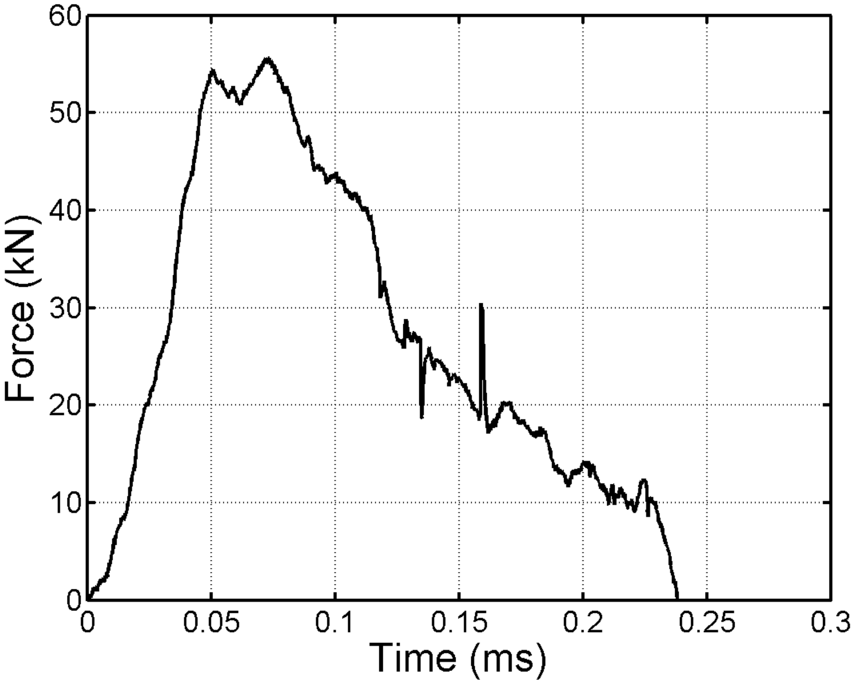

Figure C.33: UCSD Test 32; 50.8 mm diameter SHI at 149.6 m/s (652 J)

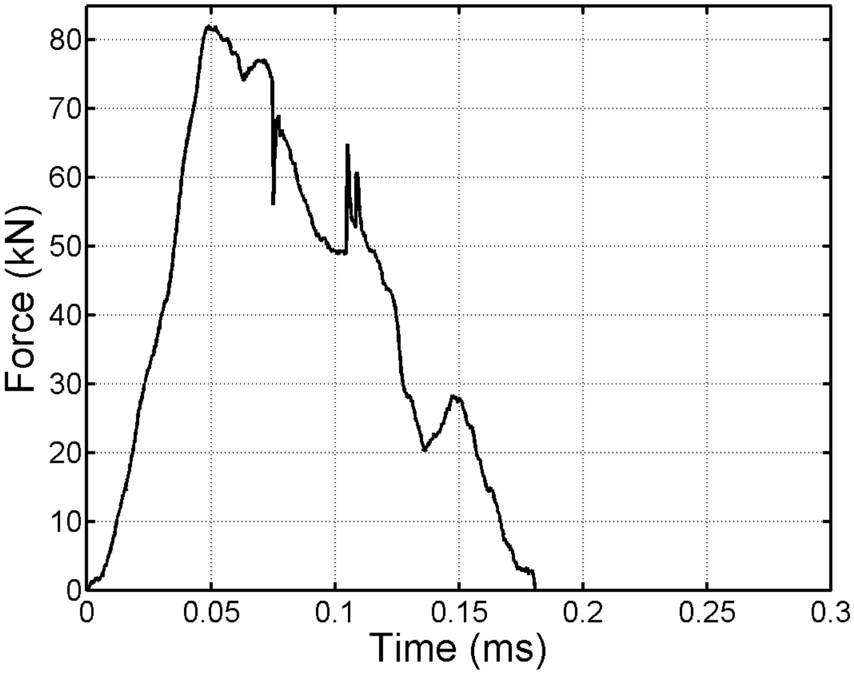

Figure C.34: UCSD Test 33; 61.0 mm diameter SHI at 144.2 m/s (1112 J)

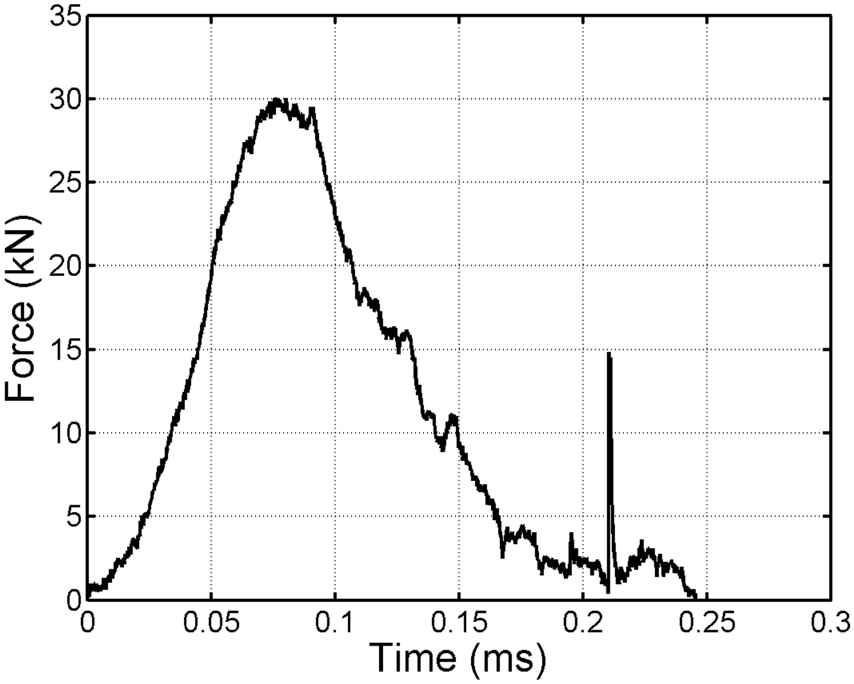

Figure C.35: UCSD Test 34; 38.1 mm diameter SHI at 135.3 m/s (199 J)

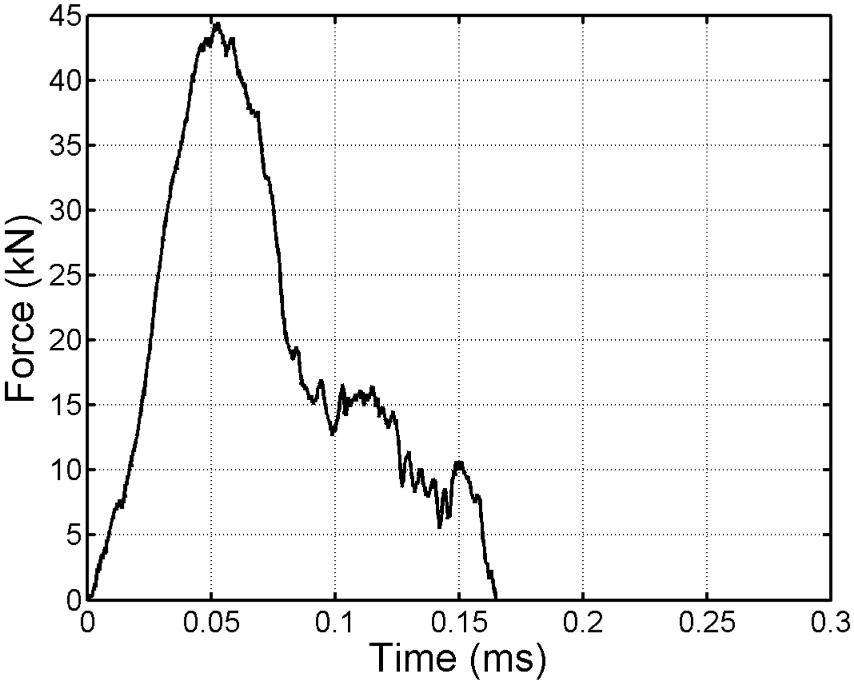

Figure C.36: UCSD Test 35; 50.8 mm diameter SHI at 133.4 m/s (507 J)

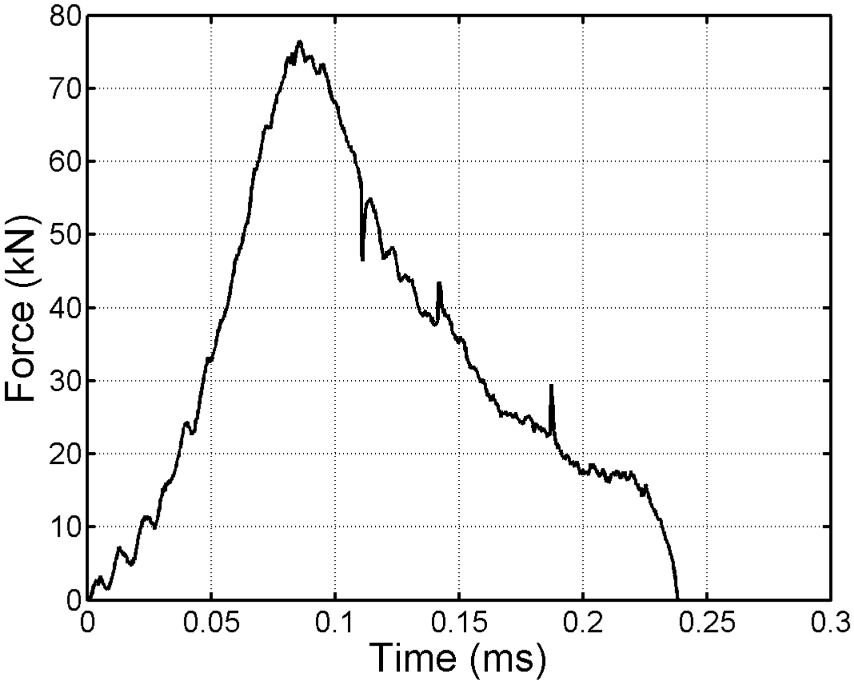

Figure C.37: UCSD Test 36; 61.0 mm diameter SHI at 124.9 m/s (833 J)

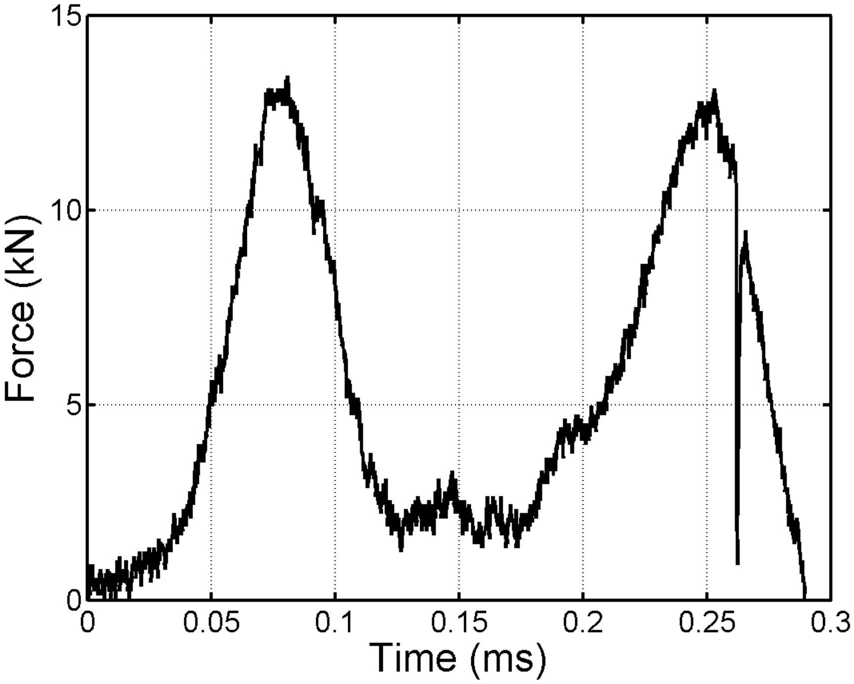

Figure C.38: UCSD Test 37; 38.1 mm diameter SHI at 75.1 m/s (67 J)

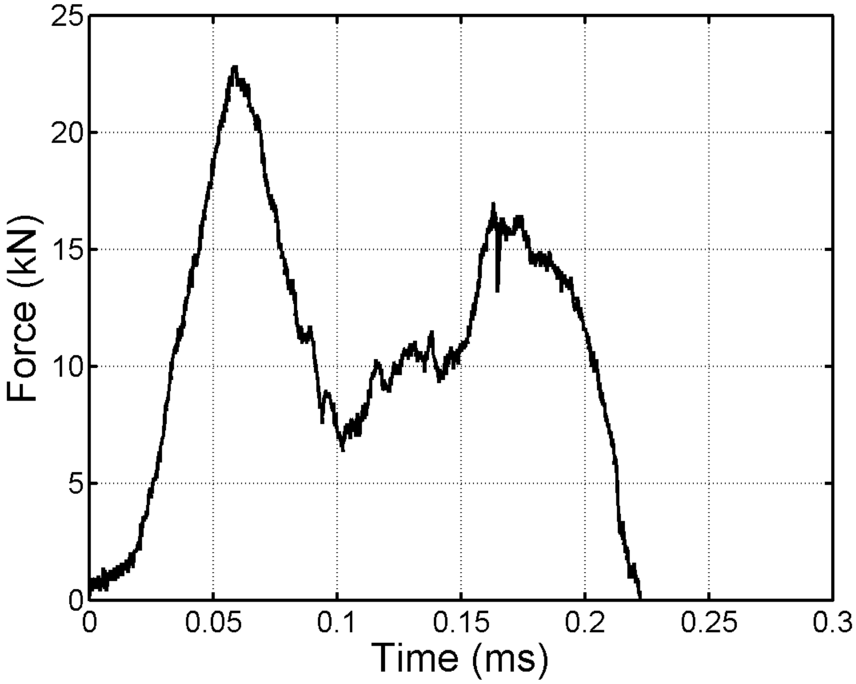

Figure C.39: UCSD Test 38; 50.8 mm diameter SHI at 73.9 m/s (158 J)

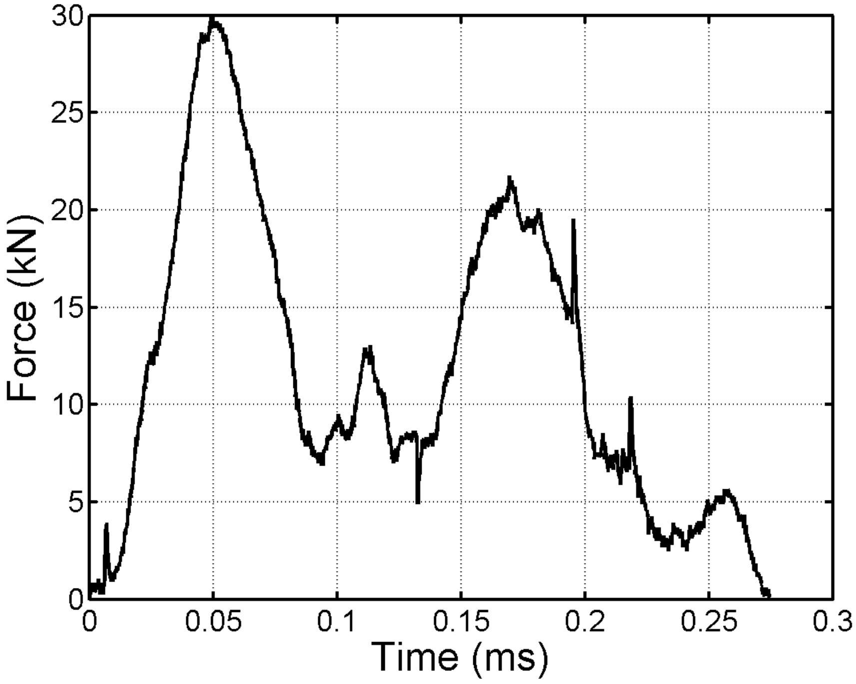

Figure C.40: UCSD Test 39; 61.0 mm diameter SHI at 72.6 m/s (281 J)

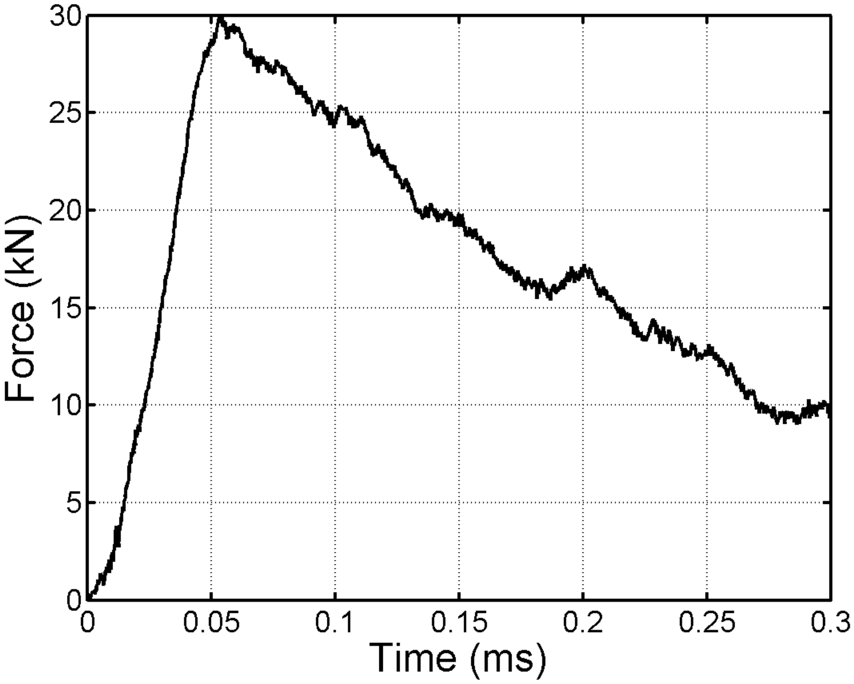

Figure C.41: UCSD Test 184; 61.0 mm diameter SHI at 81.2 m/s (363 J)

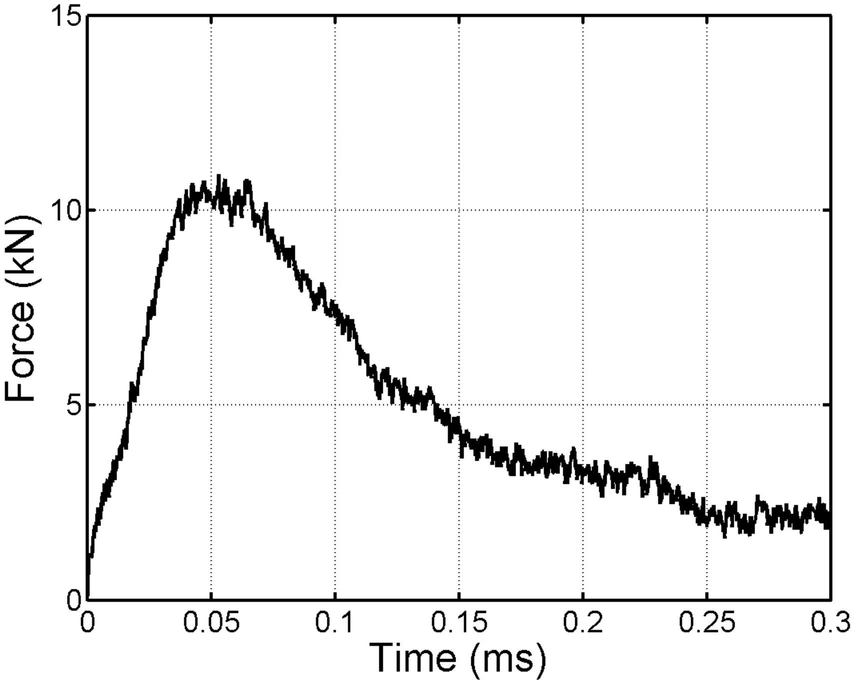

Figure C.42: UCSD Test 186; 50.8 mm diameter SHI at 63.6 m/s (116 J)

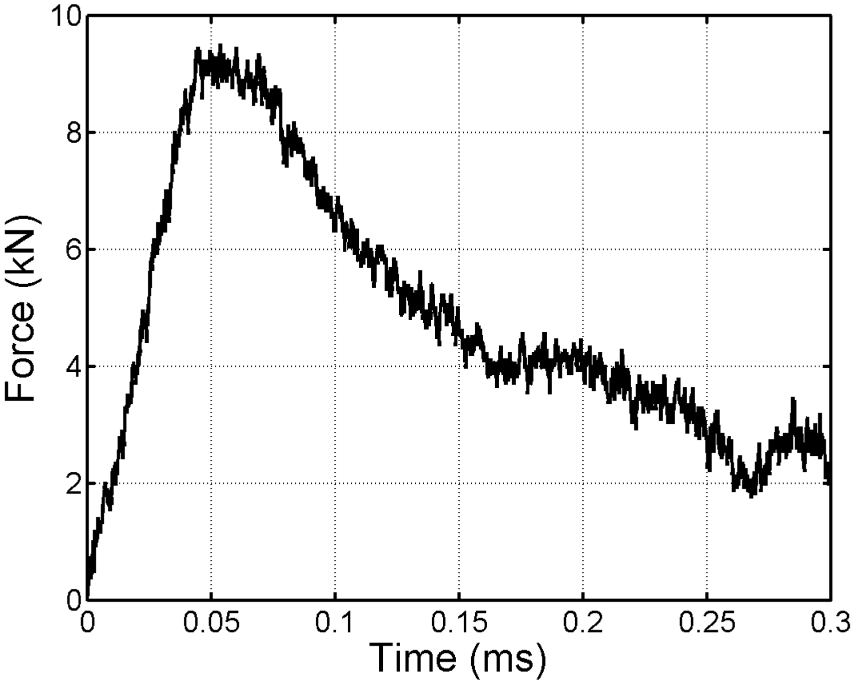

Figure C.43: UCSD Test 187; 50.8 mm diameter SHI at 63.9 m/s (112 J)

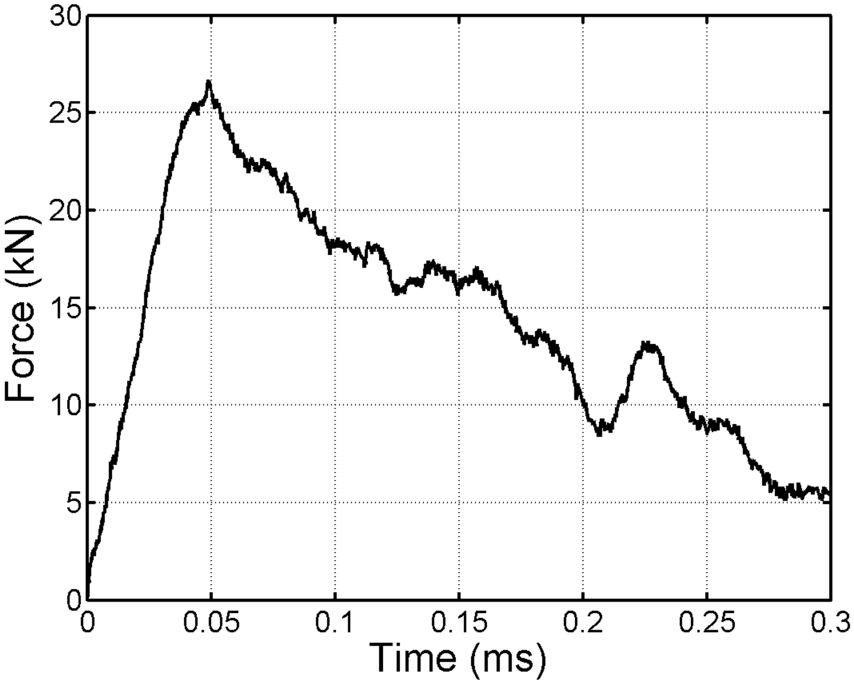

Figure C.44: UCSD Test 188; 61.0 mm diameter SHI at 98.9 m/s (516 J)

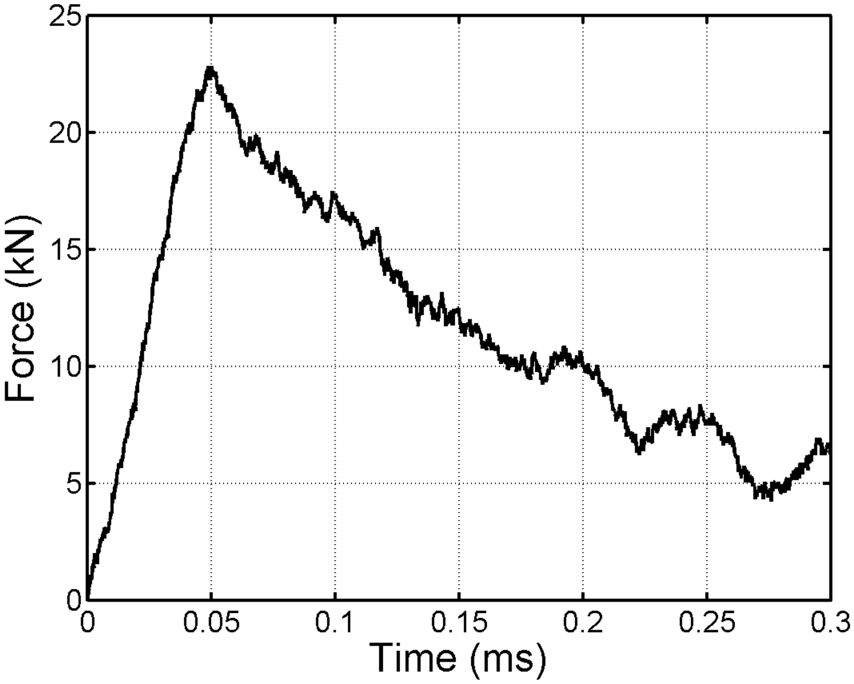

Figure C.45: UCSD Test 190; 61.0 mm diameter SHI at 80.4 m/s (352 J)

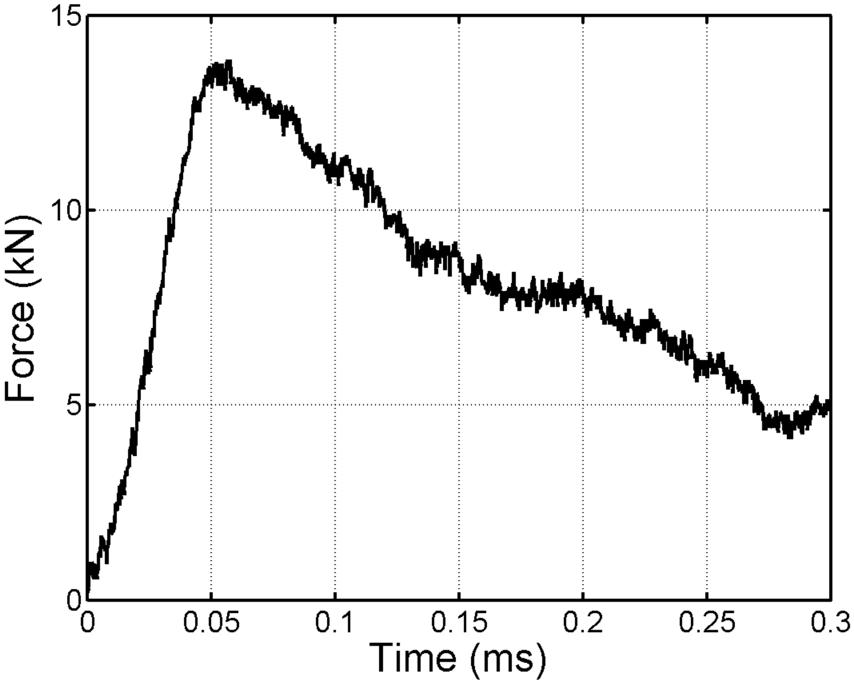

Figure C.46: UCSD Test 191; 61.0 mm diameter SHI at 61.8 m/s (201 J)

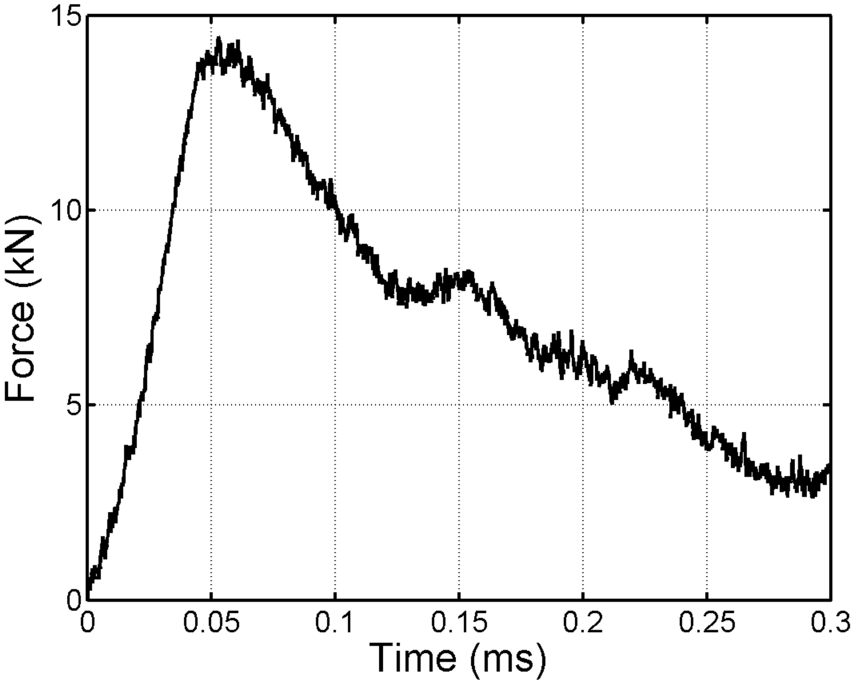

Figure C.47: UCSD Test 195; 50.8 mm diameter SHI at 60.6 m/s (114 J)

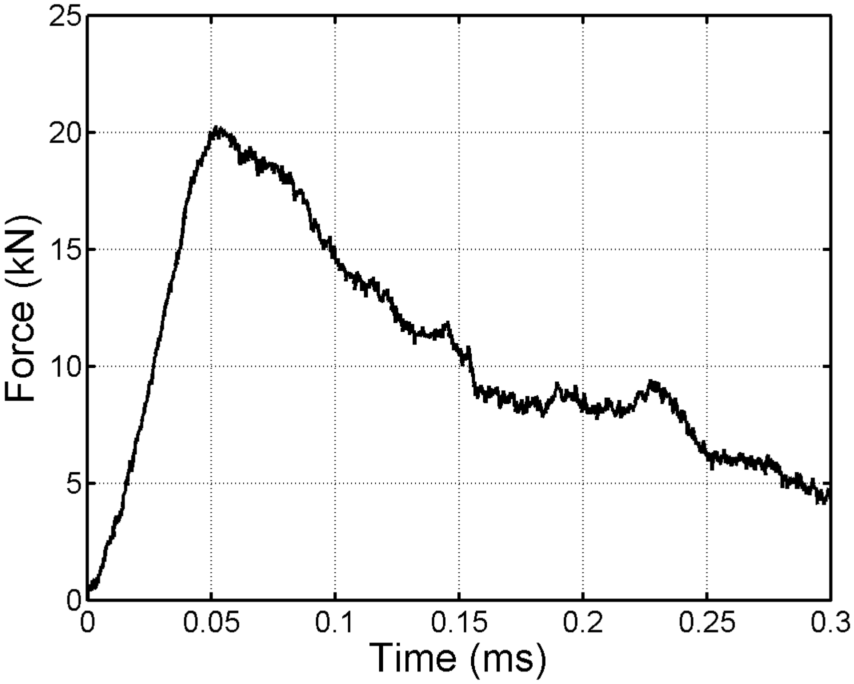

Figure C.48: UCSD Test 197; 50.8 mm diameter SHI at 82.2 m/s (209 J)

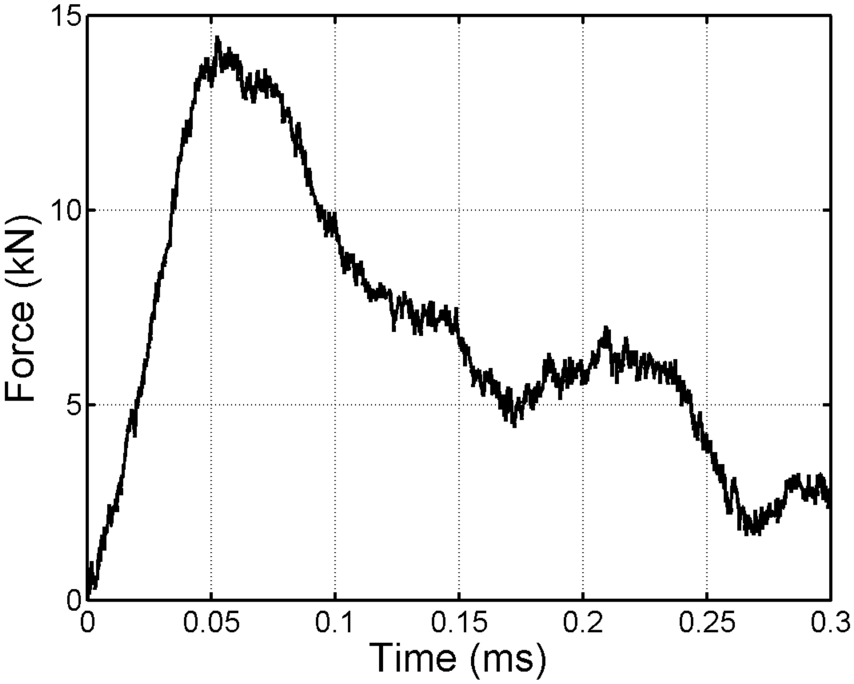

Figure C.49: UCSD Test 201; 50.8 mm diameter SHI at 59.3 m/s (111 J)

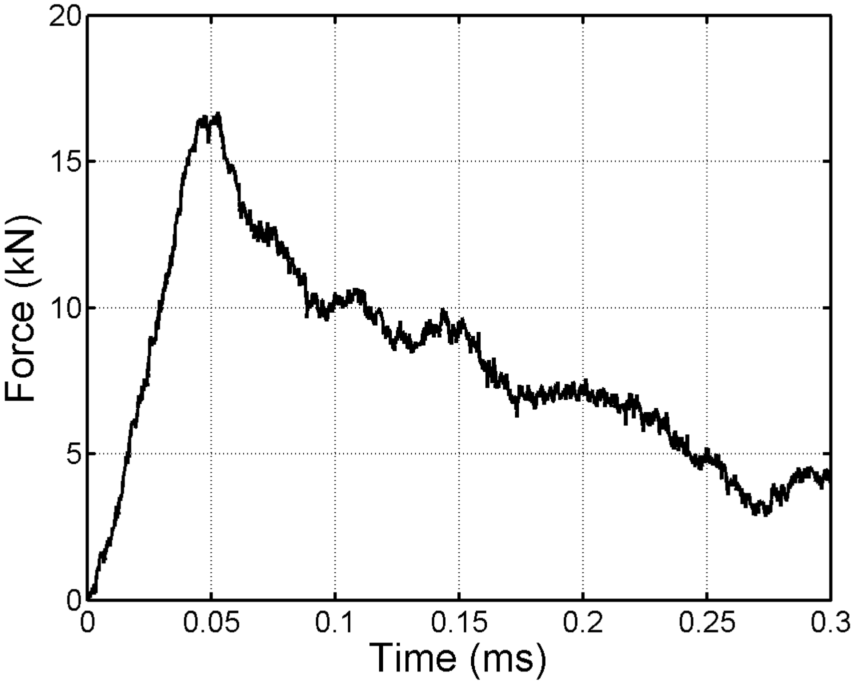

Figure C.50: UCSD Test 202; 50.8 mm diameter SHI at 62.6 m/s (124 J)

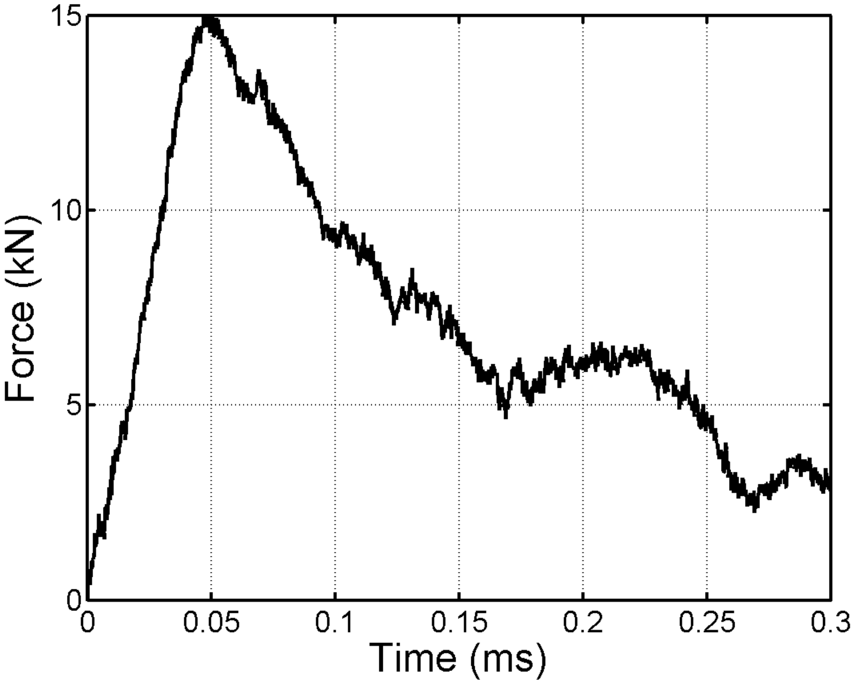

Figure C.51: UCSD Test 203; 50.8 mm diameter SHI at 61.2 m/s (118 J)

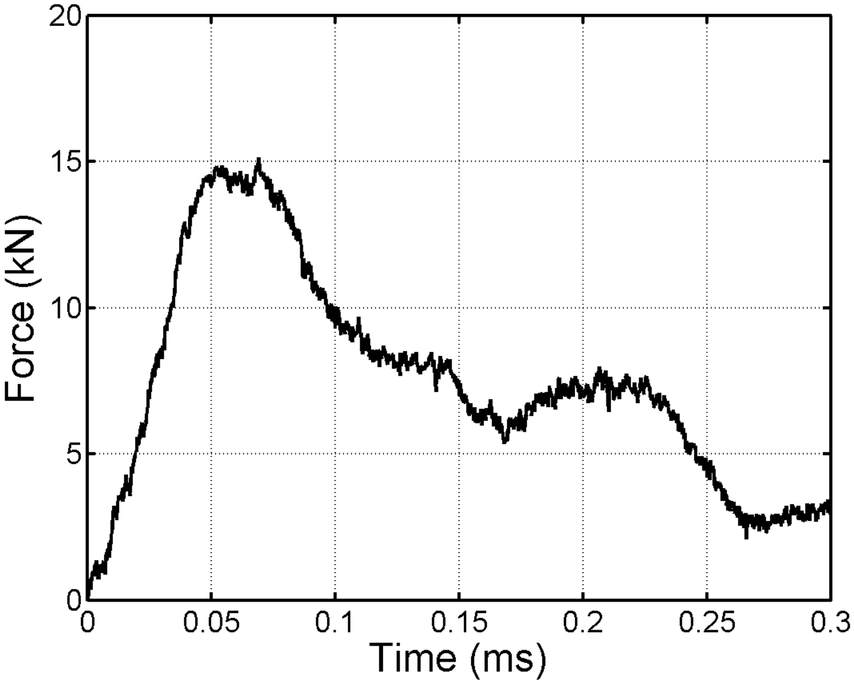

Figure C.52: UCSD Test 204; 50.8 mm diameter SHI at 61.2 m/s (119 J)

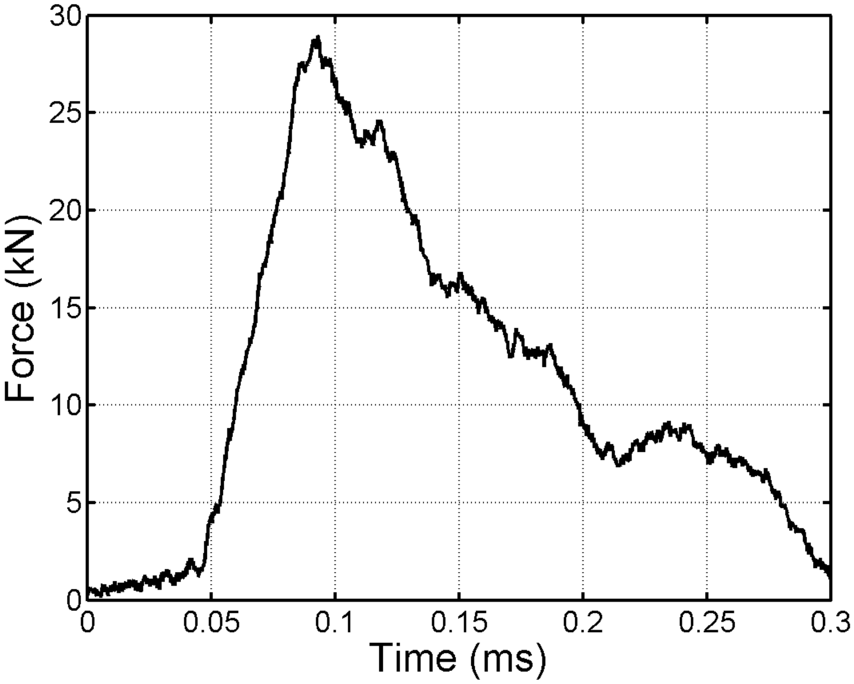

Figure C.53: UCSD Test 207; 38.1 mm diameter SHI at 133.7 m/s (238 J)

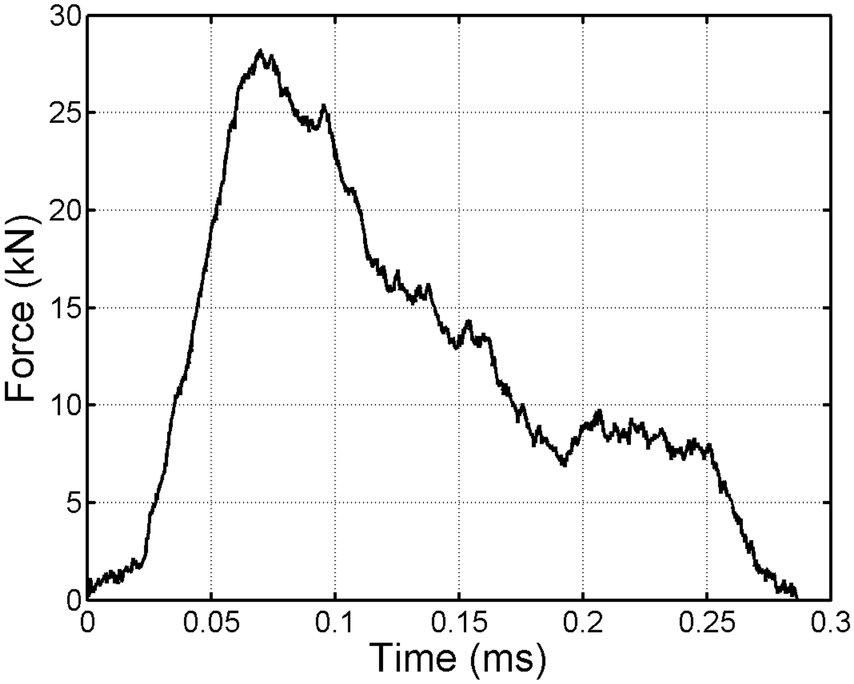

Figure C.54: UCSD Test 208; 38.1 mm diameter SHI at 136.1 m/s (238 J)

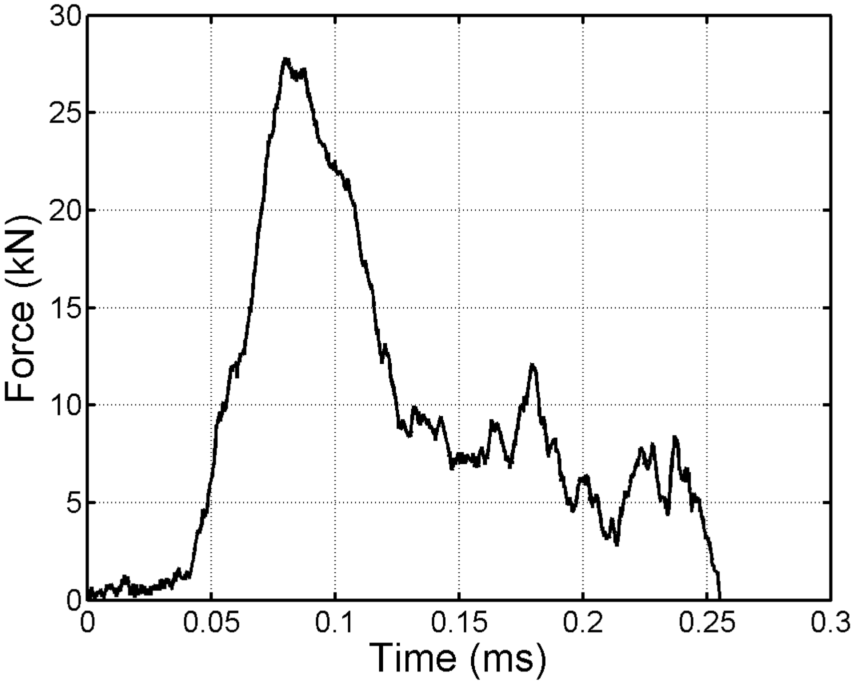

Figure C.55: UCSD Test 209; 38.1 mm diameter SHI at 134.6 m/s (236 J)

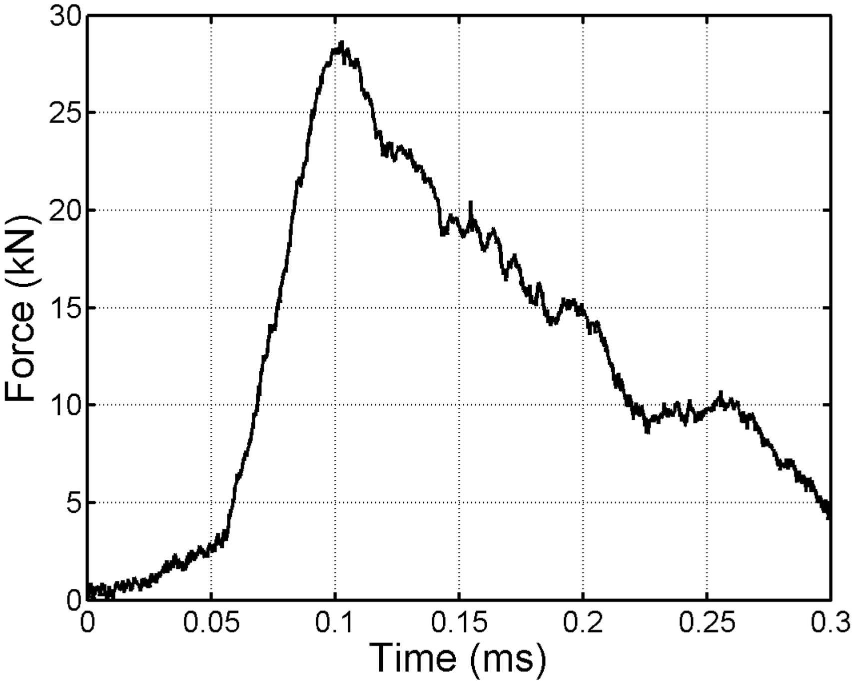

Figure C.56: UCSD Test 210; 38.1 mm diameter SHI at 135.4 m/s (246 J)

Appendix D. Summary of Simulation Results

Table D.1: All Simulations Performed with C1 – Avg.

SHI Diameter (mm)	Velocity (m/s)	KE (J)	Peak Force (kN)	Comparable Test ID
38.1	65.5	56	14.3	UCSD 1
38.1	144.1	271	34.6	UCSD 3
50.8	30.6	29	9.9	
50.8	43.3	58	14.0	
50.8	53.0	87	17.8	
50.8	60.6	114	20.9	UCSD 195 Kim et al. 49
50.8	61.2	116	21.3	UCSD 203
50.8	68.4	145	24.4	
50.8	75.0	174	27.1	
50.8	81.0	203	32.8	UCSD 197
50.8	86.6	231	33.7	
50.8	91.8	260	35.1	
50.8	96.8	289	37.2	
50.8	100.0	309	38.8	Kim et al. 48
50.8	107.3	356	42.9	UCSD 29
50.8	125.0	483	50.1	
50.8	144.1	641	59.2	UCSD 11
50.8	150.0	695	62.0	
50.8	175.0	946	77.6	
50.8	190.0	1115	87.6	
61.0	30.6	50	14.3	
61.0	43.3	100	19.8	Purdue 28
61.0	53.0	150	25.6	
61.0	61.2	200	30.3	UCSD 191
61.0	68.4	250	36.6	
61.0	75.0	300	41.3	
61.0	81.0	350	43.5	UCSD 184
61.0	86.6	400	46.8	
61.0	190.0	1927	127.6	Purdue 124

Table D.2: All Simulations Performed with C2 – Lower

SHI Diameter (mm)	Velocity (m/s)	KE (J)	Peak Force (kN)	Comparable Test ID
38.1	144.1	271	29.2	UCSD 3
50.8	60.7	114	16.9	UCSD 195 Kim et al. 49
50.8	107.3	356	33.6	UCSD 29
50.8	144.1	641	51.1	UCSD 11
60.8	190.0	1927	118.6	Purdue 124

Table D.3: All Simulations Performed with C3 - Upper

SHI Diameter (mm)	Velocity m/s)	KE (J)	Peak Force (kN)	Comparable Test ID
38.1	136.7	244	39.1	UCSD 3
50.8	60.7	114	24.6	UCSD 195 Kim et al. 49
50.8	107.3	356	48.6	UCSD 29
50.8	144.1	641	67.7	UCSD 11
60.8	190.0	1927	135.9	Purdue 124

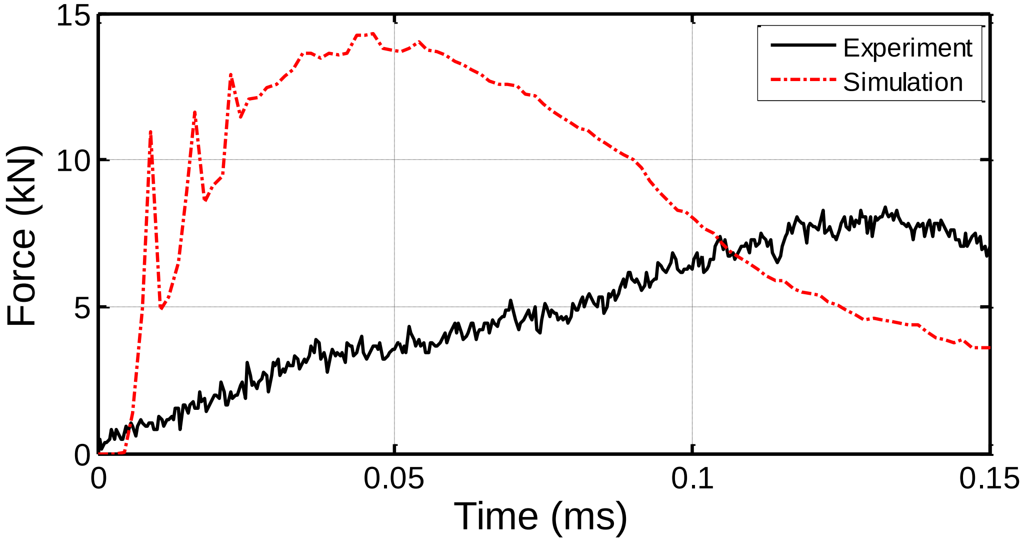

Figure D.1: Simulation results using C1 –Avg: 38.1 mm diameter SHI at 65.5 m/s (56 J); Compared to UCSD Test 1: 69.2 m/s (56 J)

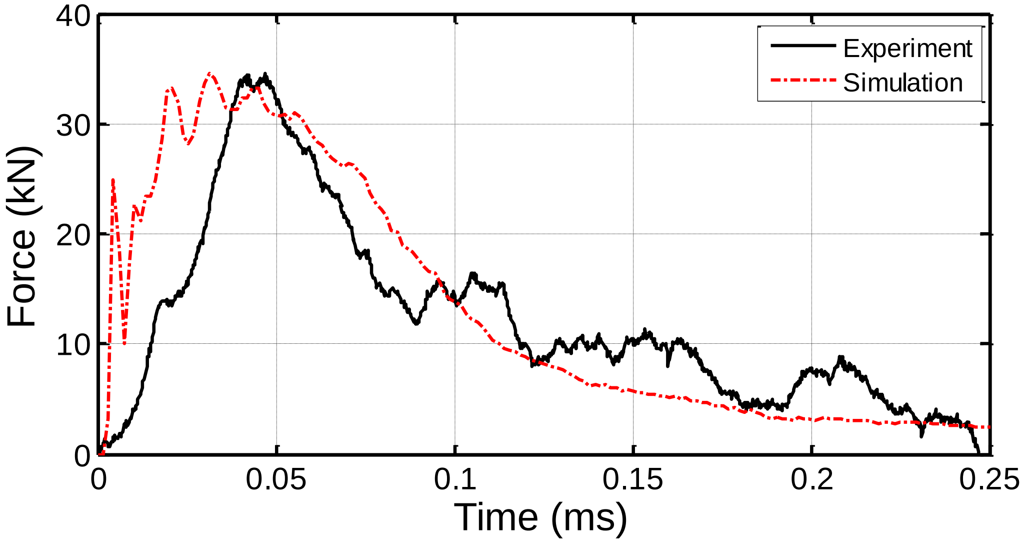

Figure D.2: Simulation results using C1 –Avg: 38.1 mm diameter SHI at 144.1 m/s (271 J); Compared to UCSD Test 3: 142 m/s (248 J)

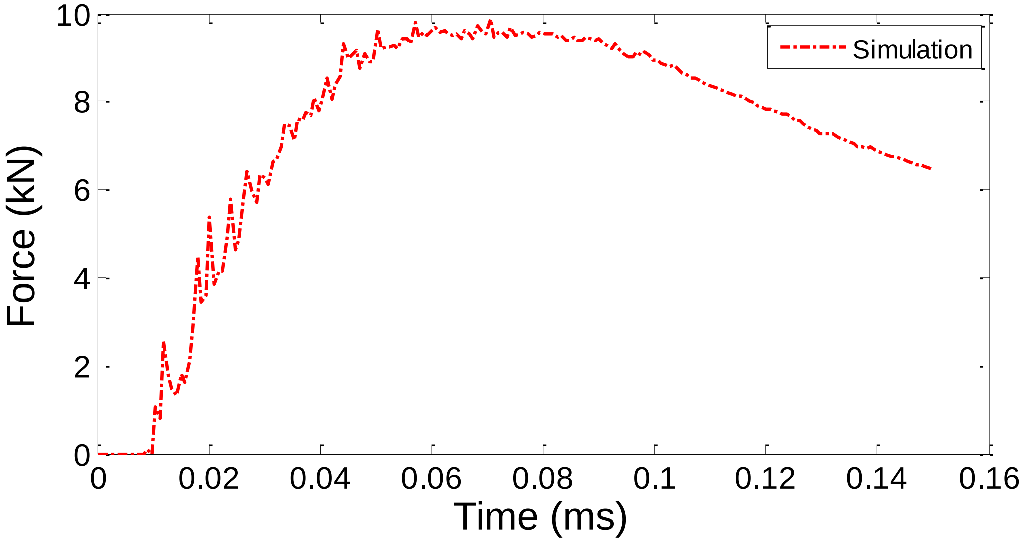

Figure D.3: Simulation results using C1 –Avg: 50.8 mm diameter SHI at 30.6 m/s (29 J)

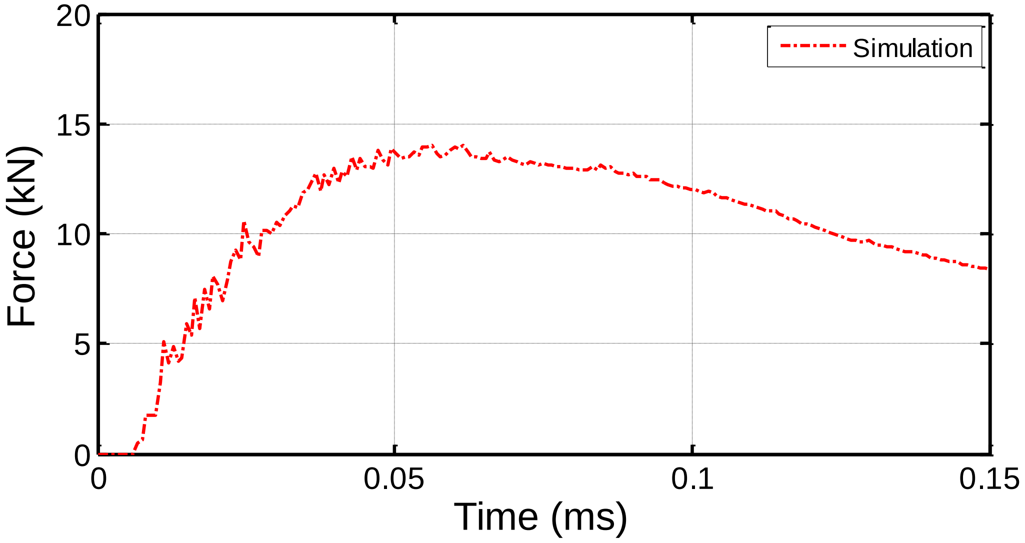

Figure D.4: Simulation results using C1 –Avg: 50.8 mm diameter SHI at 43.3 m/s (58 J)

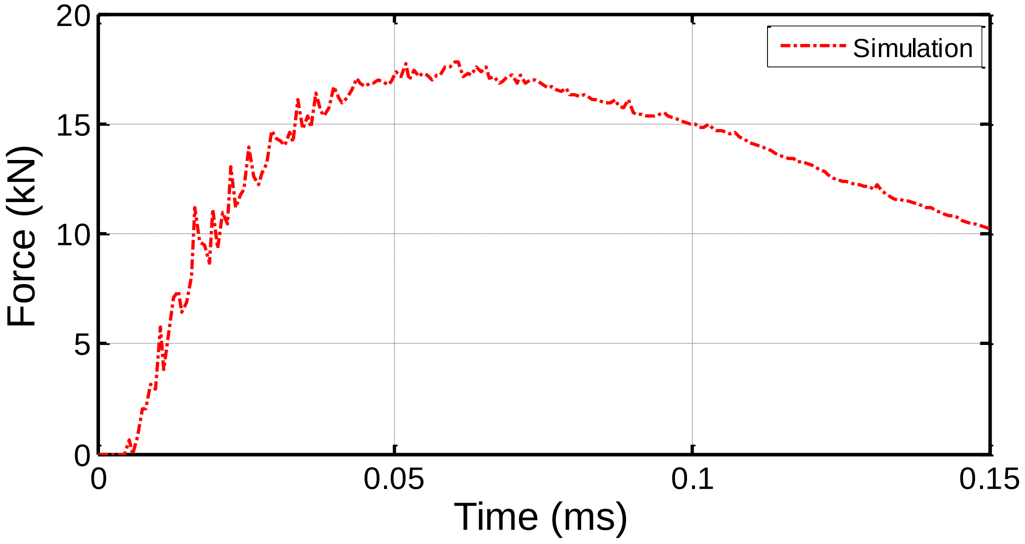

Figure D.5: Simulation results using C1 –Avg: 50.8 mm diameter SHI at 53.0 m/s (87 J)

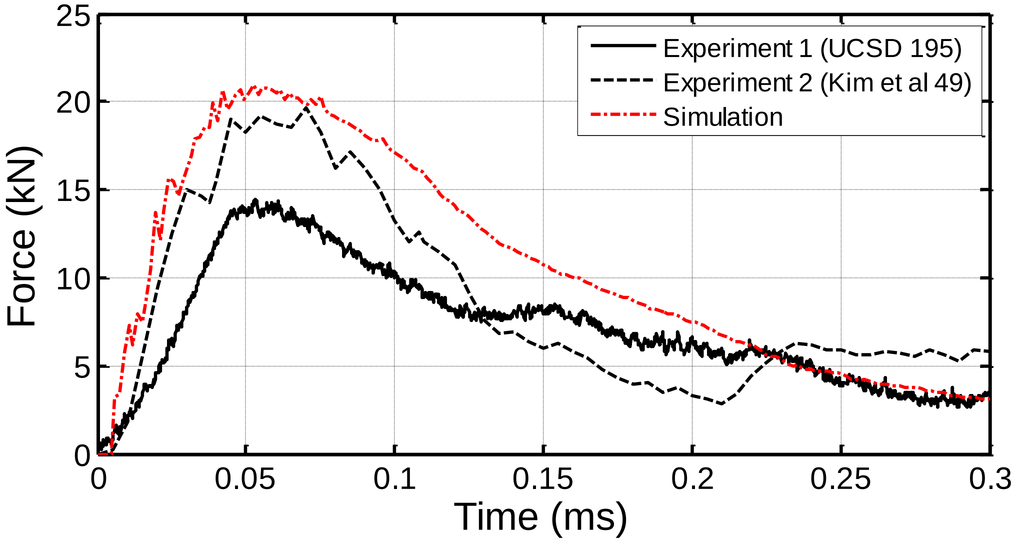

Figure D.6: Simulation results using C1 –Avg: 50.8 mm diameter SHI at 60.6 m/s (114 J); Compared to UCST Test 195: 60.6 m/s (114 J) and Kim et al. Test 49: 61.9 m/s (108 J)

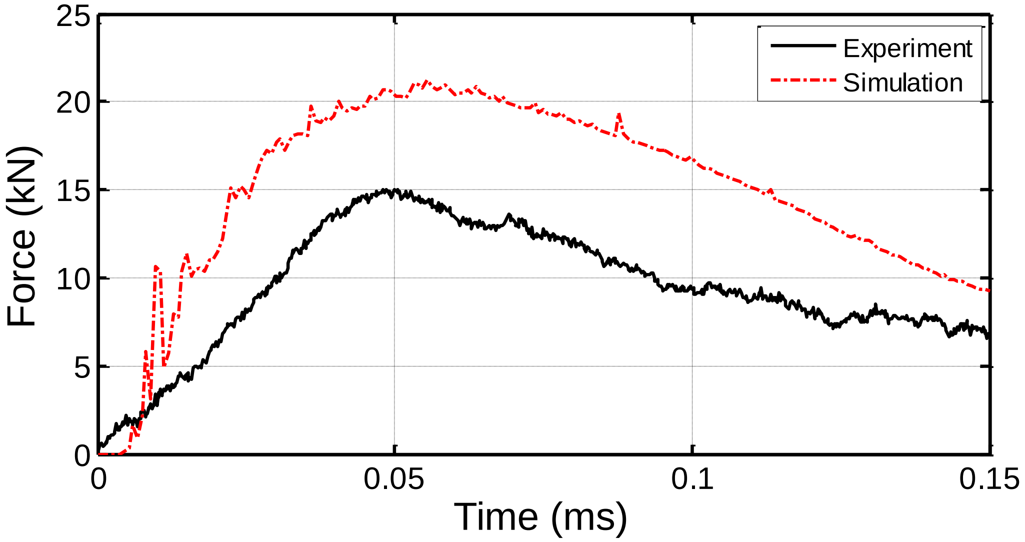

Figure D.7: Simulation results using C1 –Avg: 50.8 mm diameter SHI at 61.2 m/s (116 J); Compared to UCSD Test 203: 61.2 m/s (118 J)

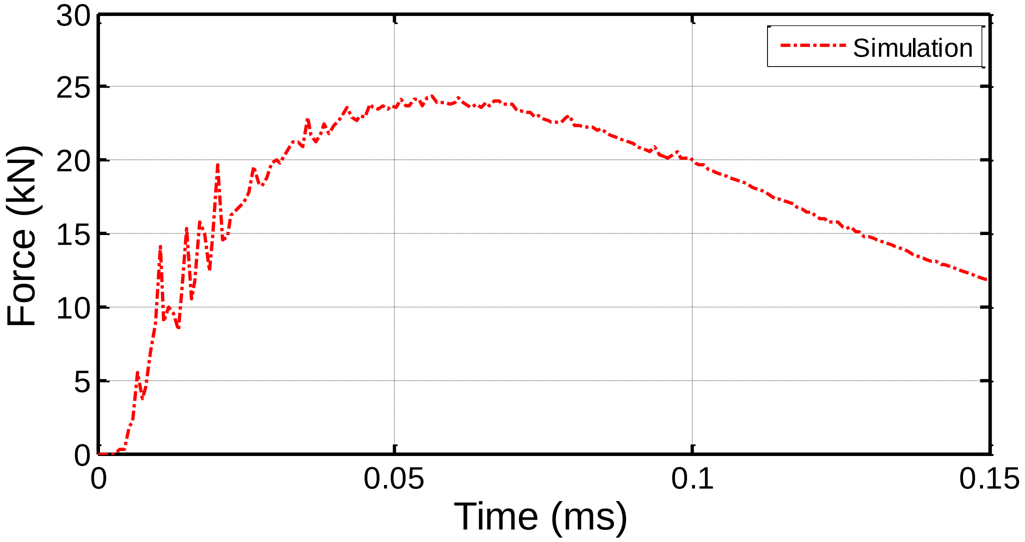

Figure D.8: Simulation results using C1 –Avg: 50.8 mm diameter SHI at 68.4 m/s (145 J)

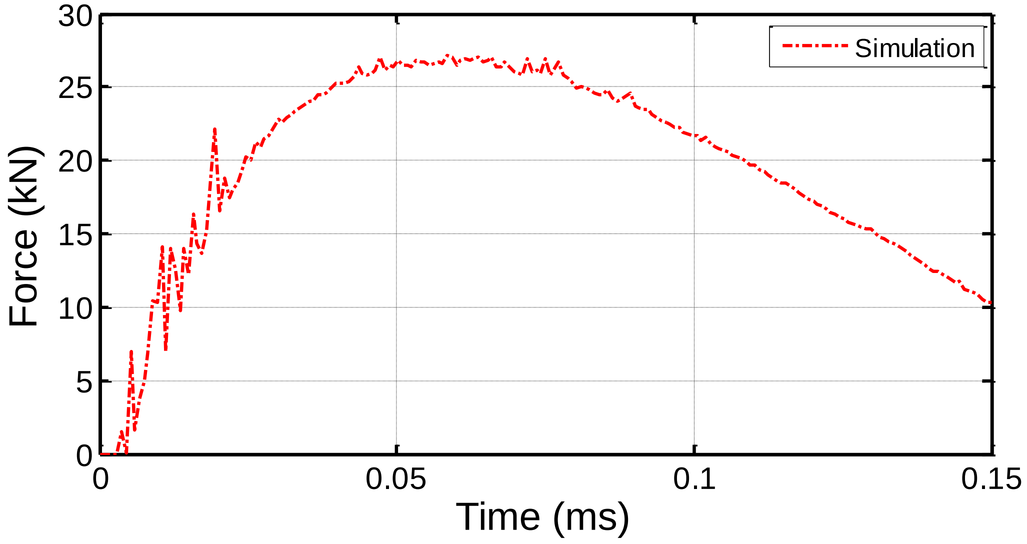

Figure D.9: Simulation results using C1 –Avg: 50.8 mm diameter SHI at 75.0 m/s (174 J)

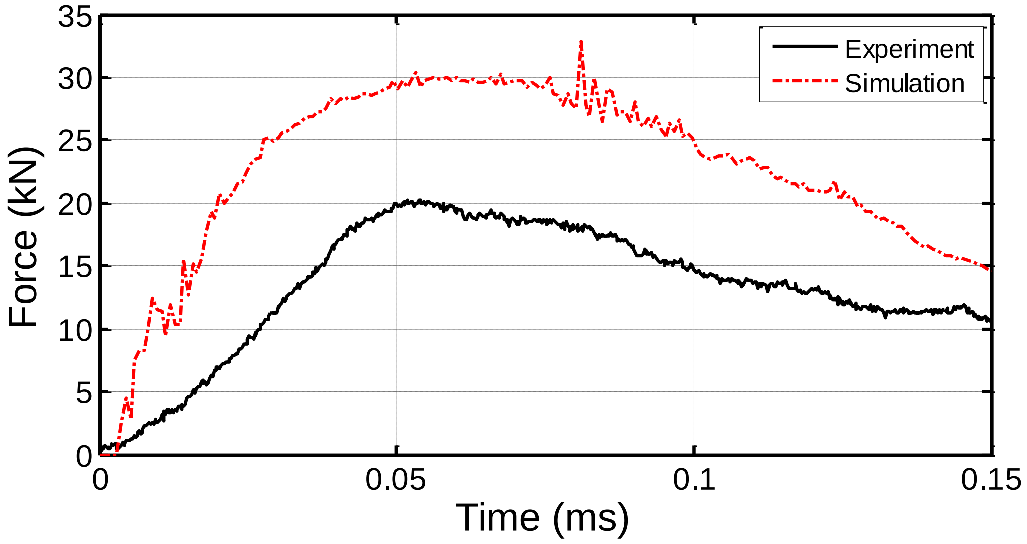

Figure D.10: Simulation results using C1 –Avg: 50.8 mm diameter SHI at 81.0 m/s (203 J); Compared to UCSD Test 197: 82.2 m/s at (209 J)

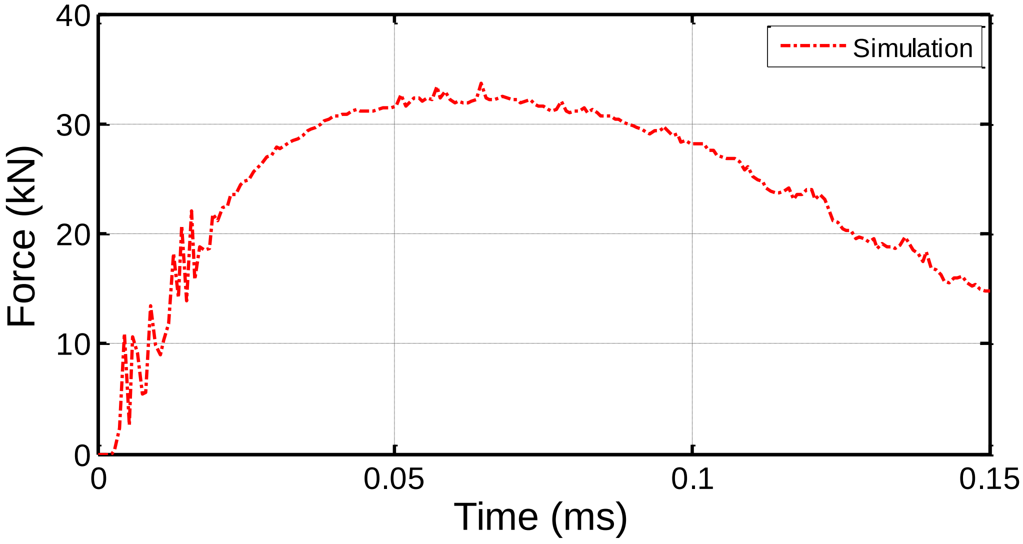

Figure D.11: Simulation results using C1 –Avg: 50.8 mm diameter SHI at 86.6 m/s (231 J)

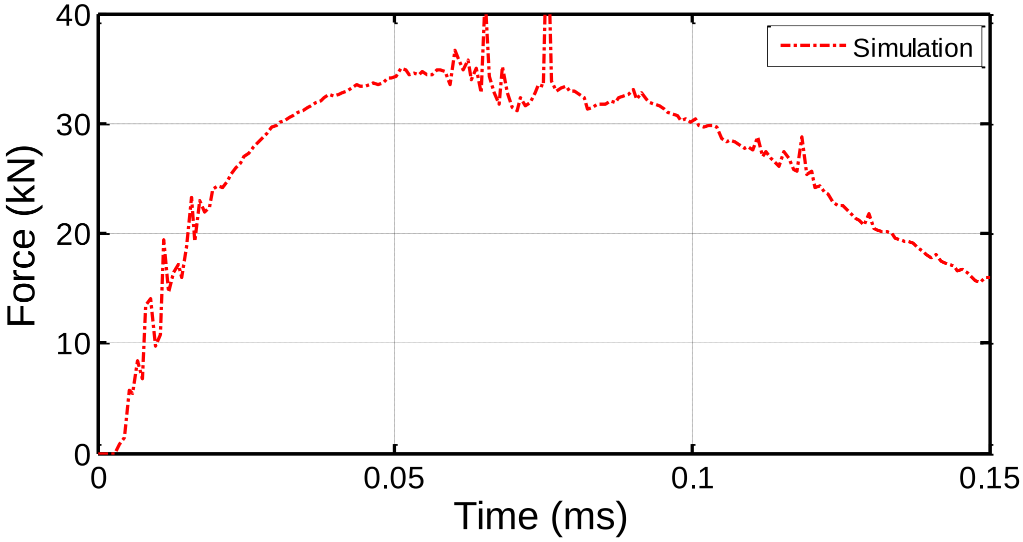

Figure D.12: Simulation results using C1 –Avg: 50.8 mm diameter SHI at 91.8 m/s at (260 J)

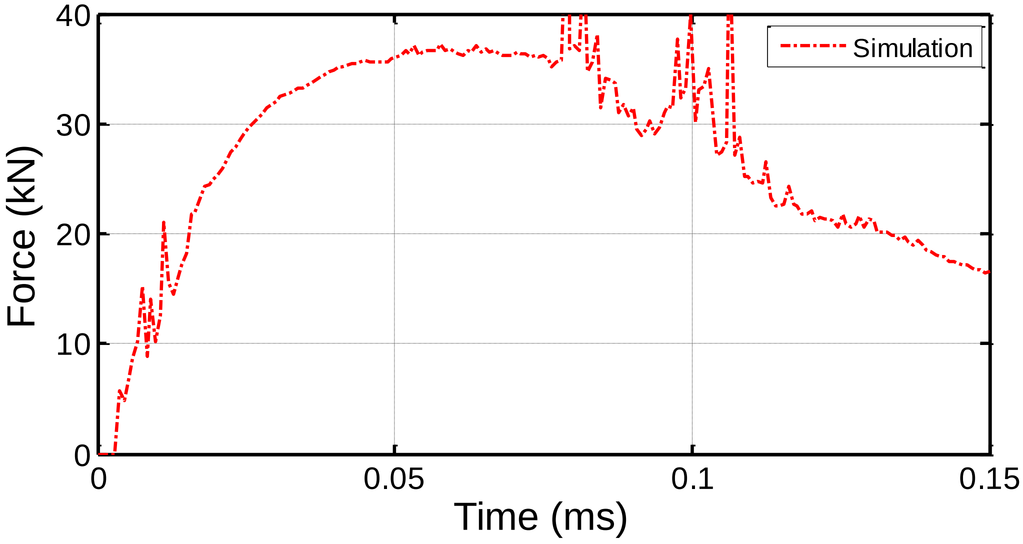

Figure D.13: Simulation results using C1 –Avg: 50.8 mm diameter SHI at 96.8 m/s (289 J)

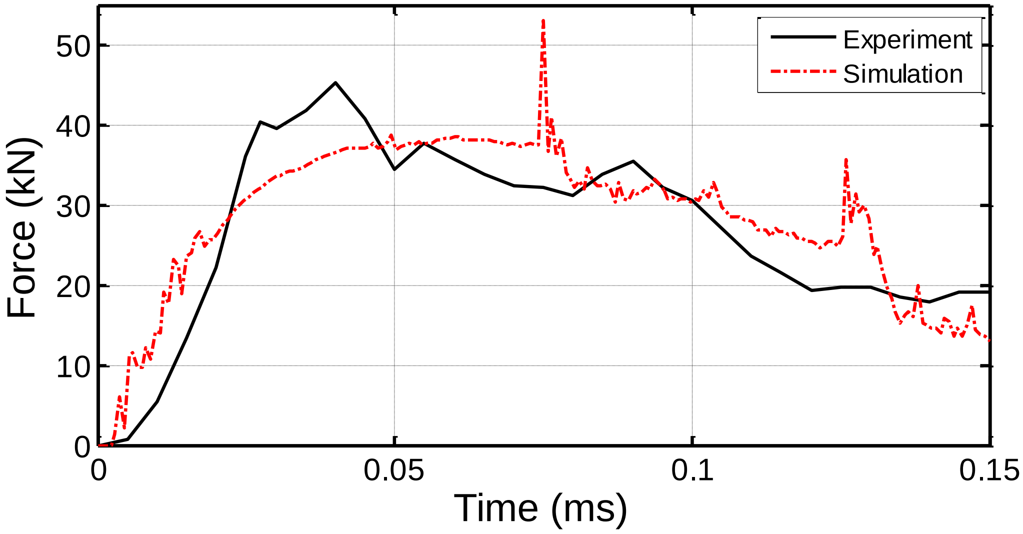

Figure D.14: Simulation results using C1 –Avg: 50.8 mm diameter SHI at 100.0 m/s (309 J); Compared to Kim et al. Test 48: 104.6 m/s (309 J)

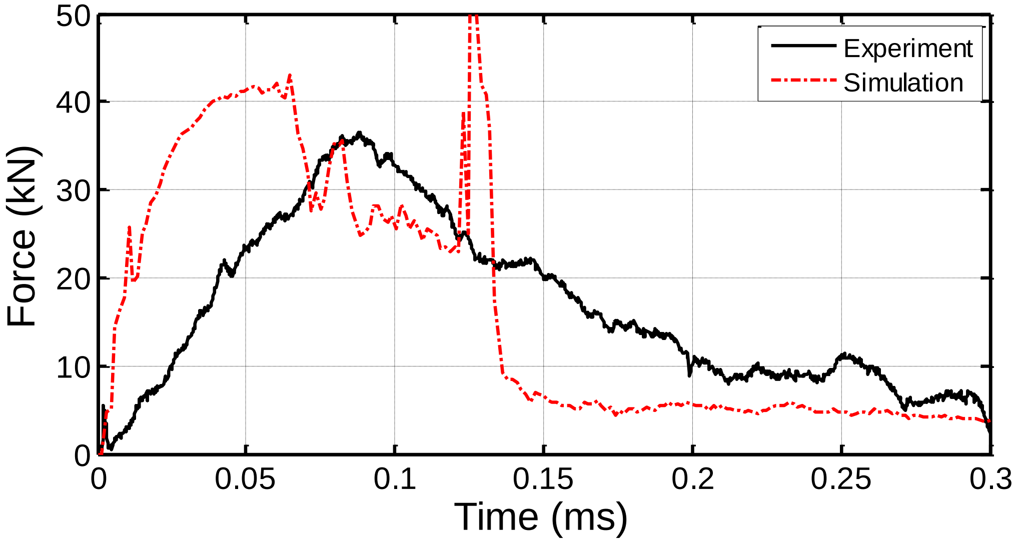

Figure D.15: Simulation results using C1 –Avg: 50.8 mm diameter SHI at 107.3 m/s (356 J); Compared to UCSD Test 29: 109.9 m/s (356 J)

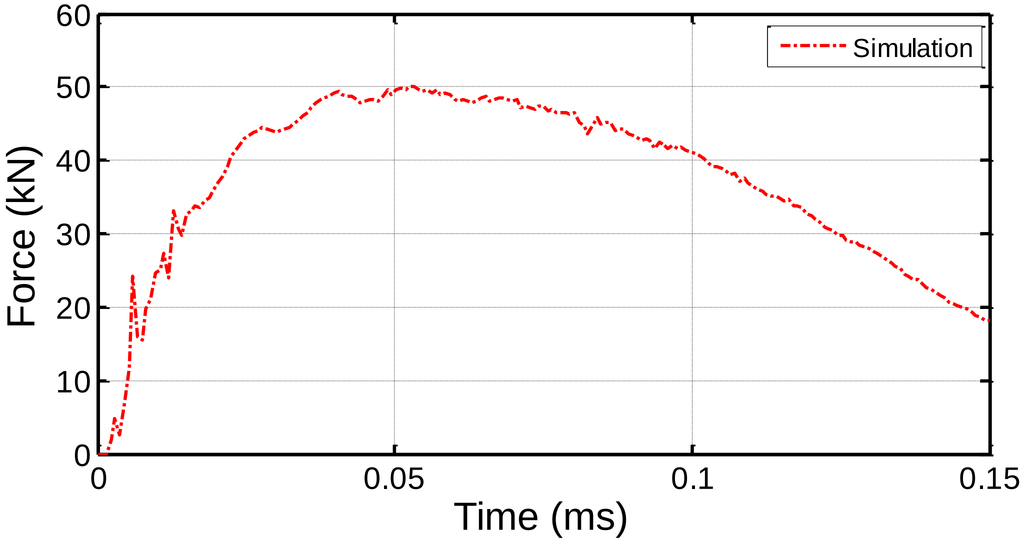

Figure D.16: Simulation results using C1 –Avg: 50.8 mm diameter SHI at 125.0 m/s (483 J)

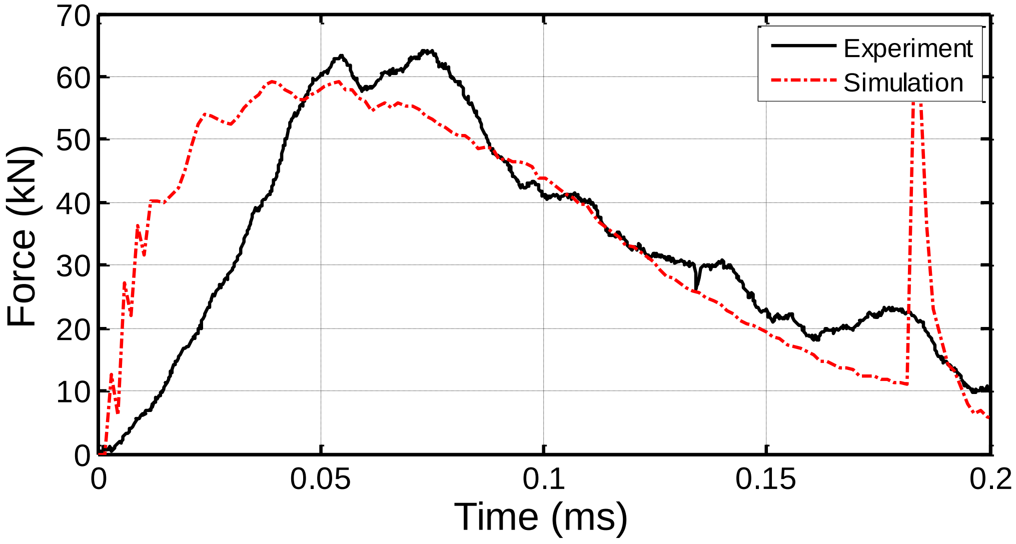

Figure D.17: Simulation results using C1 –Avg: 50.8 mm diameter SHI at 144.1 m/s (641 J); Compared to UCSD Test 29: 144.2 m/s (641 J)

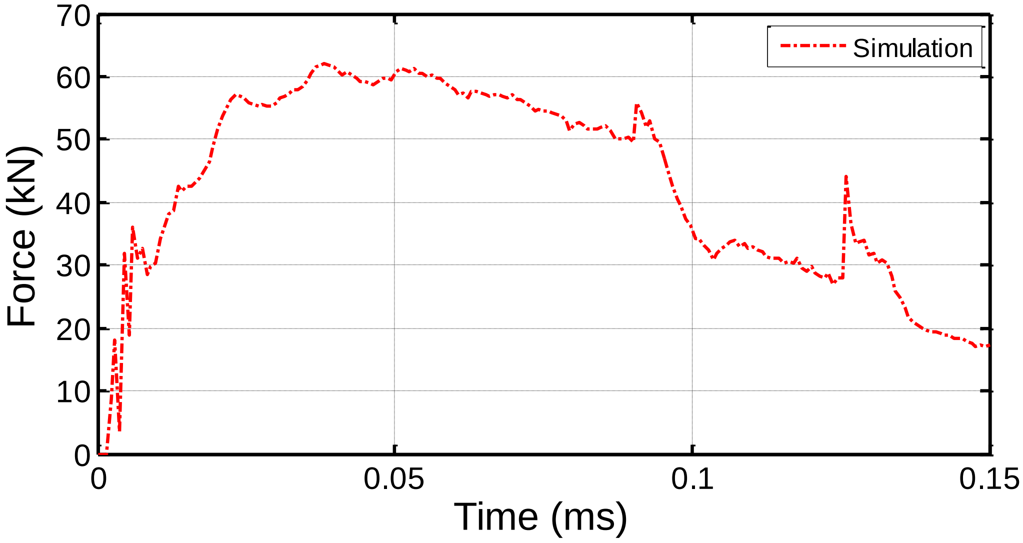

Figure D.18: Simulation results using C1 –Avg: 50.8 mm diameter SHI at 150.0 m/s (695 J)

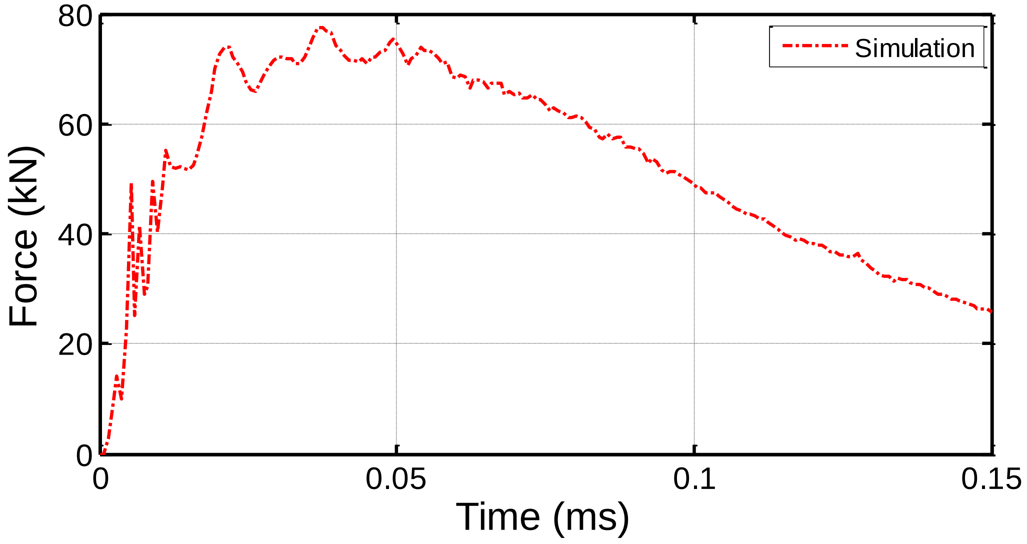

Figure D.19: Simulation results using C1 –Avg: 50.8 mm diameter SHI at 175.0 m/s (946 J)

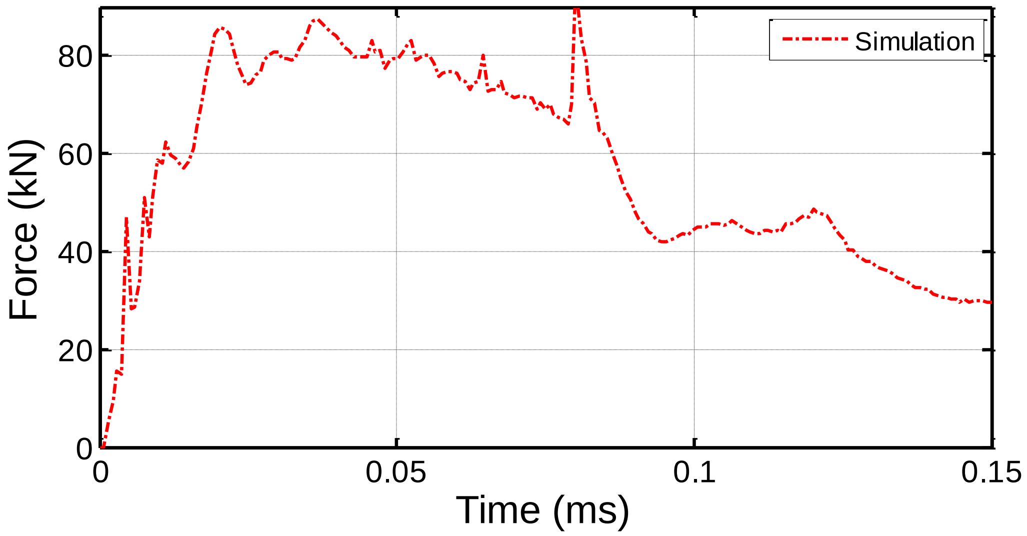

Figure D.20: Simulation results using C1 –Avg: 50.8 mm diameter SHI at 190.0 m/s (1115 J)

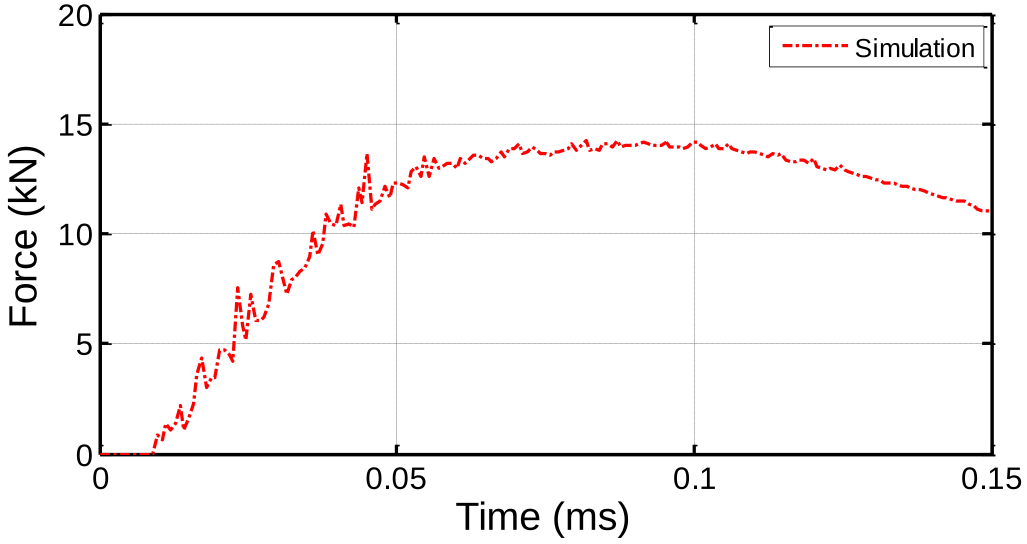

Figure D.21: Simulation results using C1 –Avg: 61.0 mm diameter SHI at 30.6 m/s (50 J)

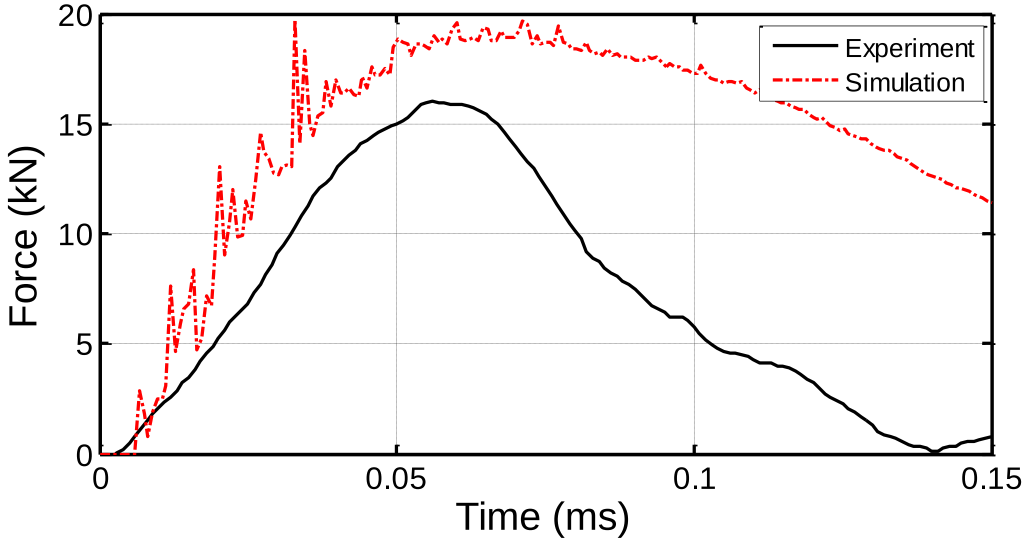

Figure D.22: Simulation results using C1 –Avg: 61.0 mm diameter SHI at 43.3 m/s (100 J); Compared to Purdue Test 28: 45.4 m/s (110 J)

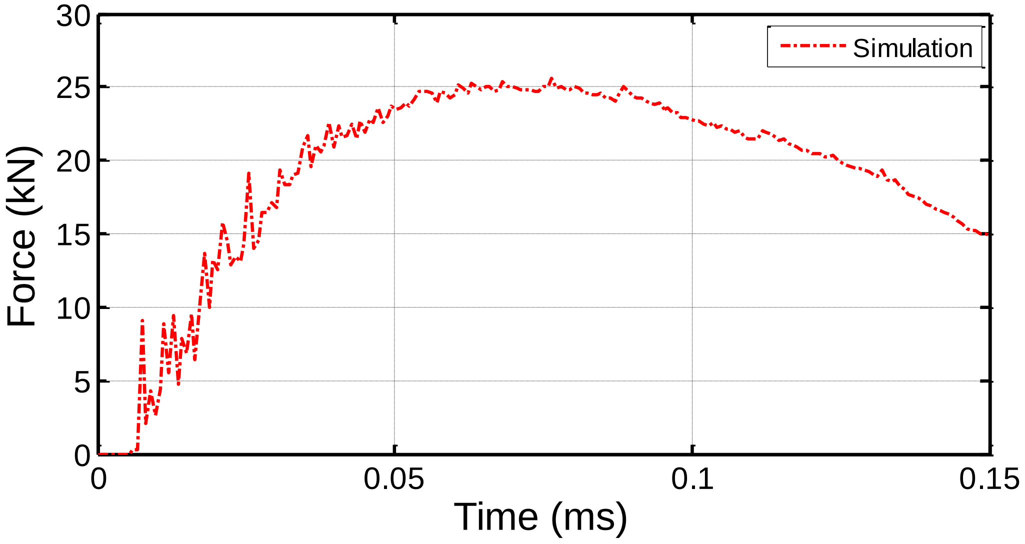

Figure D.23: Simulation results using C1 –Avg: 61.0 mm diameter SHI at 53.0 m/s (150 J)

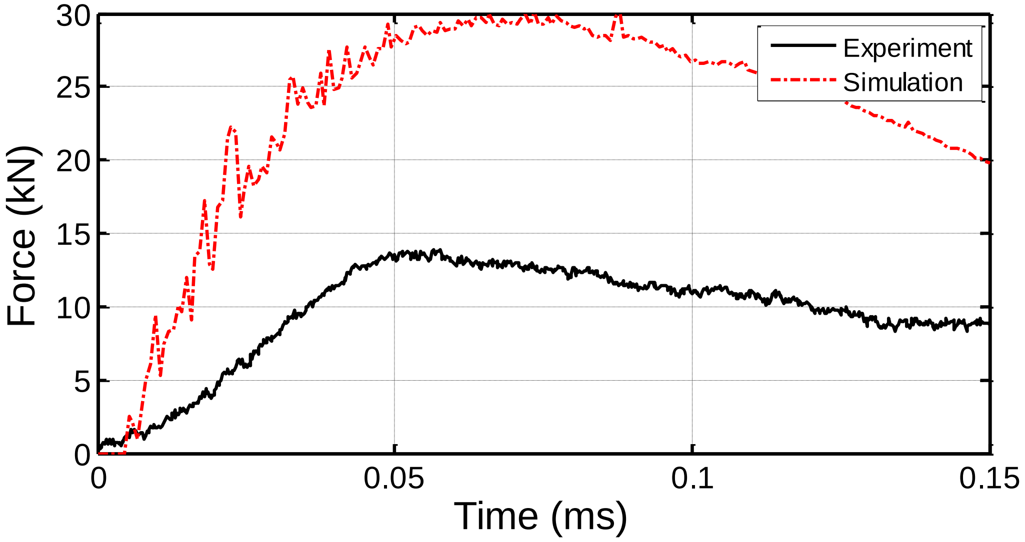

Figure D.24: Simulation results using C1 –Avg: 61.0 mm diameter SHI at 61.2 m/s (200 J); Compared to UCSD Test 191: 61.7 m/s (201 J)

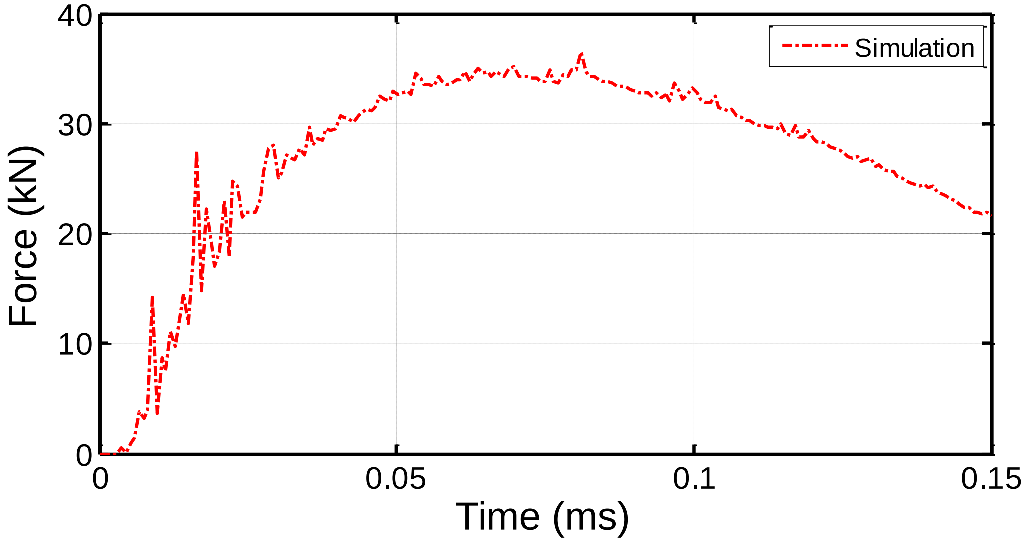

Figure D.25: Simulation results using C1 –Avg: 61.0 mm diameter SHI at 68.4 m/s (250 J)

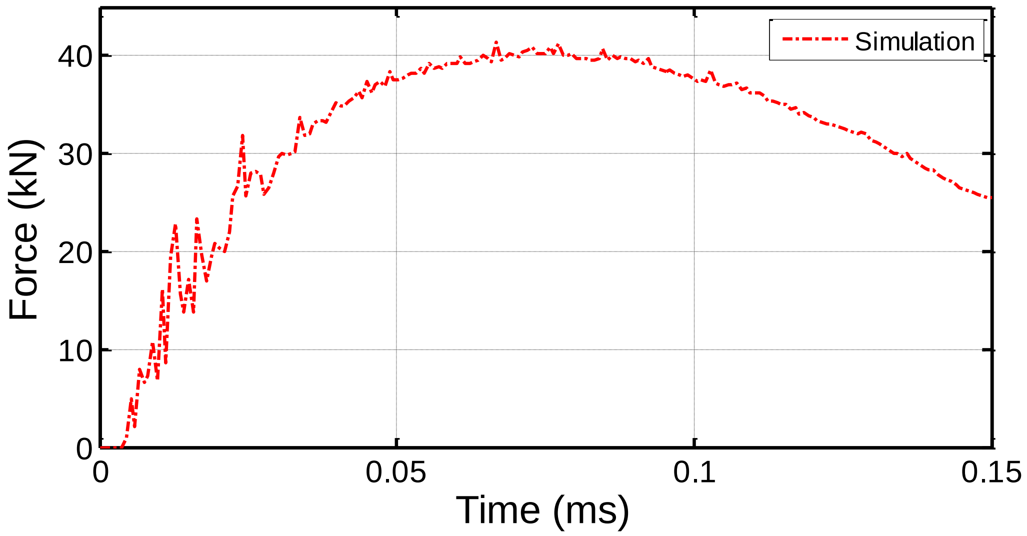

Figure D.26: Simulation results using C1 –Avg: 61.0 mm diameter SHI at 75.0 m/s (300 J)

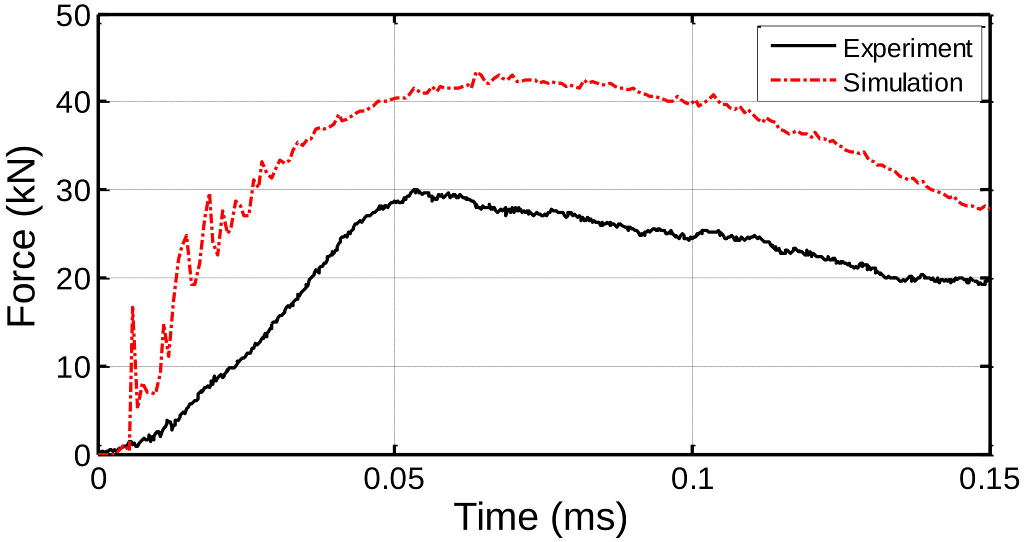

Figure D.27: Simulation results using C1 –Avg: 61.0 mm diameter SHI at 81.0 m/s (350 J); Compared to UCSD Test 184: 81.2 m/s (363.2 J)

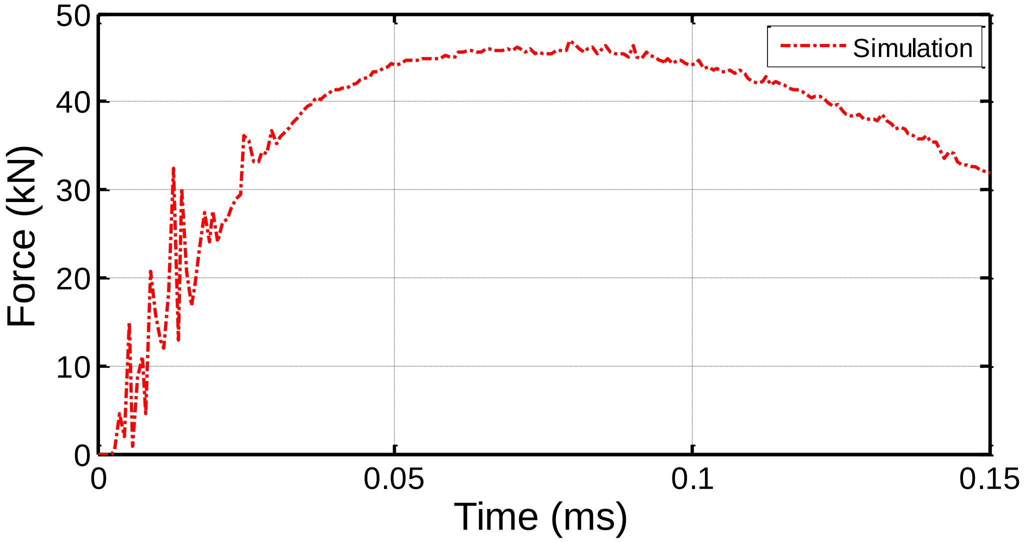

Figure D.28: Simulation results using C1 –Avg: 61.0 mm diameter SHI at 86.6 m/s (400 J)

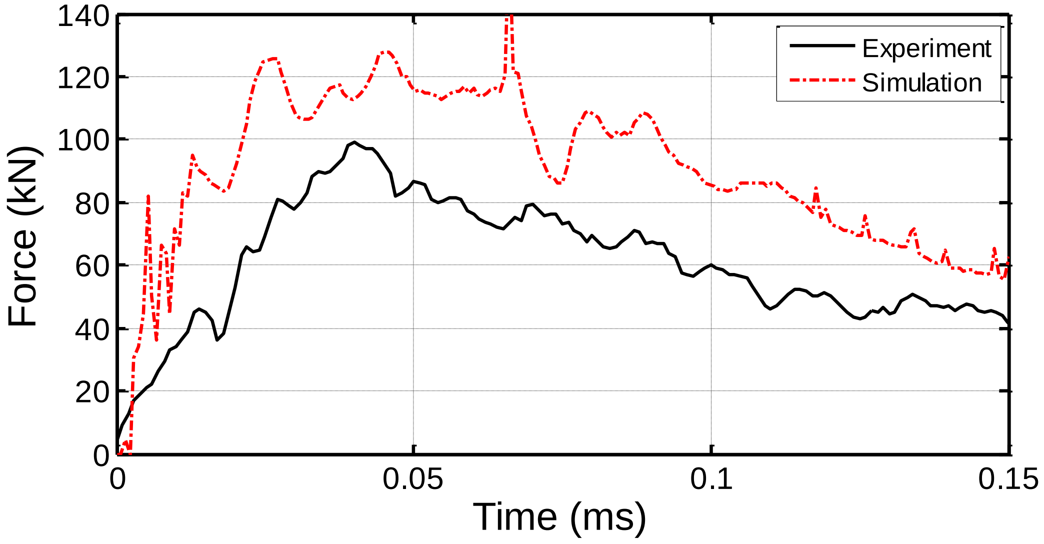

Figure D.29: Simulation results using C1 –Avg: 61.0 mm diameter SHI at 190.0 m/s (1927 J); Compared to Purdue Test 124: 189.2 m/s (1932 J)

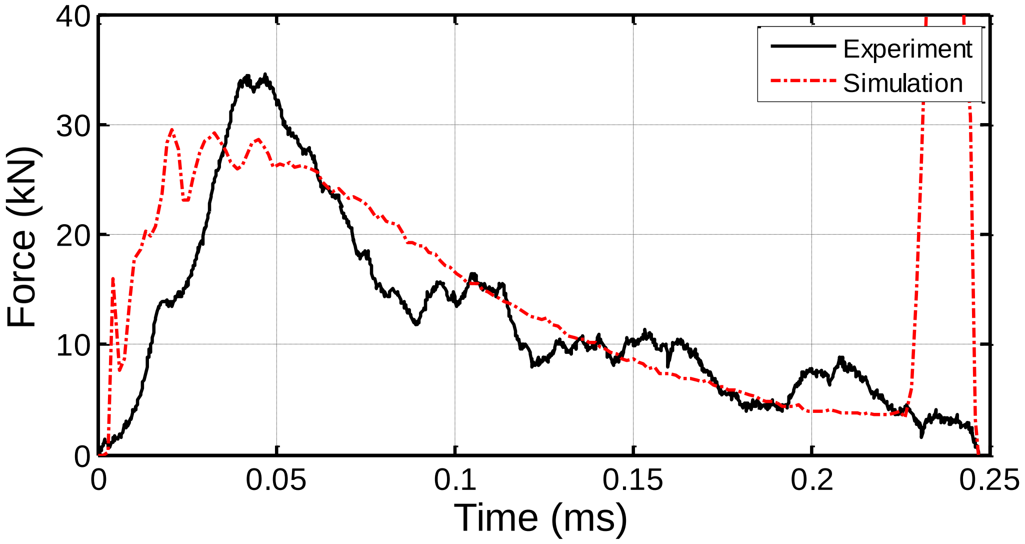

Figure D.30: Simulation results using C2- Lower: 38.1 mm diameter SHI at 144.1 m/s (271 J); Compared to UCSD Test 3:142.0 m/s (248 J)

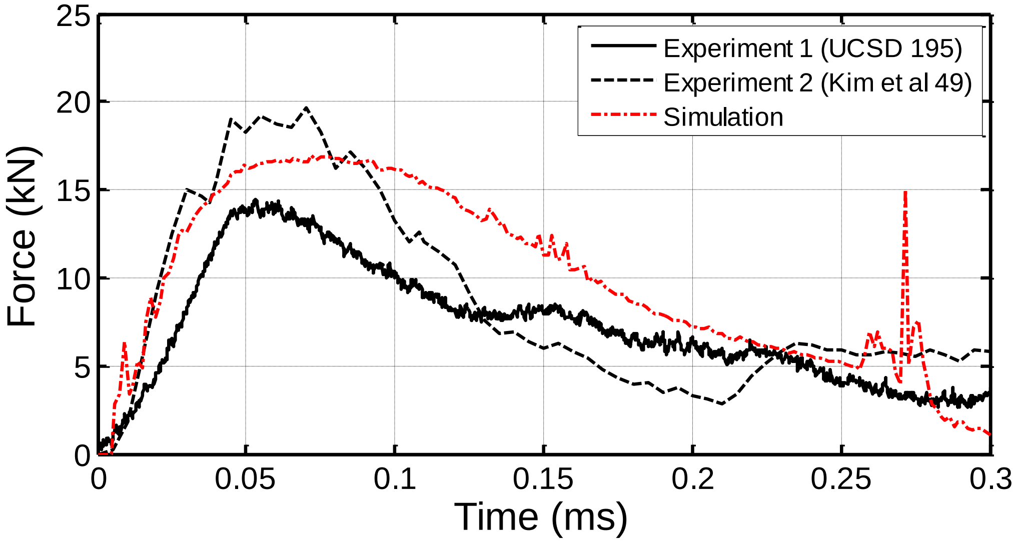

Figure D. 31: Simulation results using C2 – Lower: 50.8 mm diameter SHI at 60.6 m/s (114 J); Compared to UCSD Test 195: 60.6 m/s (114 J) and Kim et al. Test 49: 61.9 m/s (108 J)

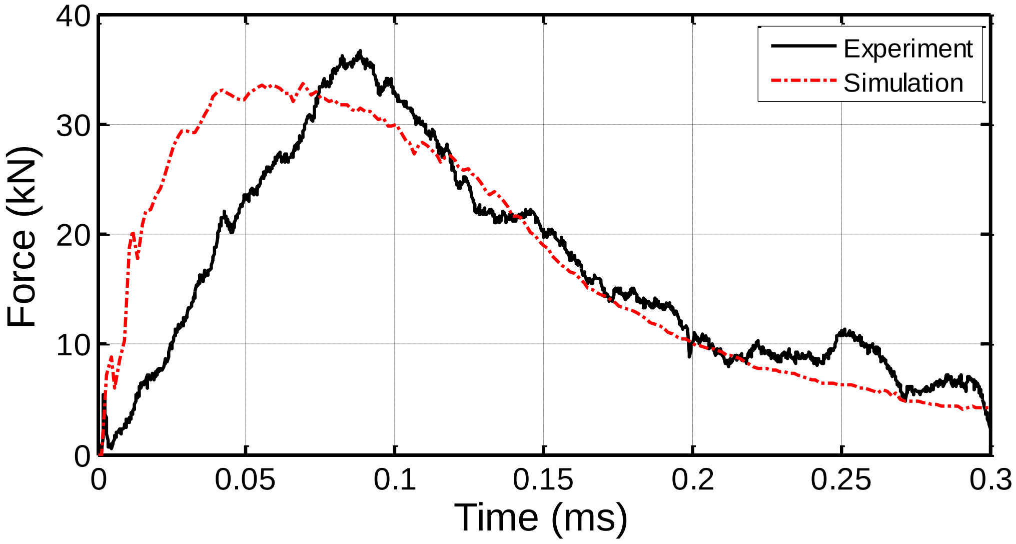

Figure D.32: Simulation results using C2- Lower: 50.8 mm diameter SHI at 107.3 m/s (356 J); Compared to UCSD Test 29: 110.0 m/s (356 J)

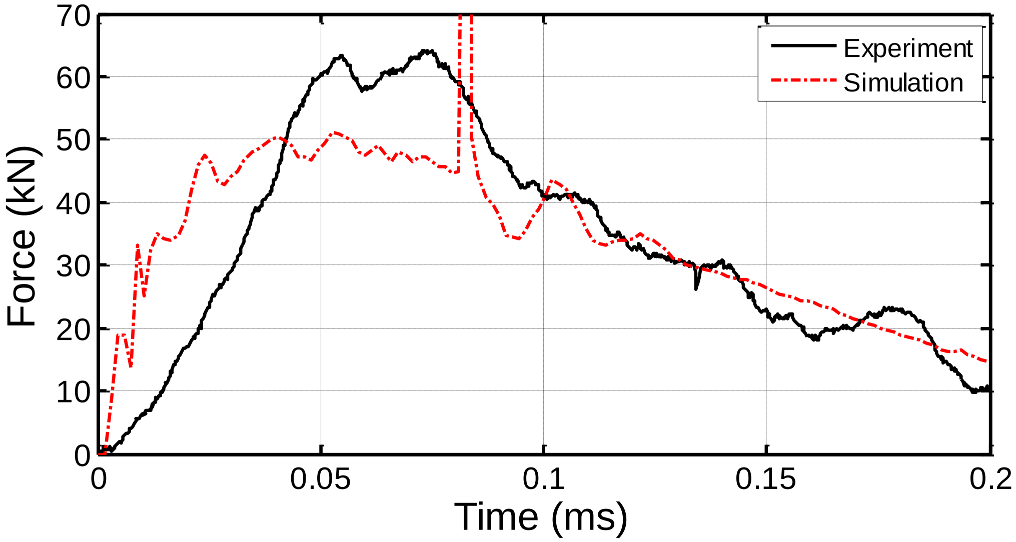

Figure D.33: Simulation results using C2 – Lower: 50.8 diameter SHI at 144.1 m/s (641 J); Compared to UCSD Test 11: 144.3 m/s (641 J)

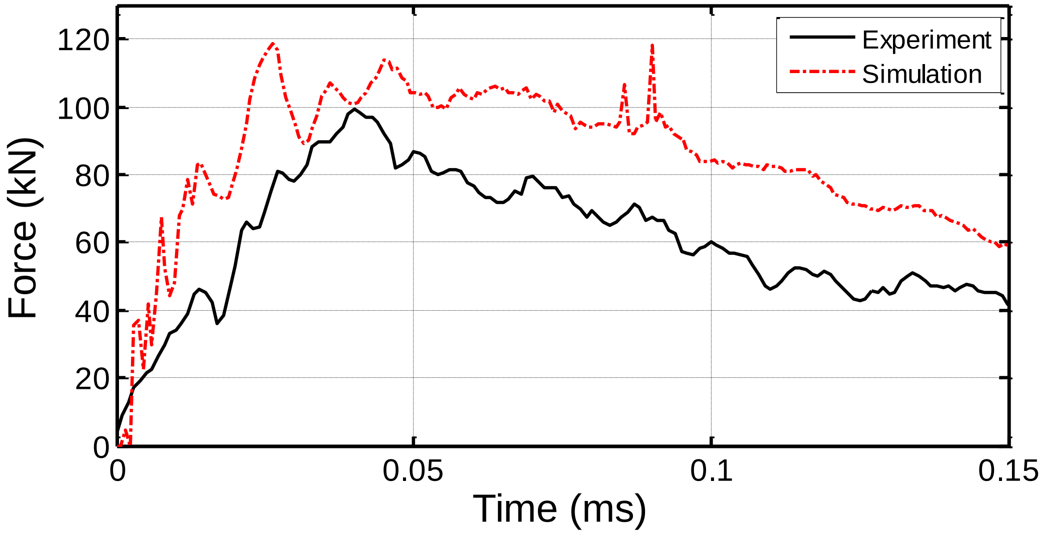

Figure D.34: Simulation results using C2 – Lower: 61.0 mm diameter SHI at 190.0 m/s (1927 J); Compared to Purdue Test 124: 189.2 (1933 J)

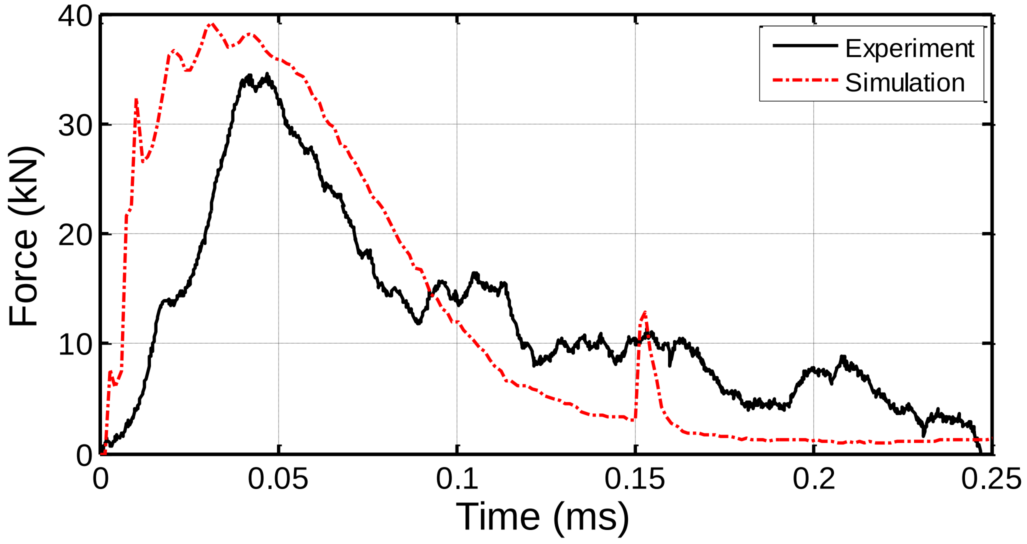

Figure D.35: Simulation results using C3- Upper: 38.1 mm diameter SHI at 144.1 m/s (271 J); Compared to UCSD Test 3:142.0 m/s (248 J)

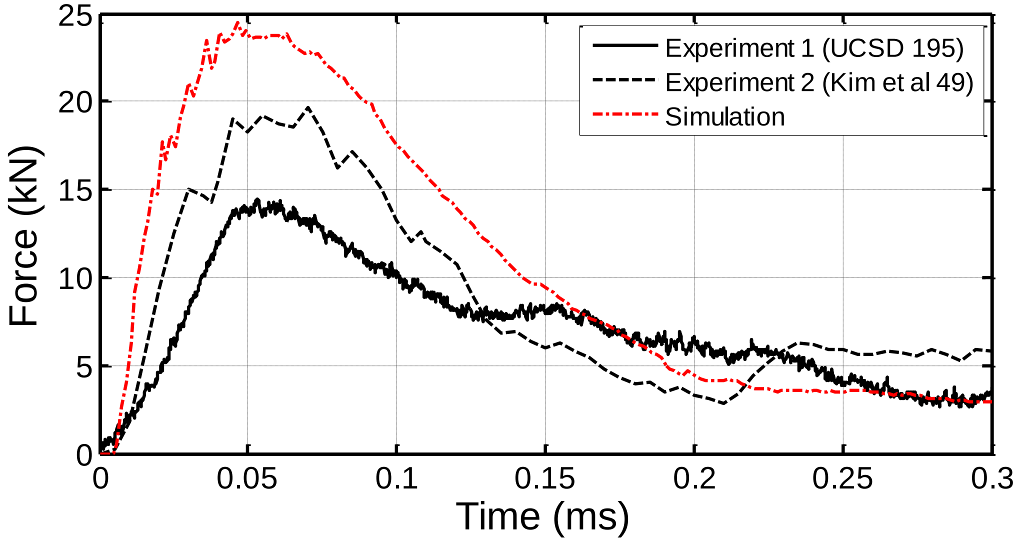

Figure D. 36: Simulation results using C3- Upper: 50.8 mm diameter SHI at 60.6 m/s (114 J); Compared to UCSD Test 195: 60.6 m/s (114 J) and Kim et al. Test 49: 61.9 m/s (108 J)

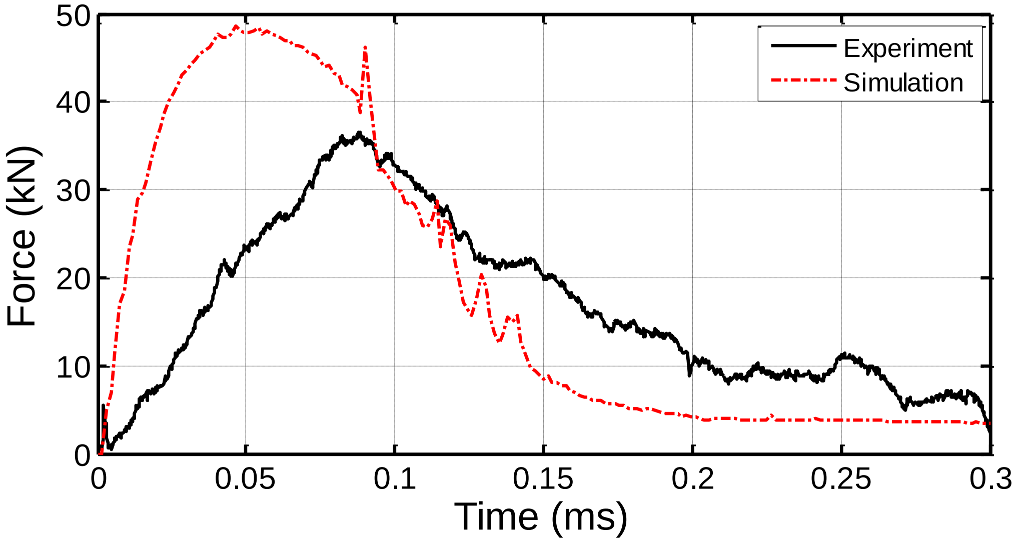

Figure D.37: Simulation results using C3- Upper: 50.8 mm diameter SHI at 107.3 m/s (356 J); Compared to UCSD Test 29: 110.0 m/s (356 J)

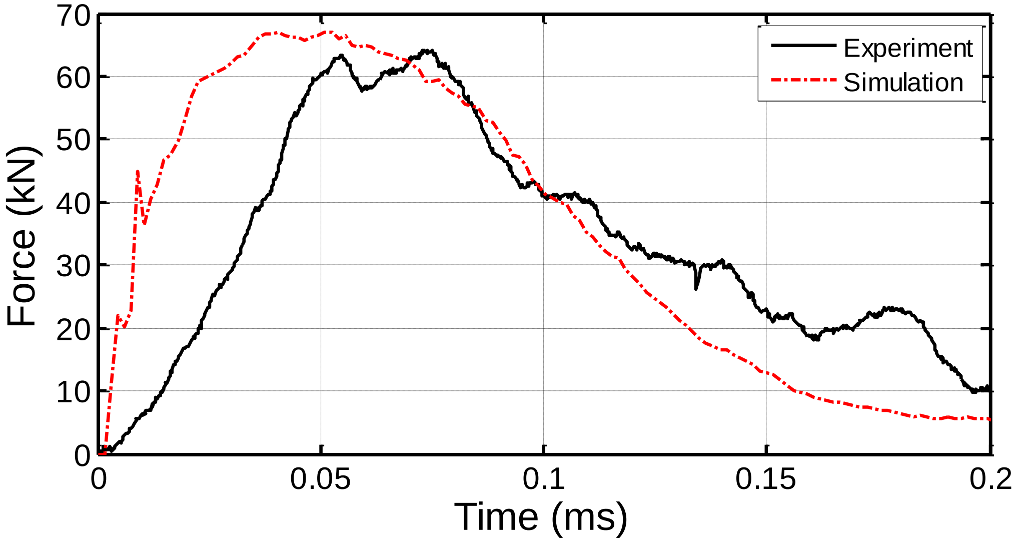

Figure D.38: Simulation results using C3- Upper: 50.8 diameter SHI at 144.1 m/s (641 J); Compared to UCSD Test 11: 144.3 m/s (641 J)

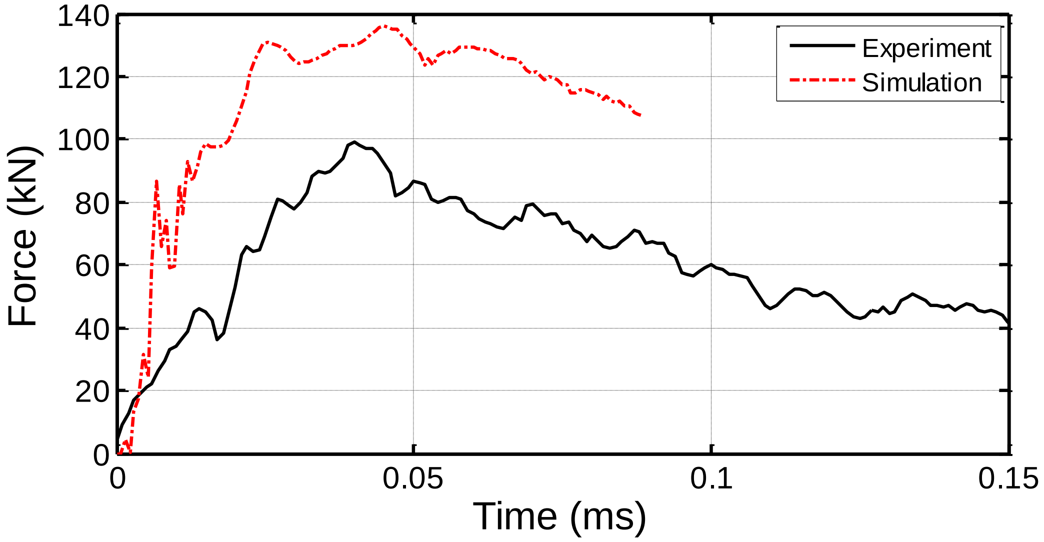

Figure D.39: Simulation results using C3- Upper: 61.0 mm diameter SHI at 190.0 m/s (1927 J); Compared to Purdue Test 124: 189.2 (1933 J)

LIST OF REFERENCES

1. Gates, D. "Bair Pilots Boeing Effort to Replace Best-selling 737." *Seattle Times*, 2008. http://seattletimes.nwsource.com.

2. Kim, H., and K. T. Kedward. "Modeling Hail Ice Impacts and Predicting Impact Damage Initiation in Composite Structures." *AIAA Journal* 38, no. 7 (2000): 1278-288.

3. Kuene, J. N. *Development of a Hail Ice Impact Model and the Dynamic Compressive Strength Properties of Ice*. Thesis, Purdue University, 2004.

4. Park, H. *Resistance of Adhesively Bonded Composite Lap Joints to Damage by Transverse Ice Impact*. Thesis, Purdue University, 2006.

5. Kim, H., and J. N. Kuene. "Compressive Strength of Ice and Impact Strain Rates." *Journal of Material Science* 42 (2007): 2802-806.

6. Kim, H., D. Welch, and K. Kedward. "Experimental Investigation of High Velocity Ice Impacts on Woven Carbon/epoxy Composite Panels." *Composites Part A: Applied Science and Manufacturing* 34, no. 1 (2003): 25-41.

7. Schulson, Erland M. "The Brittle Failure of Ice under Compression." *The Journal of Physical Chemistry B* 101, no. 32 (1997): 6254-258.

8. Schulson, E. "Brittle Failure of Ice." *Engineering Fracture Mechanics* 68, no. 17-18 (2001): 1839-887.

9. Fasanella, E., R. Boitnott, and S. Kellas. "Test and Analysis Correlation of High Speed Impacts of Ice Cylinders." In *Proceedings from 9th International LS-DYNA Users Conference*. 2006.

10. Carney, K., D. Benson, P. Dubois, and R. Lee. "A Phenomenological High Strain Rate Model with Failure for Ice." *International Journal of Solids and Structures* 43, no. 25-26 (2006): 7820-839.

11. Mellor, M., and D. Cole. "Deformation and Failure of Ice under Constant Stress or Constant Strain-rate." *Cold Regions Science and Technology* 5, no. 3 (1982): 201-19.

12. Shen, L., S. Zhao, X. Lu, and Y. Shi. "Effects of Temperature and Strain Rate on Uniaxial Compressive Strength of Naturally Formed Fresh-Water Ice." In *Proceedings of the Seventh International Conference on Offshore Mechanics and Arctic Engineering*, 19-23. ASME, 1988.

13. Kuehn, G. A., E. M. Schulson, D. E. Jones, and J. Zhang. "The Compressive Strength of Ice Cubes of Different Sizes." *Journal of Offshore Mechanics and Arctic Engineering* 115, no. 2 (1993): 142. Jones, Stephen J. "High Strain-Rate Compression Tests on Ice." *The Journal of Physical Chemistry B* 101, no. 32 (1997): 6099-101.

14. Shazly, M., V. Prakash, and B. Lerch. "High Strain-rate Behavior of Ice under Unaxial Compression." *International Journal of Solids and Structures* 46 (2009): 1499-515.

15. Dutta, P. K., D. M. Cole, E. M. Schulson, and D. S. Sodhi. "A Fracture Study of Ice Under High Strain Rate Loading." In *Proceedings of The Thirteenth (2003) International Offshore and Polar Engineering Conference*, 465-72. Honolulu, Hawaii. 2003.

16. Halpin, J. C., and H. Kim. "Managing Impact Risk for Composite Structures: Unifying Durability and Damage Tolerance Perspective." Lecture, FAA/EASA/Industry Composite Damage Tolerance and Maintenance Workshop, Amsterdam, May 2007.

17. Kim, Hyonny. *The Damage Resistance of Composite Structures to High Velocity Ice Impacts and Their Tolerance to Impact Damage*. Diss., University of California, Santa Barbara, 1998.

18. Petrenko, Victor F., and Robert W. Whitworth. *Physics of Ice*. Oxford: Oxford University Press, 1999.

19. Singh, S., K. C. Masiulaniec, K. J. DeWitt, and R. K. Britton. "Measurements of the Impact Forces of Shed Ice Striking a Surface." In *Aerospace Sciences Meeting and Exhibit, 32nd, Reno, NV, Jan 10-13, 1994*. Proceedings. AIAA, 1994.

20. *Abaqus 6.9-2 Analysis User Manual*. SIMULIA, 2009.

21. Anghileri, M., L. Castelletti, F. Invernizzi, and M. Mascheroni. "A Survey of Numerical Models for Hail Impact Analysis Using Explicit Finite Element Codes." *International Journal of Impact Engineering* 31, no. 8 (2005): 929-44.

22. Cheng, Jingyun, and Wieslaw K. Binienda. "Simulation of Soft Projectiles Impacting Composite Targets Using an Arbitrary Lagrangian-Eulerian Formulation." *Journal of Aircraft* 43, no. 6 (2006): 1726-731.

23. Airoldi, A., and B. Cacchione. "Modelling of Impact Forces and Pressures in Lagrangian Bird Strike Analyses." *International Journal of Impact Engineering* 32, no. 10 (2006): 1651-677.